A STUDY OF D SEMILEPTONIC DECAYS TO PSEUDOSCALAR MESONS

A Dissertation

Presented to the Faculty of the Graduate School

of Cornell University

in Partial Fulfillment of the Requirements for the Degree of

Doctor of Philosophy

by

Laura Johanna Fields

May 2009

A STUDY OF *D* SEMILEPTONIC DECAYS TO PSEUDOSCALAR MESONS

Laura Johanna Fields, Ph.D.

Cornell University 2009

Using the entire $\psi(3770) \to D\bar{D}$ event sample collected by the CLEO-c detector, the decays $D^0 \to \pi^- e^+ \nu_e$, $D^0 \to K^- e^+ \nu_e$, $D^+ \to \pi^0 e^+ \nu_e$ and $D^+ \to \bar{K}^0 e^+ \nu_e$ are studied via a tagged analysis technique that reconstructs semileptonic decays opposite fully reconstructed hadronic decays. Partial rates are measured in several q^2 bins, and these are combined with form factor parameterizations to extract branching fractions and form factor parameters. Taking form factor predictions from lattice QCD, the CKM matrix elements $|V_{cd}|$ and $|V_{cs}|$ are also calculated.

BIOGRAPHICAL SKETCH

Laura Johanna Fields was born in Little Rock, Arkansas in 1979. She spent a quiet childhood buried in novels, and when she graduated from Little Rock Central High, she had not traveled further from home than Ohio, a situation which caused her to think of Ohio as exotic. She first became interested in science in college, where she was encouraged to study physics by friendly professors in the University of Arkansas's physics department.

Never one to assume that she has all the right answers, Laura has often wondered whether her decision to pursue physics as a career was the right one. While she may never know for sure, she is grateful for the vast problem-solving toolkit her studies have provided and for the many spectacular doors they have opened for her. These included opportunities to solve interesting problems in places far more exotic than Ohio, such as Alaska, Switzerland, England and Ithaca, New York, where she has spent the last many years thinking about semileptonic decays. Upon completion of her degree, she plans to take a well-deserved vacation and then pursue rumors that, in addition to semileptonic decays, there are a few other interesting interactions going on in the universe.

ACKNOWLEDGEMENTS

Firstly, I would like to thank my adviser, Ritchie Patterson; Hopefully, I've absorbed some of her excellent ability to clarify problems and their solutions. The work reported here was done in collaboration with Bo Xin, whom I thank for helping to our work the best it could possibly be. The advice and frequent encouragement of Bo's adviser, Ian Shipsey, were also always appreciated.

The CLEO detector began collecting data about a month before I was born. As such, I've never met most of the people who deserve thanks here, but am grateful to the hundreds of people who built and maintained CESR and CLEO throughout the past thirty years, as well as the National Science Foundation, who funded this work.

When I arrived to work on CLEO, I knew next to nothing about how to actually *do* particle physics, and will always be indebted to a long list of CLEOn's who helped me figure it out. Most of them sat in desks next to me or down the hall and cheerfully answered all my stupid questions, and then became friends, including Hanna, Lauren, Nadia, Jim, Richard, Peter, Steve and Xin.

Graduate school is not always a very pleasant experience, but I had a lot of friends how made it worthwhile, both those I met here as well as a long list of old friends who are always there when I need them, no matter how far apart we are. In particular, Elaine and Val deserve special mention for keeping me sane all these years. I'm also grateful to my family back in Arkansas who have always supported my dreams, even when they didn't understand why I had them.

And finally, thanks to Lucy, Julius and Oliver, who always make me smile, and to Howard, who shows me everyday how much he adores me and somehow always knows where my keys are.

TABLE OF CONTENTS

LIST OF TABLES

LIST OF FIGURES

CHAPTER 1

INTRODUCTION

The theory known as the Standard Model of Particle Physics postulates a set of particles and describes how these particles interact. By any measure, it is an incredibly successful theory; nearly all experimental evidence available to date indicates that the universe is indeed made of the particles suggested by the Standard Model, and that they behave as the theory predicts. But despite its success, the Standard Model is not likely to be the final model of particle physics. Numerous questions left unanswered, such as how gravity fits into the theory and why it contains many apparently ad-hoc parameters, indicate that the Standard Model is likely incomplete. There are numerous endeavors currently underway by particle physicists around the world in the hope that, either singly or collectively, these efforts will find an inconsistency in the Standard Model that will lead to a more complete understanding of the universe.

This document is a description of one of these endeavors: a study of several semileptonic decays of the D meson using the CLEO-c particle detector. A key element of this study is the Cabibbo-Kobayashi-Maskawa (CKM) matrix [1] that governs quark-mixing in the Standard model. While the values of the CKM matrix elements are not predicted, the model does place constraints on them. Specifically, it predicts that the CKM matrix is unitary; confirmation of this key Standard Model prediction, through precision measurements of the CKM elements, is a primary goal of modern particle physics.

The formalism of D semileptonic decays within the standard model is discussed in detail in the following chapter. For the moment, we note that the differential decay rate for semileptonic decay of a D meson to a pseudoscalar meson P can be approximated by:

$$\frac{d\Gamma(D \to Pe\nu)}{dq^2} = X\frac{G_F^2 \left|V_{cq}\right|^2}{24\pi^3}p^3 \left|f_+\left(q^2\right)\right|^2, \qquad (1.1)$$

where q^2 is the invariant mass of the lepton-neutrino system, G_F is the Fermi constant, $\left|V_{cq}\right|$ is the CKM matrix element $|V_{cd}|$ for pion final states and $|V_{cs}|$ for kaon final states, $f_+\left(q^2\right)$ is the form factor that encompasses the strong-interaction dynamics of the decay and X is a multiplicative factor due to isospin.

The principle results of the study described here are measurements of $\frac{d\Gamma}{dq^2}$ integrated over seven q^2 bins each for $D^0 \to \pi^- e^+ \nu_e$ and $D^+ \to \pi^0 e^+ \nu_e$ and nine q^2 bins each for $D^0 \to K^- e^+ \nu_e$ and $D^+ \to \bar{K}^0 e^+ \nu_e$ *. These results are combined with parameterizations of $f_+\left(q^2\right)$ to make a number of secondary measurements, including branching fractions, form factor shape parameters and $\left|V_{cq}\right||f_+(0)|$. The latter can be used to extract $|V_{cd}|$ and $|V_{cs}|$, but large uncertainties in the theoretical predictions of $|f_+(0)|$ limit all measurements of the CKM elements via semileptonic decays, including ours. Although recent advances in Lattice Quantum Chromodynamics (LQCD) offer hope of form factor predictions with significantly smaller uncertainties, these new techniques require further testing before their results can be used with confidence. Because $|V_{cd}|$ and $|V_{cs}|$ have been measured in other experimental environments, and because they are very tightly constrained if CKM unitarity is assumed, D semileptonic decays can be used to obtain very precise measurements of form factor parameters. This, combined with their similarity to the B decays, where measurements of $|V_{ub}|$ are particularly crucial to studies of CKM unitarity, makes D semileptonic decays an ideal testing ground for LQCD. It is thus measurements of form factor parameters that are the most important contribution of our work.

The remainder of this document is organized as follows: in Section 2, we provide an overview of semileptonic decays and their experimental and theoretical status. Section 3 gives an overview the particle accelerators and detectors used to make our measurements. The data analysis procedure is then discussed in detail, beginning with event reconstruction techniques in Section 4 and continuing with partial rate measurements

---

*Charge conjugate modes are implied throughout this document

and their systematic uncertainties in Sections 5 and 6. The fits to the partial rates and determination of the form factor parameters, branching fractions and CKM matrix elements, are discussed in Section 7. Finally, a number of tests of the analysis are provided in Section 8, as well as a conclusion in Section 9.

CHAPTER 2

SEMILEPTONIC DECAYS

Within the Standard Model, the amplitude for semileptonic decay of a D meson (composed of quarks c and $\bar{q}'$) to a meson P (composed of quarks q and $\bar{q}'$) is given by [2]:

$$\mathcal{M}(D \to Pl\nu) = -i\frac{G_F}{\sqrt{2}}V_{cq}L^\mu H_\mu, \tag{2.1}$$

where L^μ and H_μ are the leptonic and hadronic currents describing the weak and strong dynamics of the interaction, respectively. The leptonic current is:

$$L^\mu = \bar{u}_l\gamma^{mu}\left(1 - \gamma_5\right)v_\nu, \tag{2.2}$$

where u_l, v_ν are the Dirac lepton and neutrino spinors. The hadronic current can be written as:

$$H_\mu = \langle P|\bar{q}\gamma_\mu\left(1 - \gamma_5\right)c|D\rangle. \tag{2.3}$$

In the decays of interest here, where the final state mesons are pseudoscalars, this simplifies to:

$$H_\mu = \langle P|\bar{q}\gamma_\mu c|D\rangle. \tag{2.4}$$

Because D semileptonic decays occur in the non-perturbative regime of QCD, this matrix element cannot be solved analytically. However, it can be parameterized by expanding the current in terms of all possible independent 4-vectors that can describe the decay, with each of these multiplied by a Lorentz-invariant form factor. In our case, there are only two independent 4-vectors, which can be taken to be $p_D + p_P$ and $p_D - p_P$, where p_D and p_P are the momenta of the initial and final state mesons respectively. Moreover, there is only one Lorentz invariant quantity, which is traditionally taken to be the invariant mass of the virtual W boson, $q^2 = (p_D - p_P)^2$. Thus, we can write the hadronic current as:

$$H_\mu = f_+\left(q^2\right)(p_D + p_P)^\mu + f_-\left(q^2\right)(P_D - P_P)^\mu, \tag{2.5}$$

4

where $f_+\left(q^2\right)$ and $f_-\left(q^2\right)$ are the Lorentz-invariant form factors.

The decays considered here are semi-electronic decays; in this case, taking the limit as $m_l \to 0$ is an excellent approximation, and the current is further simplified to

$$H_\mu = f_+\left(q^2\right)(p_D + p_P)^\mu . \tag{2.6}$$

Using these expressions for the hadronic and leptonic currents, Equation 2.4 can be reduced to approximation given in Chapter 1:

$$\frac{d\Gamma(D \to Pe\nu)}{dq^2} = X \frac{G_F^2 \left|V_{cq}\right|^2}{24\pi^3} p^3 \left|f_+\left(q^2\right)\right|^2 , \tag{2.7}$$

where where p is the momentum of the daughter meson in the D rest frame and X, the multiplicative factor due to isospin, is unity for all D decays to pseudoscalars except $D^+ \to \pi^0 e^+ \nu_e$, where it is $\frac{1}{2}$. Experimental studies, including the one described here, measure $d\Gamma/dq^2$ integrated over several q^2 bins in each semileptonic mode. In order to compare these with theoretical predictions, which provide estimates of $f_+(q^2)$ at one or several points in q^2, it is convenient to fit the results using parameterizations of $f_+(q^2)$. Several such parameterizations are discussed in the next section.

2.1   Form Factor Parameterizations

A number of parameterizations of $f_+\left(q^2\right)$ have been suggested. The most theoretically motivated is known as the 'series' parameterization [3] and follows from a dispersion relation:

$$f_+\left(q^2\right) = f_+(0) \frac{1 - \alpha}{1 - \frac{q^2}{M_{D^*}^2}} + \frac{1}{\pi} \int_{(m_D+m_P)^2}^{\infty} dt \frac{\mathrm{Im} f_+(t)}{t - q^2 - i\epsilon}, \tag{2.8}$$

where m_D and m_P are the masses of the semileptonic parent and daughter mesons, respectively, and α gives the relative contribution of this meson to $f_+(0)$. Simple expansions of the above integral in q^2 may not converge. However, a transformation of

variables from q^2 to z, where

$$z(q^2, t_0) = \frac{\sqrt{t_+ - q^2} - \sqrt{t_+ - t_0}}{\sqrt{t_+ - q^2} + \sqrt{t_+ - t_0}}, \qquad (2.9)$$

optimizes convergence. Here, $t_{\pm} = (m_D \pm -m_P)^2$ and t_0 is any real number less than t_+; The form factor, expanded in $z(q^2, t_0)$, is given by:

$$f_+(q^2) = \frac{1}{P(q^2)\phi(q^2, t_0)} \sum_{k=0}^{\infty} a_k(t_0) \left[z\left(q^2, t_0\right) \right]^k, \qquad (2.10)$$

where a_k are real coefficients, $P(q^2) = z(q^2, M_{D^*}^2)$ for $D \to Ke\nu$ and $P(q^2) = 1$ for $D \to \pi e\nu$, and $\phi(q^2, t_0)$ is any function that is analytic outside a cut in the complex q^2 plane that lies along the real axis from t_+ to ∞. It is customary to take $t_0 = t_+\left(1 - \sqrt{1 - t_-/t_+}\right)$, which minimizes the maximum value of $z(q^2, t_0)$, and to choose:

$$\begin{aligned} \phi(t, t_0) \quad = \quad & \alpha(\sqrt{t_+ - t} + \sqrt{t_+ - t_0}) \frac{t_+ - t}{(t_+ - t_0)^{1/4}} \times \\ & \frac{\left(\sqrt{t_+ - t} + \sqrt{t_+ - t_-}\right)^{3/2}}{\left(\sqrt{t_+ - t} + \sqrt{t_+}\right)^5}. \end{aligned} \qquad (2.11)$$

Fits to experimental data or theoretical prediction using this model are usually made using the first two or three terms in the expansion given by equation 2.10, with either $f_+(0)$ and $r_1 = a_1/a_0$ or $f_+(0)$, r_1 and $r_2 = a_2/a_0$ varied. That this model makes no ad hoc assumptions gives it a distinct advantages over the alternative models described below. However, measurements have only recently become precise enough to inspire fits to this model rather than simpler formulations.

Another parameterization, known as the 'simple pole' model, assumes that the dispersion relation given in Equation 2.8 is dominated by a single pole:

$$f_+(q^2) = \frac{f_+(0)}{1 - \frac{q^2}{m_{pole}}}. \qquad (2.12)$$

While this model can provide reasonable fits when both M_{pole} and $f_+(0)$ are allowed to float, experimental measurements of M_{pole} are far removed from the expected value of $M_{D^*_{(s)}}$, indicating the higher-order poles are not negligible [4].

A popular parameterization, the 'modified pole' model of Becirevic and Kaidalov (BK), was designed to deal with this shortcoming of the simple pole model, to which it adds an effective pole:

$$f_+(q^2) = \frac{f_+(0)}{(1 - \frac{q^2}{m_{pole}})(1 - \alpha\frac{q^2}{m_{pole}})}.$$

(2.13)

This model assumes that β, a parameter that quantifies scaling violations, is near unity while δ, which describes gluon hard-scattering, is near zero. These assumptions lead to the prediction that:

$$1 + 1/\beta - \delta \equiv \frac{M_D^2 - m_p^2}{f_+(0)}\frac{df_+(q^2)}{dq^2}\bigg|_{q^2=0} \approx 2.$$

(2.14)

There are experimental indications that this approximation is not valid [4]; this is one reason why the series expansion has become the preferred parameterization. However, the modified pole model has been the most widely used parameterization in recent experimental and theoretical studies, and it does provide good-quality fits to data and theory when $f_+(0)$ and α are varied.

An older model, the ISGW2 parametrization [5], is based on a quark model and hypothesizes:

$$f_+\left(q^2\right) = f_+\left(q_{\max}^2\right)\left(1 + \frac{r_{\mathrm{ISGW2}}^2}{12}\left(q_{\max}^2 - q^2\right)\right)^{-2},$$

(2.15)

and predicts $r_{\mathrm{ISGW2}} = 1.12\ \mathrm{GeV}^{-1}$. Experimental measurements do not support this prediction, which has caused the parameterization to fall out of favor. It is still occasionally used, in which cases $f_+(0)$ and r_{ISGW2} are varied.

2.2   Theoretical Predictions

A number of theoretical techniques exist to estimate the form factors, but all are associated with significant uncertainties. Recent developments in Lattice QCD offer the possibility of calculations with uncertainties on the order of a few percent, although

such results are not yet available. The Light Cone Sum Rule approach (LCSR) provides estimates that are competitive with current LQCD results, but are not systematically improvable. Quark models have also been used, but these results are associated with large and unquantified uncertainties. We now review each of these techniques and their form factor predictions, emphasizing those that have made predictions of the form factors at $q^2 = 0$, which we denote $f_+^\pi(0)$ for pion final states and $f_+^K(0)$ for kaon final states, and the modified pole model shape parameter, similarly denoted α^π and α^K. We choose the modified pole model because no theoretical results are available using the series parameterization and because results using the modified pole model are widely available.

2.2.1 Lattice QCD

Lattice QCD takes advantage of the path integral formulation of quantum field theory, in which matrix elements are computed by calculating the weighted average of functionals over all possible 'paths' of configuration space. Making use of the overview of LQCD provided in [6], the expectation value for some operator $\Gamma[\pi]$, in a system involving a field $\phi(x)$ and continuum action S, is given by:

$$\langle\langle \Gamma[\phi]\rangle\rangle = \frac{\int D\phi(x)\,\Gamma[x]e^{-S[\phi]}}{\int D\phi(t)e^{-S[x]}}, \tag{2.16}$$

which is a weighted average over all paths with weight $e^{-S[x]}$. In this context, the term 'path' refers to each possible set of values the field $\phi(x)$ may take over an infinite number of paths. Calculation of such objects can be considerably simplified by discretizing each space and time dimension into a finite sized grid of points, or "lattice". A particular path, or 'configuration,' is specified by the value of the field ϕ at each point on the grid. This reduces an infinite problem to a problem of numerical integration:

$$\langle\langle \Gamma[\phi(x)]\rangle\rangle = \frac{e^{-S[\phi]}\Gamma[\phi]\prod_{xj\in grid} d\phi(x_j)}{\int e^{-S[\phi]}\prod_{xj\in grid} d\phi(x_j)} \tag{2.17}$$

where S is now the original action with any spatial or temporal derivatives replaced by differences in the field at neighboring lattice sites. In simple cases, these integrals can be evaluated numerically; more complicated situations require a procedure known as Monte Carlo integration, which involves the generation of a large number of configurations $\phi(x_j)$ such that the probability for obtaining a particular configuration is proportional to $e^{-S[\phi(x_j)]}$. Thus, an unweighted average of Γ over all of these paths is equivalent to a weighted average over the uniformly distributed paths. Estimates of matrix elements then can be calculated using these configurations, but the results are just that – estimates, and are associated with a statistical uncertainty [6]. Semileptonic decay form factors are obtained in LQCD by calculating two and three point functions on the lattice. In asymptotic limits, these functions are proportional to the matrix element given in Equation 2.4 [7].

LQCD form factor predictions are associated with many systematic uncertainties, many of which are related to the discretization approximation. Moreover, because a calculation with lattice spacing a is only able to resolve particles with momentum greater than $2a$, current LQCD simulations are limited to low q^2 regions ($q^2 \lesssim 2$). Another drawback of LQCD is that computational cost rises as quark mass decreases, necessitating use of unphysical u and d quark masses and extrapolation of results to the true quark masses.

Until very recently, only "quenched" LQCD calculations of form factors were available. That is, it was not possible to include fermion vacuum polarization in the QCD actions. Calculations are now available [8] using "Symanzik improved staggered quark" actions, which provide both accurate simulation of light quarks and relatively efficient calculations. These calculations estimate:

$$f_+^\pi(0) = 0.64 \pm 0.03 \pm 0.06$$
$$f_+^K(0) = 0.73 \pm 0.03 \pm 0.07.$$

Although not affected by the large quenching uncertainties of previous measurements, these estimates do carry combined systematic uncertainties of 10%, which is dominated by those associated with discretization of the charm quark. These uncertainties are expected to be significantly improved in future studies. The results were also fit using the modified pole model, with the shape parameters found to be:

$$\alpha^\pi = 0.44 \pm 0.04$$

$$\alpha^K = 0.50 \pm 0.04.$$

where the uncertainties are statistical only. Unfortunately, systematic uncertainties on the shape parameters are not available.

Although unquenched LQCD has the potential to provide results with much improved uncertainties, the results quoted above are still on par with quenched results. For instance, the work reported in [7] finds:

$$f_+^\pi(0) = 0.57 \pm 0.06 \pm 0.02$$

$$f_+^K(0) = 0.66 \pm 0.04 \pm 0.01,$$

In addition to the sources of systematic uncertainty described above for the unquenched calculation, these systematic uncertainties also include those due to the quenching approximation. Due in part to the use of smaller lattice spacings, this study is able to achieve smaller systematic uncertainties than the unquenched study. However, because they are dominated by quenching uncertainties, they are not systematically improvable.

2.2.2   Light Cone Sum Rules

Several attempts have been made to calculate D semileptonic form factor parameters using Light Cone Sum Rules. This technique builds on more basic QCD sum rules that exploit the fact that QCD is perturbative over short distances. In certain kinematic

regions, the quarks involved in the interaction can be treated as free; dispersion relations can then be used to extend the solution to other kinematic regions [9].

Light cone sum rules begin by investigating correlation functions such as the following, which is relevant to $D^0 \to \pi e \nu$ [10]:

$$F_\mu(p_\pi, q) = i \int d^4 x e^{iq \cdot x} \langle \pi(p_\pi) | T \bar{u}(x) \gamma_\mu c(x), m_c \bar{c}(0) i \gamma_5 d(0) | 0 \rangle. \tag{2.18}$$

For the case of small fixed q^2 and a highly virtual c quark, the region that dominates this integral is that near the light cone $x^2 = 0$ [11]. In this case, the above correlation function can be evaluated by contracting the c-quark fields and expanding the remaining matrix elements in an operator product expansion about the light cone. The expansion is ordered by a quantity called 'twist,' equal the difference between an operator's dimension and spin. For example, the lowest order twist contribution to the correlation function given in Equation 2.18 is [9]:

$$F_\mu(p_\pi, q) = m_c f_\pi \int_0^1 \frac{du \phi_p i(u, \mu_c)}{m_c^2 - (1-u)p_\pi^2 - u(p_p i + q)^2}, \tag{2.19}$$

where $\phi^\pi(u, \mu_c)$ is a "light-cone distribution amplitude" – a non-perturbative object that describes the long distance behavior of the pion; it is considered an input of the theory and is taken from experiment or LQCD. The pion decay constant is given by f_π and μ_c, which can be approximated by $\sqrt{m_c^2 - P_d^2}$, is the scale that separates the long-distance effects of the light cone amplitudes from the short-distance effects of their coefficients.

The light cone expansion can be linked to the semileptonic form factors by considering a dispersion relation, which is obtained from the original correlation function (Eq. 2.18) by inserting between the two currents the identity in the form of a complete set of states with D-meson quantum numbers:

$$F_\mu(P_D, q) = \frac{\langle \pi | \bar{u} \gamma_\mu c | D \rangle \langle D | \bar{c} i \gamma_5 d | 0 \rangle}{m_D^2 - p_D^2} + \sum_x \frac{\langle \pi | \bar{u} \gamma_\mu c | x \rangle \langle x | \bar{c} i \gamma_5 d | 0 \rangle}{m_x^2 - p_D^2}. \tag{2.20}$$

11

Relating the dispersion relation to light cone expansion, one arrives at an approximate expression of the form factor f_+, known as the 'sum rule' [10]:

$$f_+^\pi\left(q^2\right) = \frac{1}{2m_D^2 f_D}e^{m_c^2/m^2}\left[F_0^{(2)} + \frac{\alpha_s\left(\mu_c\right)}{3\pi}F_1^{(2)} + F_0^{(3,4)}\right], \tag{2.21}$$

which is valid only for low q^2. The twist contribution correlation functions F_x^y are functions of q^2, a mass scale M, m_c, s_D^0 and $\mu_c = \sqrt{(m_D^2 - m_c^2)}$. In addition to uncertainties due to uncalculated terms in the expansion, LCSR form factor results carry uncertainties from each of these inputs.

A study using this technique [10] has found:

$$f_+^\pi(0) = 0.65 \pm 0.11 \tag{2.22}$$

Calculations of $f_+^K(0)$ are found to vary too strongly with the somewhat poorly known strange quark mass to make strong predictions of their value. Although the standard LCSR breaks down at $q^2 \approx 0.6$ GeV^2, where the higher order terms in the light cone expansion begin to grow, a different sum rule can be constructed at the upper limits of q^2. This is done by assuming that the lowest lying D^* pole dominates the form factor at high q^2. Using this new sum rule to calculate the form factor at high q^2 and fitting these together with the low-q^2 results using the modified pole parameterization, the shape parameters are found to be:

$$\alpha^\pi = 0.01^{+0.11}_{0.07},$$
$$\alpha^K = -0.07^{+0.15}_{0.07}.$$

It is unclear how much the assumption of single-pole dominance at high q^2 may influence these shape predictions.

Preliminary results from a continuation of this study [12], making use of improved twist calculations and updated input parameters, are also available. Although this study does not address form factor shape parameters, it did quantify uncertainties due to the

strange quark mass, enabling a prediction of $f_+^K(0)$ and finding:

$$f_+^\pi(0) = 0.63 \pm 0.11,$$

$$f_+^K(0) = 0.75 \pm 0.12.$$

Attempts have also been made to combine LCSR's and heavy quark effective theory [13], resulting in form factor normalization estimates with large uncertainties:

$$f_+^\pi(0) = 0.67 \pm 0.20,$$

$$f_+^K(0) = 0.67 \pm 0.19.$$

The LCSR approach to form factor calculations is not perfect. It is accurate only at low q^2 and possibly at high q^2; even in these regions, its accuracy is limited by uncertainty in input parameters and contributions due to higher order terms in the expansions. Although the uncertainties can be gauged fairly accurately and can be reduced by better experimental and LQCD estimates of input parameters, LCSR is not exact and its accuracy cannot be systematically improved.

2.2.3 Quark Models

Quark models (QM) approximate the real QCD matrix elements:

$$\langle P|\bar{q}\gamma_\mu c|D\rangle. \tag{2.23}$$

by matrix elements composed of naive models of the QCD currents:

$$\langle \mathbf{P}|\bar{\mathbf{q}}\gamma^\mu \mathbf{c}|\mathbf{D}\rangle \tag{2.24}$$

where the bold-faced symbols denote fields that are not derived from QCD but are rather based on some naive model tuned to simulate experimental results. These models assume that mesons can be accurately modeled as $q\bar{q}$ bound states and that the wave functions of the mesons are steeply peaked and nearly confined within the radius of the

hadron [14]. A number of models have been formulated, some of which are capable of calculating form factors over most of the q^2 range. However, their approximate nature means that they cannot be systematically improved, and estimating the uncertainty on their calculations is difficult.

One of the oldest quark models is known as the ISGW model [15]. Proposed in 1985 to address CP violation in B semileptonic decays, it has since been used to model a number of other semileptonic decays. The model calculates matrix elements using non-relativistic vectors that are superpositions of $q\bar{q}$ states with momentum-weighted wave functions, chosen to be solutions of the Schroedinger Equation with a Coulomb plus linear potential. Since it is a non-relativistic approximation, the predictions of the model must be extrapolated to relativistic regimes. The model was updated (to become the "ISGW2" model) in 1995 [5], taking into account heavy quark symmetry. The ISGW2 model predicts the form factors at $q^2 = 0$ to be:

$$f_+^\pi(0) = 0.60,$$
$$f_+^K(0) = 0.85.$$

It is difficult to estimate the errors on these numbers, but they are thought to be large (> 25%). As mentioned in the previous section, the ISGW2 model also predicts the form factor shape given in equation 2.15. However, the models inability to accurately estimate relativistic corrections casts doubt on its form factor shape predictions.

A more modern model, known as the Relativistic Dispersion quark model [14], was developed to deal with the many problems suffered by previous quark models. Among these were a strong dependence on input parameters and an inability to incorporate relativistic effects. This model requires form factors to be relativistic double spectral representations obtained from the wave functions of the initial and final state mesons. The model has several input parameter that are calibrated using experimental and LQCD results. Fitting the resulting form factors using the modified pole parameterization, the

model finds:

$$f_+^\pi(0) = 0.69,$$

$$f_+^K(0) = 0.78,$$

$$\alpha^\pi = 0.20,$$

$$\alpha^K = 0.24.$$

As with other quark models, the uncertainties on these calculations are difficult to gauge, but based on comparison with other calculations and experiment, they are though to be of order 10%.

2.3   Experimental Measurements

We now turn our attention from theoretical form factor predictions to experimental measurements. Again, we emphasize results of $f_+^\pi(0)$, $f_+^K(0)$, α^π and α^K. We also discuss branching fraction measurements, and, where applicable, form factor shape parameters estimated using the series parameterization (r_1^π, r_2^π, r_1^K and r_2^K).

2.3.1   Mark III

The MARK III experiment pioneered the tagging technique used by many CLEO-c analyses, including the one described here. Located at the SPEAR e^+e^- storage ring at the Stanford Linear Accelerator Center, it was among the first to make measurements involving D semileptonic decays [16]. Collecting data using electron-positron collisions at the $\psi(3770)$ and using essentially the same analysis technique that CLEO-c now uses, the analysis found 3636 tag candidates, 7 $D^0 \rightarrow \pi^- e^+ \nu_e$ and 56 $D^0 \rightarrow K^- e^+ \nu_e$ candi-

dates, leading branching fraction measurements of

$$\mathcal{B}\left(D^0 \to \pi^- e^+ \nu_e\right) = \left(0.39^{+0.23}_{0.11} \pm 0.04\right)\%, \tag{2.25}$$

$$\mathcal{B}\left(D^0 \to K^- e^+ \nu_e\right) = (3.4 \pm 0.5 \pm 0.05)\%. \tag{2.26}$$

2.3.2 FOCUS

The FOCUS experiment was a fixed target experiment that studied photon on beryllium collisions at Fermilab. It was used to collect a sample of approximately 13,000 semileptonic decay candidates, which were used to measure the modified pole shape parameter in $D^0 \to K^- \mu^+ \nu$ [17]:

$$\alpha^K = 0.28 \pm 0.08 \pm 0.07. \tag{2.27}$$

2.3.3 BES

The BES-II experiment, located along the Beijing Electron Positron Collider (BEPC II), has also used a tagged analysis technique to measure D semileptonic branching fractions [18]. They have collected 7584 tags, 104 $D^0 \to K^- e^+ \nu_e$ candidates and 9 $D^0 \to \pi^- e^+ \nu_e$ candidates, measuring

$$\mathcal{B}\left(D^0 \to \pi^- e^+ \nu_e\right) = (0.33 \pm 0.13 \pm 0.03)\%,$$

$$\mathcal{B}\left(D^0 \to K^- e^+ \nu_e\right) = (3.82 \pm 0.40 \pm 0.27)\%.$$

2.3.4 Belle

Based at the KEKb storage ring, the Belle experiment has collected 281 fb^{-1} of data taken at the $\Upsilon(4S)$ resonance. The Belle collaboration has used this data to measure both branching fractions and form factors in D semileptonic decays [19]. Studying

$e^+e^- \rightarrow DD^*X$ and $e^+e^- \rightarrow D^*D^*X$ events, they find:

$$\mathcal{B}\left(D^0 \rightarrow \pi l \nu\right) = (0.255 \pm 0.019 \pm 0.016)\,\%,$$

$$\mathcal{B}\left(D^0 \rightarrow K l \nu\right) = (3.45 \pm 0.07 \pm 0.20)\,\%.$$

where the lepton can be either an electron or a muon. They have also measured the differential decay rate $d\Gamma/dq^2$ in 10 bins for $D^0 \rightarrow \pi l \nu$ and 28 bins for $D^0 \rightarrow K l \nu$ and fit these distributions to the modified pole model, finding:

$$f_+^\pi(0) = 0.624 \pm 0.020 \pm 0.030$$

$$f_+^K(0) = 0.695 \pm 0.007 \pm 0.022$$

$$\alpha^\pi = 0.10 \pm 0.21 \pm 0.10,$$

$$\alpha^K = 0.52 \pm 0.08 \pm 0.06.$$

2.3.5 BaBar

The BaBar Collaboration have studied the decay $D^0 \rightarrow K^- e^+ \nu_e$ in detail [20]. Located at the PEP-II storage ring at the Stanford Linear Accelerator Center, BaBar collected $75\mathrm{fb}^-1$ of data, of which $c\bar{c}$ continuum event candidates were used for the D semileptonic analysis. Measuring the branching fraction with respect to $\bar{D}^0 \rightarrow K^+ \pi^-$, they find:

$$\mathcal{B}\left(D^0 \rightarrow K^- e^+ \nu_e\right) = (3.522 \pm 0.027 \pm 0.045 \pm 0.065)\,\%, \tag{2.28}$$

where the final uncertainty is from the $\bar{D}^0 \rightarrow K^+ \pi^-$ branching fraction. They have also measured form factor parameters using ten q^2 bins, finding

$$f_+^K(0) = 0.727 \pm 0.007 \pm 0.005 \pm 0.007, \tag{2.29}$$

where the final uncertainty is due to the $\bar{D}^0 \rightarrow K^+ \pi^-$ branching fraction, the D lifetime and V_{cs}. The modified shape parameter is found to be:

$$\alpha^K = 0.43 \pm 0.03 \pm 0.04. \tag{2.30}$$

The BaBar collaboration has also fit form factor distributions using the series expansion with three terms in the expansion, finding:

$$r_1^K = -2.5 \pm 0.2 \pm 0.2,$$

$$r_2^K = 0.6 \pm 6. \pm 5.$$

2.3.6 CLEO

The CLEO experiment has made several studies of D semileptonic decays, including a CLEO III analysis of 7 fb^{-1} of data taken at or below the $\Upsilon(4S)$ resonance [4]. Using $D^{*+} \to D^0 \pi^+$ candidates and fully reconstructing all final state particles except the neutrino, this analysis measured form factor shape parameters

$$\alpha^\pi = 0.37^{+0.20}_{-0.31} \pm 0.15,$$

$$\alpha^K = 0.36 \pm 0.10^{+0.03}_{-0.07},$$

where the reconstructed lepton was either an electron or a muon.

The most recent CLEO studies of D semileptonic decays were a pair of analyses that used the initial 281 pb^{-1} of CLEO-c data and employed complimentary analysis technique. One analysis [4] followed a tagged procedure very similar to the one described here, while the other [21] used an untagged technique that fully reconstructs all particles in the event without requirements on the identity of the D decay opposite the semileptonic candidate. The results of the analyses have been averaged [4] (taking into account the considerable correlations on the uncertainties) and the branching fraction are found to be:

$$\mathcal{B}\left(D^0 \to \pi^- e^+ \nu_e\right) = (0.304 \pm 0.011 \pm 0.005)\,\%,$$

$$\mathcal{B}\left(D^0 \to K^- e^+ \nu_e\right) = (3.60 \pm 0.03 \pm 0.06)\,\%,$$

$$\mathcal{B}\left(D^+ \to \pi^0 e^+ \nu_e\right) = (0.378 \pm 0.020 \pm 0.012)\,\%,$$

$$\mathcal{B}\left(D^+ \to \bar{K}^0 e^+ \nu_e\right) = (8.69 \pm 0.12 \pm 0.19)\,\%,$$

18

The only averaged form factor results are those using the three parameter series model:

$$f_+^\pi(0) = 0.634 \pm 0.022 \pm 0.009 \pm 0.003$$

$$f_+^K(0) = 0.764 \pm 0.007 \pm 0.005 \pm 0.001$$

where the final errors are due to V_{cq}, which we have taken from the latest fits to electroweak data assuming CKM unitarity [22], which find $|V_{cd}| = 0.2256 \pm .0010$ and $|V_{cs}| = .97334 \pm 0.00023$. The form factor shape parameters, again using a three parameter series model, are:

$$r_1^\pi = -1.7 \pm 0.5 \pm 0.1,$$

$$r_2^\pi = -1.8 \pm 3.2 \pm 0.9,$$

$$r_1^K = -2.4 \pm 0.3 \pm 0.1,$$

$$r_2^K = 21 \pm 8 \pm 2.$$

The form factor results using a modified pole model have not been averaged. Combining the results from D^0 and D^+ modes, the tagged analysis finds:

$$\alpha^\pi = 0.16 \pm 0.10 \pm 0.05$$

$$\alpha^K = 0.21 \pm 0.05 \pm 0.02.$$

The untagged analysis did not average the D^0 and D^+ modes, so we take their results to be those of the better-measured D^0 modes:

$$\alpha^\pi = 0.37 \pm 0.08 \pm 0.03$$

$$\alpha^K = 0.21 \pm 0.05 \pm 0.03$$

2.3.7 $|V_{cd}|$ and $|V_{cs}|$

The CKM matrix elements $|V_{cd}|$ and $|V_{cs}|$ can be measured using semileptonic decays. For instance, the averaged CLEO-c 281 pb^{-1} analyses find [4]:

$$|V_{cd}| = 0.223 \pm 0.008 \pm 0.003 \pm 0.023 \qquad (2.31)$$

$$|V_{cs}| = 1.019 \pm 0.010 \pm 0.007 \pm 0.106, \qquad (2.32)$$

where the final uncertainty is due to LQCD predictions [8], which find $f_+(0) = 0.64 \pm 0.03 \pm 0.06$ for $D \to \pi$ transitions and $f_=(0) = 0.73 \pm 0.03 \pm 0.07$ for $D \to K$ transition. More precise measurements of $|V_{cd}|$ are available from neutrino/anti-neutrino scattering, where the ratio of double to single muon production is proportional to $|V_{cd}|^2$ [22]. An average of these measurements finds:

$$|V_{cd}| = 0.230 \pm 0.011. \qquad (2.33)$$

Measurements of $|V_{cs}|$ are best made via leptonic or semileptonic decays. An average of all available results gives [22]

$$|V_{cs}| = 1.04 \pm 0.06. \qquad (2.34)$$

The uncertainties on $|V_{cs}|$ and $|V_{cd}|$ are decreased substantially by assuming CKM matrix unitarity. Global fits to all relevant electroweak measurements assuming the CKM unitarity finds [22]:

$$|V_{cd}| = 0.2256 \pm 0.0010 \qquad (2.35)$$

$$|V_{cs}| = 0.9733 \pm 0.0002. \qquad (2.36)$$
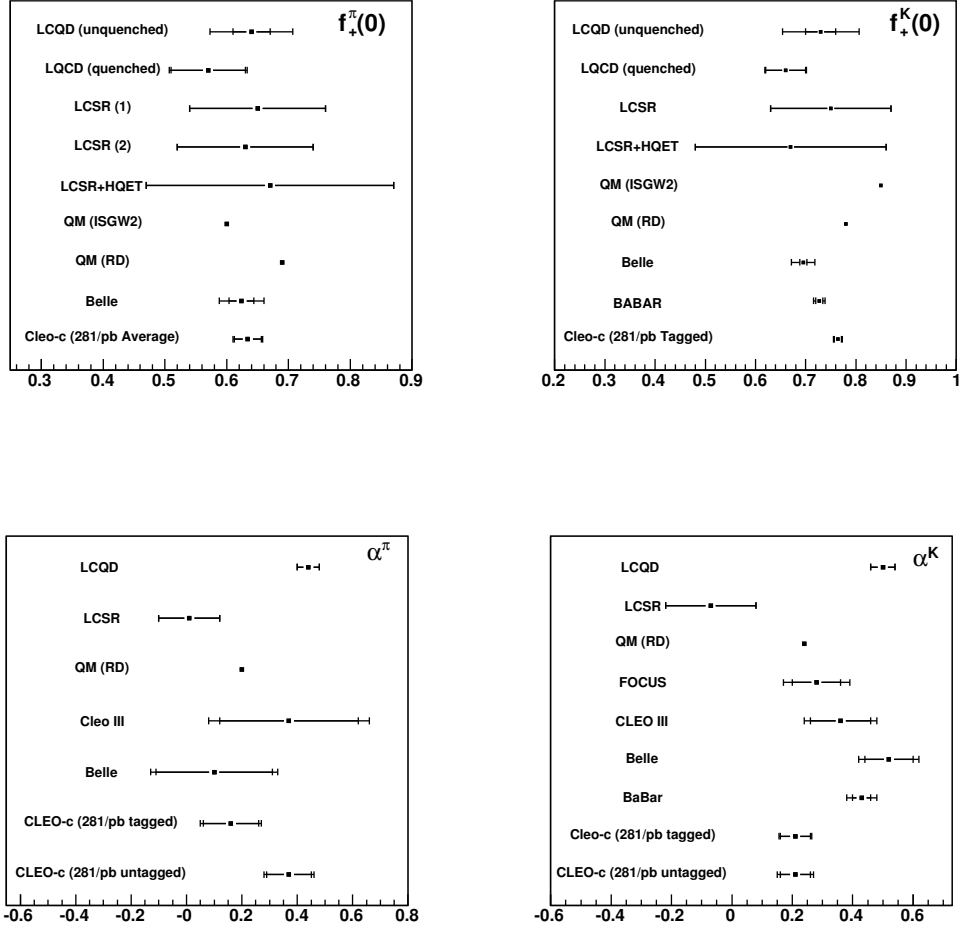
Figure 2.1: Comparison of theoretical predictions and experimental measurements of D semileptonic form factor parameters.
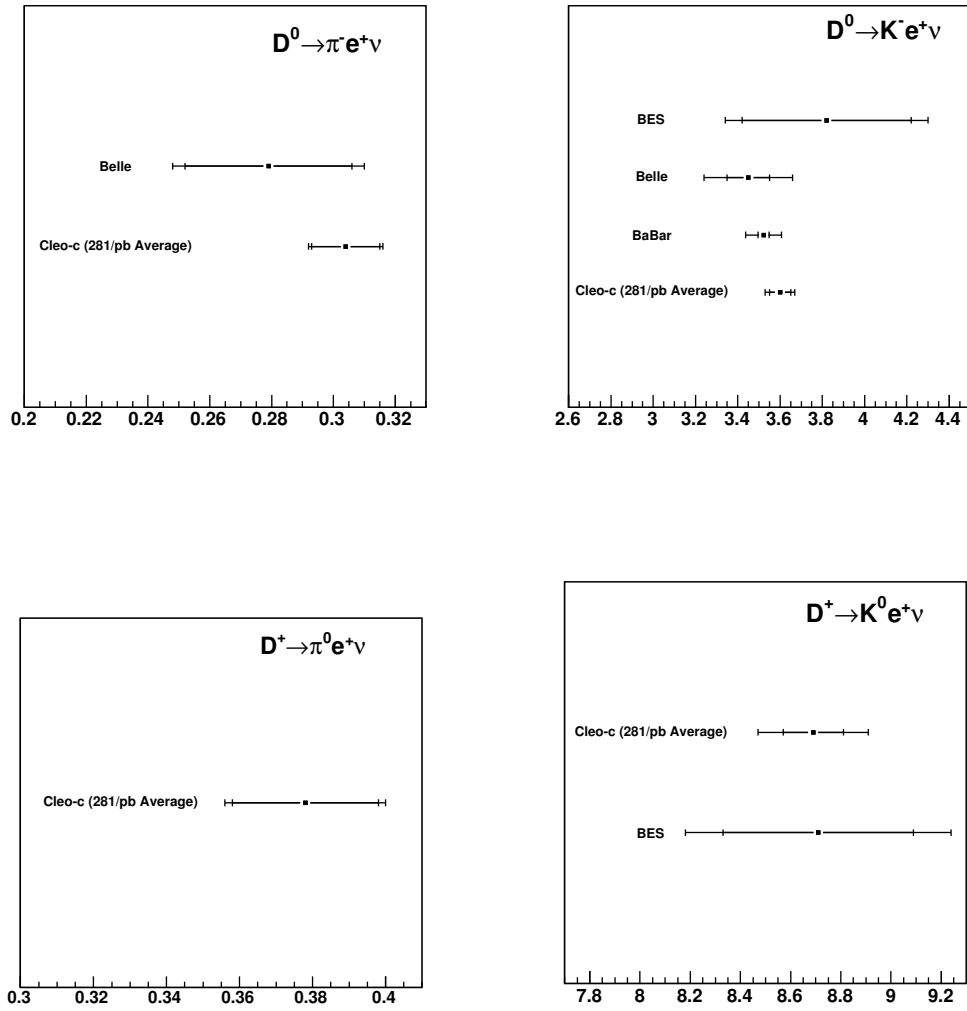
Figure 2.2: Comparison of measurements of *D* semileptonic branching fractions.
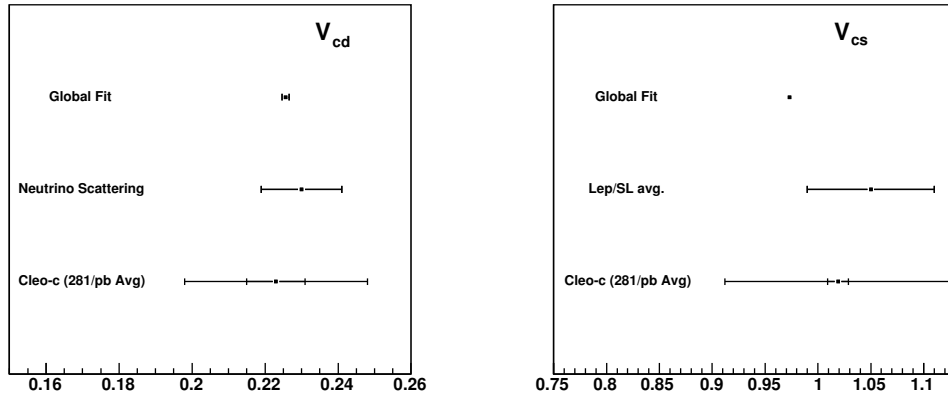
Figure 2.3: Comparison of measurements of CKM matrix elements.

2.4 Summary of Experimental and Theoretical Status

Figures 2.1-2.3 show each of the theoretical and experimental results discussed in the previous sections. The next several chapters detail a new study of D semileptonic decays, which will add a data point to each of the plots shown in Figures 2.1-2.2.

CHAPTER 3

EXPERIMENTAL APPARATUS

3.1   The Cornell Electron Storage Ring

The Cornell Electron Storage Ring (CESR) is located in Ithaca, NY and has been in operation since 1979. It is a 768 meter diameter ring that simultaneously stores beams of electrons and positrons (moving in opposite directions), providing collisions of these beams inside the CLEO detector. While originally designed to create collisions with between 9 and 16 GeV center-of-mass (COM) energies, CESR was augmented in 2002 to produce collisions with around 4 GeV COM energies, near the charm production threshold.

The electrons that are eventually stored in CESR originate from an electron gun with energies of 120 keV. They then enter a 30 meter linear accelerator, which increases their energy to 300 MeV. A synchrotron accelerates the electrons to their final storage energies via kicker magnets before they are injected into CESR. Positrons are injected separately and are obtained by inserting a tungsten target into the path of the electrons in the linear accelerator.

Because acceleration is provided by Radio Frequency (RF) cavities, the particles must be stored in 'bunches'. Within CESR, the beam is composed of a series of "trains" located 14 ns (or 4.2 m) apart, and each train is compose of a series of "bunches" located 40 ps (or 4.2 cm) apart. In typical operating conditions, there are 8 trains, each containing 3-5 bunches. The number of electrons per bunch varies with the operating conditions of the accelerators, and corresponds to a current of around 3 mA or less when $\psi(3770)$ data was taken.

While beam collisions are desired at the interaction point (IP) centered within the CLEO detector, there are a number of parasitic interaction points spaced around the
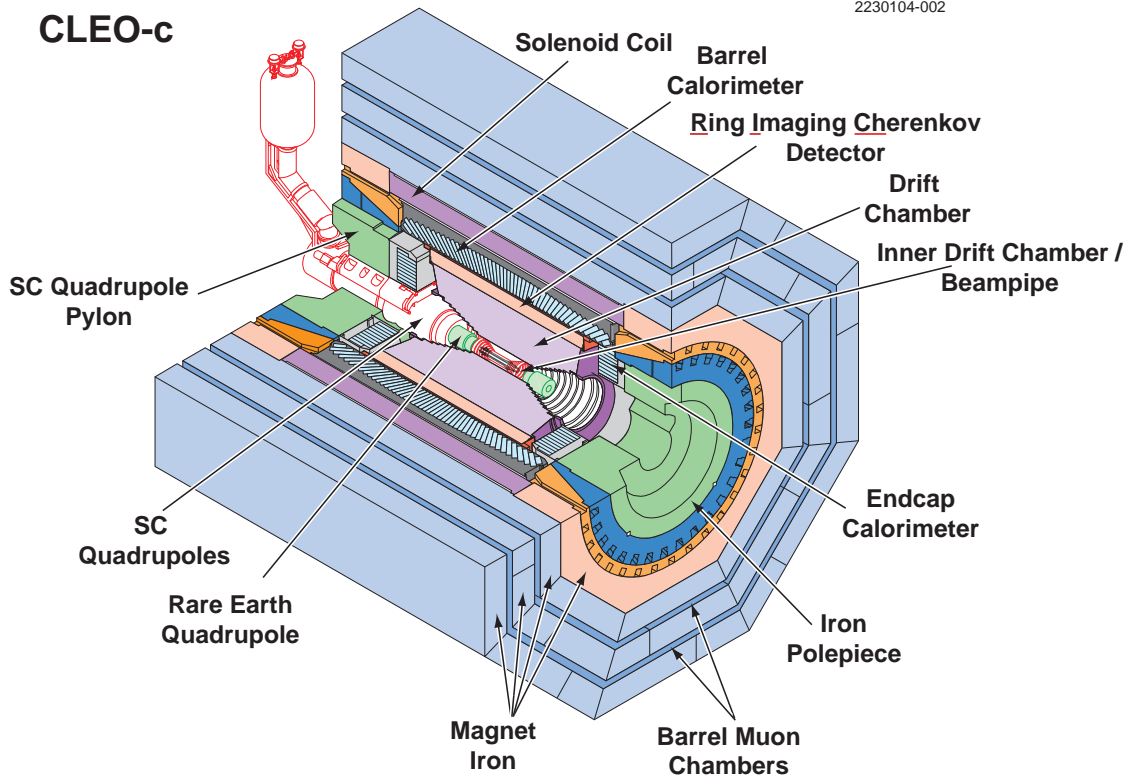
Figure 3.1: The CLEO-c detector

ring. To avoid beam interactions here, electrostatic separators are used, resulting in a 'pretzel orbit' with the electron and positron beams winding around one another. At the main IP, the collision region is composed of a ribbon-like volume approximately 0.18mm x 0.34mm x 1.8 cm. To avoid further interactions near the IP, the colliding beams have a small crossing angle of approximately 3 mrad, causing CESR collisions to have a small but non-zero net momentum.

3.2 The CLEO Detector

When an electron positron collision occurs within CESR, daughter particles of this collision travel through a system of particle detectors collectively known as the CLEO

detector. The original incarnation of CLEO began taking data in 1979, but the CLEO-c detector (shown in figure 3.1) has very few components in common with that original detector. The primary component that remained a part of CLEO throughout its lifespan, the muon system, is generally unused in analyses of charm-threshold data, as muons in collisions at this energy are often not energetic enough to penetrate the chambers. The primary physical components of the detector used in this study of D semileptonic decays are the tracking chambers (DR and ZD), the ring imaging Cerenkov detector (RICH) and the crystal calorimeters (CC). We briefly describe each of these components, as well as the trigger and data acquisition system.

It is useful to refer to certain coordinate systems when discussing the detector sub-components. CLEO commonly uses Cartesian coordinate system with origin at the center of the detector, the z axis lying parallel to the CESR beam line pointing west, the x axis pointing horizontally away from the center of CESR and the y axis pointing up. We also use the polar angle θ, the angle with respect to the positive z axis.

3.2.1   Drift Chambers

The detectors closest to the CESR beamline are drift chambers; their primary purpose is to measure the charge and momentum of charged particles. CLEO has two drift chambers; the primary chamber, known as the DR, surrounds a smaller inner chamber known as the ZD [23]. They are approximately cylindrical (the axis of the cylinder lying along the z axis) and nearly hermetic, covering an angular range of $|\cos\theta| < 0.93$.

The DR(ZD) is composed of approximately 10,000(300) "sense" wires, each surrounded by several parallel "field" wires. The sense wires are arranged into 47(6) DR(ZD) layers, with a ϕ spacing of approximately 1.4 cm. Both chambers are filled with a Helium-Propane mixture that is ionized when the traversed by charged particles. The field wires are held at a positive voltage with respect to the sense wires, causing

27

electron products of the ionization to be pulled towards the sense wires. When they are very near the sense wires, the electrons gain sufficient energy to cause further ionization, creating an "avalanche" of electrons that amplifies the signal.

The timing of the electron avalanche, combined with the known drift velocity and CESR timing information, can be used to approximate the original position of a particle near a wire, with an average resolution of 110 μm. Each of the wires is approximately parallel to the z axis, providing accurate measurements of particle positions in the xy plane. In order to establish the z position of tracks along the axis parallel to the beamline, some of the wires have a small angle with respect to the z axis. These wires are known as "stereo" wires while those without an angular offset are known as "axial" wires. All of the wires in the ZD are stereo, with large angles of 12-15° providing good z measurements near the interaction point. The first 16 layers of the DR are axial wires, with the outer 31 layers having stereo angles of 1.2-1.5°. Further information about the z position of particles is provided by cathode strips, which lie along the outer walls of the DR.

The amount of current deposited by the electron avalanche also provides useful information. Because the current of the electron avalanche is proportional to the number of electrons originally ionized, the change in current deposition as a particle traverses the chambers gives a measurement of the rate of energy loss dE/dx by the particle. The Bethe-Bloch equations [22], along with the measured momentum of the particle, are used to infer the mass of the particle, and thus, to some extent, the identity of the particle. For our purposes, dE/dx is most useful for determining whether a track is a pion, kaon or electron.

The entire tracking chamber lies within a 1.0 Tesla superconducting magnet. This causes the charged particles to curve in the xy plane, with a radius of curvature propor-

tional to their transverse momentum. The tracking chambers provide measurements of charged particle momentum with resolution near 0.6% at 800 MeV/c.

3.2.2 Ring Imaging Cerenkov Detector

The Ring Imaging Cerenkov Detector (RICH) became part of the CLEO detector during an upgrade in 1999. Designed to improve upon the charged particle identification performance already available from dE/dx information in the drift chambers, the RICH begins immediately after the outer edge of the drift chamber with 1 cm layer of lithium fluoride crystals. Particles with velocity exceeding that of a 150 nm photon traveling in LiF will radiate Cerenkov light. The original particle and the Cerenkov light then travels through a 16 cm thick layer of inert nitrogen gas, where the cone of Cerenkov photons (typically composed of around ten photons) expands to a measurable size. The photons are detected in multi-wire proportional chambers filled with a mixture of triethylamine vapor and methane gas. The gas is ionized and the resulting electrons are amplified and readout using cathode pads and low-noise electronics. For each track in an event, a Cerenkov angle is calculated for each photon associated with the track, and likelihoods for kaon, pion, electron, muon and proton hypotheses are calculated.

3.2.3 Crystal Calorimeter

The CLEO crystal calorimeter [24] was installed during an upgrade of the detector that took place in the late 1980's. It is composed of approximately 7800 thalium-doped Cesium Iodide crystals that are 5cm square by 30 cm long. The orientation of a crystal depends on its location within the detector: those within the "barrel" region of the detector ($|\cos\theta| < 0.82$) are arrayed so that their axes are directed towards points very near but not exactly at the IP. Crystals in the two "endcaps" ($0.85 < |\cos\theta| < 0.95$) are

arrayed parallel to the z axis. These orientations were designed to reduce the likelihood of a particle interacting in space between the crystals.

Although the calorimeter spans 95% of the solid angle, CLEO data analyses generally consider only showers contained in the 'good barrel' ($|\cos\theta| < 0.82$) and 'good endcap' regions ($0.85\,|\cos\theta| < 0.82$), which exclude the barrel/endcap transition region and the outer portions of the calorimeter, where detector material degrades performance. In the good barrel and endcap regions, the calorimeter provides an energy resolution of $\sigma E/E \sim 5\%$ at 100 MeV.

Four silicon photodiodes mounted on each of the 7800 crystals transform the light produced in the scintillating crystals into an electrical signal; this is then fed into a preamplifier and mixer/shaper cards which combine and shape the four preamp signals before sending them on to analog-to-digital converters.

Both charged and neutral particles leave energy in the calorimeter, often in more than one crystal. Photon and lepton showers are generally more compact than those associated with hadrons. Neutral and charged particles can be distinguished by associating showers with tracks, or lack thereof, in the drift chambers. The ratio of shower energy to track momentum (E/p), as well as shower shape variables such as $E9/E25$ (the ratio of energies in the innermost 9/25 crystals of a shower) are also powerful tools in determining the identity of particles. The fine segmentation of the calorimeter also allows for excellent identification of $\pi^0 \to \gamma\gamma$ decays, which have a typical mass resolution of 6 MeV.

Several of the crystals in the calorimeter are prone to such high noise levels that they are not useful in physics analysis. These are termed "hot" crystals. The noise levels for all crystals are monitored during data-taking and a list of the hot crystals for each run is used to exclude these crystals during event reconstruction.

3.2.4 Trigger

Although a collision can occur during any one of CESR's bunch crossings, which occur at a rate of several MHz during normal operating conditions, it is not practical to read out all of CLEO's detector channels at this rate. Useful collisions occur at rates of order 100 Hz, which is a feasible readout rate. The CLEO-c trigger [25] was designed to determine when the detector channels should be readout. Since this decision must be made very quickly, only the outer drift chamber and calorimeter are used to make this decision.

In the absence of the trigger, all of the CLEO detectors continuously collect information, which is overwritten on timescales of one μs. Every 48 ns, a preliminary decision is made by the trigger based on low level information from the detectors. If this information is consistent with a collision useful for calibration or analysis, gates are closed and data taking stops for approximately two μs while the trigger makes a second decision, after which either the data acquisition system writes the detector data to disk or the electronics gates are opened and the detector continues collecting information until another trigger occurs.

The trigger analyzes tracking information by comparing charge depositions in the drift chamber with all possible hit combinations consistent with tracks. Each of the wires in the 16 axial layers are considered individually, while wires in the outer stereo layers are grouped into four-by-four blocks that are treated as single objects. Information in the calorimeter is similarly parsed into groups of overlapping eight-by-eight blocks of crystals. The final trigger decision is based on the number of tracks observed above some momentum threshold and the number of showers observed above some energy threshold. There are different selection criteria, any one of which will trigger readout. The one of most interest to semileptonic decays is the "two-track" trigger, which requires at least

two tracks in the axial section of the drift chamber with momentum greater than 167 MeV/c.

3.3 Data and Monte Carlo Samples

We use the entire CLEO-c data sample taken at the $\psi(3770)$ resonance, which has an integrated luminosity of 818 pb^{-1}. Monte Carlo (MC) simulations are used to evaluate efficiencies and backgrounds. These samples are GEANT-based [26] and use EvtGen [27]; final state radiation (FSR) is simulated using PHOTOS [28] version 2.15 with FSR interference enabled. A sample $\psi(3770) \rightarrow D\bar{D}$ MC corresponding to 20 times the data luminosity was generated with both D mesons decaying generically according to the latest available D branching fractions and decay models. This sample, along with a sample of simulated $e^+e^- \rightarrow q\bar{q}$ (where $q = u,d$ or s), $e^+e^- \rightarrow \tau^+\tau^-$ and $e^+e^- \rightarrow \psi(2S)\gamma$ events corresponding to five times the data luminosity, is referred to as "generic MC". We also use a sample of $\psi(3770) \rightarrow D\bar{D}$ events in which the D meson decays to one of the four studied semileptonic modes and the $\bar{D}$ decays to one of the hadronic final states used in tag reconstruction. This sample corresponds to approximately 100 times the data luminosity and is referred to as "Signal MC". In both the generic and signal MC samples, the semileptonic decays are generated using the modified pole parameterization with parameters fixed to those measured in the initial 281 pb^{-1} of CLEO-c data.

CHAPTER 4

EVENT RECONSTRUCTION

CLEO-c data is ideally suited for precision measurements of D-decays. A large sample of the data was collected using electron-positron collisions with center-of-mass energies near the $\psi(3770)$ resonance. At these energies, D mesons are produced solely as part of $ee \rightarrow D\bar{D}$ events. This enables the use of a data analysis technique pioneered by the Mark-III collaboration [16] known as "tagging". Fully reconstructed $\bar{D}$ decays in hadronic modes provide a clean sample of D decays opposite the hadronic "tags," where studies of Semileptonic decays can be conducted.

To begin our study of D semileptonic decays, we must first identify events in the CLEO-c $\psi(3770)$ data which contain pairs of tag and semileptonic candidates. These are themselves composed of candidate pions, kaons, electrons and photons. Below, we first describe the particle identification criteria and then the requirements that combinations of these particles must satisfy to become tag or semileptonic candidates.

4.1 Tracks

Candidate electrons, charged kaons and charged pions are all selected from tracks in the drift chamber. In each case, the track must satisfy the following basic track quality criteria:

- $0.05 \leq p \leq 2.0$ GeV

- $|db| \leq 0.005$ m

- $|z0| \leq 0.05$ m

- $\chi^2 \leq 100000$

- hit fraction ≥ 0.5

- $|\cos\theta| \leq 0.93$,

where p is the measured momentum of the track, $|db|$ and $|z0|$ are the distances from the track's production vertex to the beam interaction point in the xy plane and along the z axis respectively, χ^2 refers to the quality of the track fit, hit fraction is the fraction of layers in the drift chamber that registered the track and $\cos\theta$ is the angle between the track and the z axis. Charged track reconstruction efficiencies are approximately 84% for kaons and 89% for pions and electrons; lost tracks within $|\cos\theta| < 0.93$ are almost exclusively due to particle decay in flight and material interaction in the drift chambers.

4.2 Electrons

Electron candidates are selected from good-quality tracks with $p > 200$ MeV, $\cos\theta < 0.9$, $0.5 \leq E/p < 1.5$ and $-3.0 \leq \sigma_e^{de/dx} < 3.5$, where E is the calorimeter energy associated with the track and $\sigma_e^{de/dx}$ measures the deviation of the track's energy deposition in the drift chamber from that expected for an electron. For each track fulfilling all these criteria, a combined likelihood $\mathcal{F}$ is constructed based on E/p, dE/dx and RICH information such that $0 \leq \mathcal{F} \leq 1$, where are tracks with $\mathcal{F} = 0$ are least likely to be electrons and tracks with $\mathcal{F} = 1$ are most likely to be electrons. We require that $\mathcal{F} > 0.8$. The efficiency for electron identification is about 50% at the low momentum threshhold of 200 MeV/c, rises sharply to 92% at 300 MeV/c, and varies mildly as a function of momentum beyond 300 MeV/c. Roughly 0.1% of charged hadrons satisfy the electron identification criteria.

4.3 Photons

Final state radiation can cause mismeasurements of any of the charged particles in our events. Because of their low mass compared to the other particles of interest here, elec-

trons are most likely to undergo FSR. To reduce the effect of FSR on our measurements, we attempt to recover photons, which we term "bremsstrahlung photons," in the neighborhood of the electrons by identifying calorimeter showers that:

- are not from hot crystals,

- have energy greater than 30 MeV,

- are not matched to tracks

and have momentum within 5 degrees of the electron track.

4.4 Charged Hadrons

Charged pions are identified from good quality tracks whose dE/dx information is consistent with a pion hypothesis within three standard deviations σ. A likelihood ($\mathcal{L}$) designed to separate charged pions from charged kaons is formed from RICH and dE/dX information such that tracks with $\mathcal{L} > 0$ are more likely to be pions than kaons and tracks with $\mathcal{L} < 0$ are more likely to be kaons than pions. We require pion candidates satisfy $\mathcal{L} \geq 0$. Charged kaons are identified in a similar manner; kaon candidates are required to be good tracks with dE/dx information consistent within 3σ of a kaon hypothesis and have $\mathcal{L} \leq 0$. Given a properly reconstructed track, hadron identification efficiencies are approximately 95%, with midisdentifaction rates of a few percent.

4.5 Neutral Hadrons

Neutral pions are reconstructed by combining pairs good-quality showers (as defined above for bremsstrahlung showers) that have shower shape parameters consistent with photons. The π^0's are required to satisfy a three sigma mass cut, and when multiple π^0's are found opposite the tag, we choose the π^0 candidate with invariant mass closest to the

nominal π^0 mass. Efficiencies for π^0 reconstruction vary from 40% at a momentum of 100 MeV/c to 60% at 900 MeV/c.

Neutral kaons are reconstructed via $K_S \rightarrow \pi^+\pi^-$ by combining pairs of oppositely charged vertex constrained tracks that are within 3 σ of the nominal K_S mass. This procedure results in a K_S^0 mass resolution of 2-2.5 MeV/c^2 and a K_S^0 reconstruction efficiency of around 94%. When multiple K_S candidates are found opposite the tag, we choose the candidate with invariant mass closest to the nominal K_S mass.

4.6 Tag Decays

Tag decays are reconstructed from combinations of charged and neutral hadrons in three D^0 tag modes ($\bar{D}^0 \rightarrow K^+\pi^-$, $\bar{D}^0 \rightarrow K^+\pi^-\pi^0$ and $\bar{D}^0 \rightarrow K^+\pi^-\pi^-\pi^+$) and six $D^\pm$ tag modes ($D^- \rightarrow K^+\pi^-\pi^-$, $D^- \rightarrow K^+\pi^-\pi^-\pi^0$, $D^- \rightarrow K^0\pi^-$, $D^- \rightarrow K^0\pi^-\pi^0$, $D^- \rightarrow K^0\pi^-\pi^-\pi^+$ and $D^- \rightarrow K^+K^-\pi^-$). Tag candidates must satisfy the $M_{BC} = \sqrt{E_{beam}^2 - \mathbf{P}_{tag}^2}$ and $\Delta E = E_{beam} - E_{tag}$ cuts shown in Table 4.1. In events with multiple candidates, we choose the

Table 4.1: ΔE= $E_{beam} - E_{tag}$ requirements for Tag reconstruction

mode	ΔE cut	
$D^0 \rightarrow K^-\pi^+$	$-0.030 < \Delta E < 0.030$	$1.858 < M_{BC} < 1.874$
$D^0 \rightarrow K^-\pi^+\pi^0$	$-0.050 < \Delta E < 0.044$	$1.858 < M_{BC} < 1.874$
$D^0 \rightarrow K^-\pi^+\pi^+\pi^-$	$-0.020 < \Delta E < 0.020$	$1.858 < M_{BC} < 1.874$
$D^+ \rightarrow K^-\pi^+\pi^+$	$-0.0232 < \Delta E < 0.0232$	$1.8628 < M_{BC} < 1.8788$
$D^+ \rightarrow K^-\pi^+\pi^+\pi^0$	$-0.0276 < \Delta E < 0.0276$	$1.8628 < M_{BC} < 1.8788$
$D^+ \rightarrow K_S^0\pi^+$	$-0.0272 < \Delta E < 0.0272$	$1.8628 < M_{BC} < 1.8788$
$D^+ \rightarrow K_S^0\pi^+\pi^0$	$-0.0366 < \Delta E < 0.0366$	$1.8628 < M_{BC} < 1.8788$
$D^+ \rightarrow K^0\pi^+\pi^+\pi^-$	$0.0159 < \Delta E < 0.0159$	$1.8628 < M_{BC} < 1.8788$
$D^+ \rightarrow K^+K^-\pi^+$	$-0.0138 < \Delta E < 0.0138$	$1.8628 < M_{BC} < 1.8788$

candidate per tag mode per flavor that has the smallest value of ΔE.

4.7   Semileptonic Decays

For each tag satisfying the criteria above, we search for electron/meson pairs opposite the tag that are consistent with a $D^0 \to \pi^- e^+ \nu_e$, $D^0 \to K^- e^+ \nu_e$, $D^+ \to \pi^0 e^+ \nu_e$ or $D^+ \to \bar{K}^0 e^+ \nu_e$. For $D^0 \to \pi^- e^+ \nu_e$ and $D^0 \to K^- e^+ \nu_e$, the electron and meson are required to have opposite charge. For $D^+ \to \pi^0 e^+ \nu_e$ and $D^+ \to \bar{K}^0 e^+ \nu_e$, the electron and tag are required to have opposite charge.

CHAPTER 5

PARTIAL RATES

Our most fundamental measurements are the differential semileptonic rates integrated over seven q^2 bins for $D^0 \to \pi^- e^+ \nu_e$ and $D^+ \to \pi^0 e^+ \nu_e$ and nine q^2 bins for $D^0 \to K^- e^+ \nu_e$ and $D^+ \to \bar{K}^0 e^+ \nu_e$. We denote these by $\Delta\Gamma_i = \int_i \frac{d\Gamma}{dq^2} dq^2$. To measure the partial rates, we first determine the number of observed tags ("tag yields"), $N_{\text{tag}}^{\text{obs},\alpha}$, in each tag mode α. This is related to the number of tags that actually occurred, N_{tag}^α, via:

$$N^\alpha = \frac{N_{\text{tag}}^{\text{obs},\alpha}}{\epsilon_{\text{tag}}^\alpha}, \tag{5.1}$$

where ϵ_{tag}^α is the reconstruction efficiency for tag mode α. We then determine the number of events with both a tag and semileptonic candidate. These "signal yields", $n_j^{\text{obs},\alpha}$, are determined separately for each tag mode α and q^2 bin j. The signal yields are related to the actual number of tag-semileptonic combinations that occurred in each q^2 bin, n_i^α, via:

$$n_i^{\text{obs},\alpha} = \sum_j n_j^\alpha \epsilon_{ij}^\alpha, \tag{5.2}$$

where ϵ_{ij}^α are the elements of a matrix that describes the efficiency and smearing across q^2 bins associated with tag and semileptonic reconstruction. As the number of tag-semileptonic combinations that occurred is a function of the number of tag decays and the differential semileptonic decay rate, $d\Gamma/dq^2$, we can rewrite Eq. 5.2 as:

$$n_j^{\text{obs},\alpha} = N_{\text{tag}}^\alpha \tau_D \sum_i \epsilon_{ij}^\alpha \int_i \frac{d\Gamma}{dq^2} dq^2, \tag{5.3}$$

where the integration is over the width of q^2 bin i. Combining this with equation 5.1 and solving for the differential rate, we obtain a simple formula for extracting the partial rates:

$$\begin{aligned} \Delta\Gamma_i &\equiv \int_i \frac{d\Gamma}{dq^2} dq^2 \\ &= \frac{1}{\tau_D} \frac{\epsilon_{\text{tag}}^\alpha}{N_{\text{tag}}^{\text{obs},\alpha}} \sum_j \left(\epsilon^{-1}\right)_{ij}^\alpha n_j^{\text{obs},\alpha}. \end{aligned} \tag{5.4}$$

The following sections describe the extraction of the tag and signal yields ($N_{\text{tag}}^{\text{obs},\alpha}$ and $n_i^{\text{obs},\alpha}$), the tagging efficiencies ($\epsilon_{\text{tag}}^{\alpha}$) and the signal smearing and efficiency matrices ϵ_{ij}^{α}. With all of these numbers in hand, we then extract the partial rates.

5.1 Tag Yields

The beam constrained mass (M_{BC}) distributions of tag candidates in data passing all tag selection criteria except those on M_{BC} are shown in Figure 5.1. We fit these distributions using an unbinned likelihood fit that mirrors that used by a D hadronic analysis of the initial 281 pb^{-1} of CLEO-c data [29]. For the signal shape, we use three RooDLineShape functions, described in [30]. RooDLineShape is a probability density function designed to take into account the natural $\psi(3770)$ line shape, beam energy resolution, momentum resolution and initial state radiation effects. The relative widths and normalizations of the three signal shapes are fixed to values determined by the D hadronic analysis using Monte Carlo.

The line shape requires a number of input parameters, and we again use values from by the D Hadronic analysis: the mass and width of the $\psi(3770)$ are taken to be 3771.8 MeV and 28.5 MeV, respectively, the Blatt-Weisskopf interaction radius is set to 12.3 GeV^{-1} and the beam energy spread is fixed to 2.1 MeV. For the background shape, we use an ARGUS function [31], modified to allow the power parameter to float:

$$(M_{BC}; m_0, \xi, \rho) = A M_{bc} \left(1 - \frac{m^2}{m_0^2}\right)^{\rho} e^{\xi\left(1 - \frac{m^2}{m_0^2}\right)}. \tag{5.5}$$

The background and signal levels estimated by the fits are shown in Figure 5.1. Tag yields are estimated by counting candidates in the M_{BC} range given in Table 4.1 after subtracting the fitted background from the data distributions. The results are shown in Table 5.1.
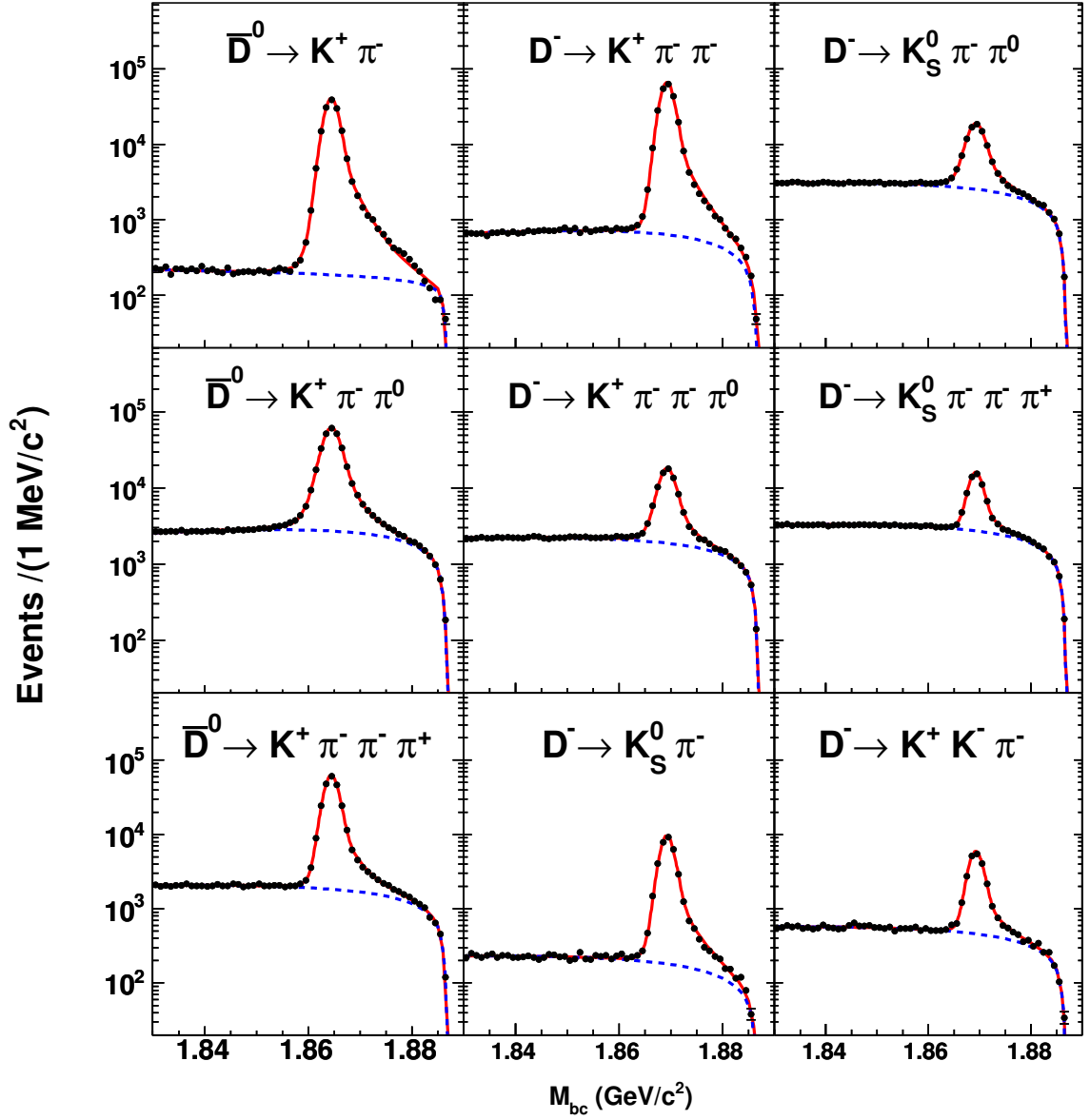
Figure 5.1: M_{BC} distributions of tag candidates in data (points), with fits (solid line) and background levels estimated by fits (dotted line).

Table 5.1: Tag Yields in Data

mode	Tag Yield in Data
$D^0 \to K^-\pi^+$	149616 ± 392
$D^0 \to K^-\pi^+\pi^0$	284617 ± 589
$D^0 \to K^-\pi^+\pi^+\pi^-$	227536 ± 517
$D^+ \to K^-\pi^+\pi^+$	233670 ± 497
$D^+ \to K^-\pi^+\pi^+\pi^0$	69798 ± 330
$D^+ \to K_S^0\pi^+$	33870 ± 194
$D^+ \to K_S^0\pi^+\pi^0$	74842 ± 357
$D^+ \to K^0\pi^+\pi^+\pi^-$	49117 ± 323
$D^+ \to K^+K^-\pi^+$	19926 ± 171

5.2 Tagging Efficiencies

We estimate tagging efficiencies from the generic Monte Carlo sample by first obtaining tag yields in Monte Carlo in the same manner described above for data, with some features in the signal lineshape altered such that:

- The mass of the $\psi(3770)$ is fixed to 3772.4 MeV

- The width of the $\psi(3770)$ is fixed to 23.5 MeV

- Blatt-Weisskopf interaction radius is set to 15 GeV^{-1}

The tag yields in Monte Carlo, along with the counted number of each tag decay at generator level and the resulting tagging efficiency for each mode is given in Table 5.2.

5.3 Signal Yields

D semileptonic signal yields can be extracted from a variety of distributions. We have chosen the distribution of a variable, termed 'U', which is the difference between the missing energy and missing momentum of an event:

$$U = E_{miss} - |\mathbf{P}_{miss}| \tag{5.6}$$

Table 5.2: Tag Yields and Efficiencies in Generic Monte Carlo

mode	Tag Yield	Number generated	Tag Efficiency (%)
$\bar{D}^0 \to K^+\pi^-$	2918504 ± 1709	4468232	65.32 ± 0.04
$\bar{D}^0 \to K^+\pi^-\pi^0$	5543510 ± 2491	15771736	35.15 ± 0.02
$\bar{D}^0 \to K^+\pi^-\pi^-\pi^+$	4326474 ± 2162	9498773	45.55 ± 0.02
$D^- \to K^+\pi^-\pi^-$	4879314 ± 2238	8804756	55.42 ± 0.03
$D^- \to K^+\pi^-\pi^-\pi^0$	1519769 ± 1410	5548121	27.39 ± 0.03
$D^- \to K^0\pi^-$	629478 ± 802	1231951	51.10 ± 0.07
$D^- \to K^0\pi^-\pi^0$	1579426 ± 1431	5502567	28.74 ± 0.03
$D^- \to K^0\pi^-\pi^-\pi^+$	1042612 ± 1193	2392207	43.58 ± 0.05
$D^- \to K^+K^-\pi^-$	389963 ± 689	927005	42.07 ± 0.07

where

$$E_{miss} = E_{beam} - E_{he}$$

$$\mathbf{P}_{miss} = -\mathbf{P}_{tag} - \mathbf{P}_{he} \qquad (5.7)$$

and

$$E_{he} = E_{K/\pi} + E_e + E_{brem}$$

$$\mathbf{P}_{he} = \mathbf{P}_{K/\pi} + \mathbf{P}_e + \mathbf{P}_{brem}. \qquad (5.8)$$

In these expressions, $P_{K/\pi}$ and $E_{K/\pi}$ are the measured momentum and energy of the kaon or pion, P_e and E_e are the measured momentum and energy of the electron, and E_{brem} and P_{brem} are the measured energy and momentum of any bremsstrahlung photons that were reconstructed. $\mathbf{P}_{tag}$ is the measured momentum of the tag, with magnitude constrained by the beam energy and mass of the D meson:

$$\mathbf{P}_{tag} = \sqrt{E_{beam}^2 - M_D^2} \, \hat{P}_{tag,meas}$$

All of the energy and momenta used to define U must be in a well defined frame; because the energy of each D is equal to the beam energy only in the e^+e^- center-of-mass frame,

this is a convenient choice. Momentum vectors measured in the laboratory frame are boosted to the center-of-mass frame by correcting for the small e^+e^- total momentum arising from the beam crossing angle.

U distributions in data are shown in figures 1-22. For semileptonic candidates which are correctly reconstructed, the missing neutrino causes the U distribution to peak at zero, the shape of the distribution being roughly Gaussian due to finite detector resolution. Misreconstructed candidates and various types of backgrounds generally have non-zero U values. Although other distributions, such as missing mass, could also be used, the U distribution has been found to have excellent signal to background separation.

Both $D^0 \rightarrow K^-e^+\nu_e$ and $D^+ \rightarrow \bar{K}^0e^+\nu_e$ have very small backgrounds that are dominated by $D \rightarrow K^*e\nu$, while the backgrounds in $D^0 \rightarrow \pi^-e^+\nu_e$ and $D^+ \rightarrow \pi^0e^+\nu_e$ are larger. The $D^+ \rightarrow \pi^0e^+\nu_e$ background is dominated by $D^+ \rightarrow \bar{K}^0e^+\nu_e \rightarrow \pi^0\pi^0e\nu$. Similarly, $D^0 \rightarrow K^-e^+\nu_e$ makes up a large portion of the $D^0 \rightarrow \pi^-e^+\nu_e$ background, but this mode is also affected by other significant backgrounds such as $D^0 \rightarrow \rho^-e^+\nu_e$.

5.3.1 Definition of q^2

Signal yields are binned in q^2, the invariant mass squared of the electron-neutrino system:

$$q^2 = (E_\nu + E_e)^2 - |\mathbf{P}_\nu + \mathbf{P}_e|^2 \tag{5.9}$$

We take the neutrino energy to be the missing energy of the event, defined as in U above. The neutrino momentum is defined as the missing momentum of the event constrained so that the magnitude of the missing momentum is equal to the missing energy:

$$\mathbf{P}_\nu = E_{miss}\hat{P}_{miss} \tag{5.10}$$

43

The calculation of q^2 is done in the e^+e^- center of mass frame. Measured in signal Monte Carlo, the q^2 resolution is approximately 0.008 GeV^2 in all modes but $D^+ \to \pi^0 e^+ \nu_e$, where it is 0.014 GeV^2.

For $D^0 \to \pi^- e^+ \nu_e$ and $D^+ \to \pi^0 e^+ \nu_e$, we divide our samples into 7 q^2 bins defined by: [0,0.3), [0.3,0.6), [0.6,0.9), [0.9,1.2), [1.2,1.5), [1.5,2.0), [2.0,∞) GeV^2. For $D^0 \to K^- e^+ \nu_e$ and $D^+ \to \bar{K}^0 e^+ \nu_e$, we use 9 q^2 bins defined by: [0,0.2), [0.2,0.4), [0.4,0.6), [0.6,0.8), [0.8,1.0), [1.0,1.2), [1.2,1.4), [1.4,1.6), [1.6,∞) GeV^2. In all cases, we fit the U distribution for each q^2 bin and each tag mode separately.

5.3.2   Fitting Shapes

For the signal shape, we take as a starting point the U distributions of signal Monte Carlo. Our studies find U resolutions in data are around 12 MeV in $D^0 \to \pi^- e^+ \nu_e$, $D^0 \to K^- e^+ \nu_e$ and $D^+ \to \bar{K}^0 e^+ \nu_e$ and 28 MeV in $D^+ \to \pi^0 e^+ \nu_e$. Monte Carlo U resolutions are slightly narrower: around 11 MeV in $D^0 \to \pi^- e^+ \nu_e$, $D^0 \to K^- e^+ \nu_e$ and $D^+ \to \bar{K}^0 e^+ \nu_e$ and 24 MeV in $D^+ \to \pi^0 e^+ \nu_e$. U distribution tails are also somewhat larger in data. As we have been unable to determine the cause of these discrepancies, we account for them by convolving the signal shape with a double Gaussian. The widths of the two Gaussians and their relative normalization are fixed to parameters that vary with semileptonic mode, and were determined by manually varying the parameters and choosing the value that minimized the likelihood (defined in Equation 5.11) summed over tag modes and q^2 bins. The width of the narrower(wider) Gaussian is fixed to 6(30), 5(30), 13(35) and 7(35) MeV for $D^0 \to \pi^- e^+ \nu_e$, $D^0 \to K^- e^+ \nu_e$, $D^+ \to \pi^0 e^+ \nu_e$ and $D^+ \to \bar{K}^0 e^+ \nu_e$ respectively, while the normalization of the second Gaussian is fixed to 5%, 4%, 7% and 3% of the first, for each mode respectively.

Treatment of background shapes varies somewhat with semileptonic mode. Each mode has a very small background from non-$D\bar{D}$ sources ($ee \to q\bar{q}$ continuum, radiative

returns and $ee \rightarrow \tau\tau$). We take the shape of this background from the Monte Carlo samples for these sources, which are equivalent to five times the data luminosity, and fix the normalization of this shape to 1/5. All $D\bar{D}$ backgrounds are taken from the 20x generic Monte Carlo Samples. The normalizations of the $D^+ \rightarrow \bar{K}^0 e^+ \nu_e$ background to $D^+ \rightarrow \pi^0 e^+ \nu_e$ and the $D^0 \rightarrow K^- e^+ \nu_e$ background to $D^0 \rightarrow \pi^- e^+ \nu_e$ are fixed to the values that minimize the combined likelihood for all q^2 bins and all tag modes. If branching fractions and fake rates were exactly correct in the Monte Carlo, we would expect this normalization to be 0.05 (the ratio of luminosities in data and Monte Carlo). However, we find that the chisquare minimizing values are 0.039 for $D^+ \rightarrow \bar{K}^0 e^+ \nu_e$ and 0.061 for $D^0 \rightarrow K^- e^+ \nu_e$. The high normalization preferred for $D^0 \rightarrow K^- e^+ \nu_e$ indicates that the $K^\pm \rightarrow \pi^\pm$ fake rate is higher in data than in Monte Carlo. This is compatible with studies of $\pi^\pm$ and $K^\pm$ fake rates found in [32] and [29]. Most of the $D^+ \rightarrow \bar{K}^0 e^+ \nu_e$ background to $D^+ \rightarrow \pi^0 e^+ \nu_e$ is due to $K^0_S \rightarrow \pi^0 \pi^0$ decays. The lower normalization preferred for this background indicates that the π^0 finding efficiency is $\approx 10\%$ per π^0 lower in data than in Monte Carlo. This is the same sign and scale found in CLEO-c π^0 finding systematics studies [33]. In $D^0 \rightarrow \pi^- e^+ \nu_e$, we fix the background from $D^0 \rightarrow \rho^- e^+ \nu_e$ to the ratio of tag yields in data and Monte Carlo. In each semileptonic mode, all $D\bar{D}$ background modes not mentioned above are combined into a single shape whose normalization is allowed to float.

5.3.3 Fitting Function

To extract semileptonic signal yields, we use a binned likelihood fitting technique described in [22]. We vary fit parameters $\vec{\theta}$ in order to optimize agreement between the expected number of candidates in each bin of the U distribution ($\vec{\nu}(\vec{\theta}) = \nu_1(\vec{\theta}), ..., \nu_N(\vec{\theta})$)

and the number observed in data ($\vec{n} = n_1, ..., n_N$). The optimal parameters minimize:

$$-2 \ln L(\theta) = 2 \sum_{i=1}^{N} \left[\nu_i(\theta) - n_i + n_i \ln \frac{n_i}{\nu_i(\theta)} \right]. \tag{5.11}$$

In bins where the number of observed candidates is zero, the last term is zero. The last term is not well defined in the case where the number of observed candidates is non-zero but the number predicted is zero. This can occur due to finite Monte Carlo statistics or incorrect modeling of backgrounds in the Monte Carlo. In cases where the Monte Carlo predicts zero candidates but where there are nonzero candidates in data, we set the number of expected candidates to ≈ 0.05, equivalent to one event being present in the Monte Carlo. The actual number used by the fitter is taken from the ratio of tag yields in data and Monte Carlo for the tag mode in question.

For example, in the case of $D^0 \to \pi^- e^+ \nu_e$, the expected number of candidates in bin i is:

$$\nu_i = x_{sig} N_{sig,i} + x_{kenu} N_{kev,i} + \frac{N_{tag,data}}{N_{tag,MC}} N_{\rho ev} + x_{other} N_{other,i},$$

where $N_{sig,i}$, N_{Kev}, $N_{\rho ev,i}$ are the number of $D^0 \to \pi^- e^+ \nu_e$ (after the double Gaussian smear), $D^0 \to K^- e^+ \nu_e$ and $D^0 \to \rho^- e^+ \nu_e$ candidates in ith bin of the Monte Carlo U distributions. The number of events in all modes other than $D^0 \to \pi^- e^+ \nu_e$, $D^0 \to K^- e^+ \nu_e$ and $D^0 \to \rho^- e^+ \nu_e$ is given by $N_{other,i}$. The fitting parameters are x_{sig} and x_{other} – the normalizations of the signal and combined background shapes respectively. The normalization of the fixed $D^0 \to K^- e^+ \nu_e$ background is given by x_{kev}.

5.3.4 Signal Yield Results

The results of the signal yield fits, including final fit parameters, signal yields and log-likelihoods are shown in Tables 5.3 - 5.7. The signal yield for a particular fit is taken from the normalization of the signal shape. An advantage of a binned likelihood fit is that, unlike an unbinned likelihood fit, it allows a goodness of fit test, since, for large

sample sizes, the likelihood function given in Eq. 5.11 obeys a χ^2 distribution [22].

Given the 17 U bins used in the fits and 2 free parameters of the fit, we would expect the

likelihoods to be around 15 ± 6. The fits themselves and residuals summed over q^2 are

available in Figures 1-26 of the Appendix.

Table 5.3: Signal Yield Fit Results for $D^0 \rightarrow \pi^- e^+ \nu_e$. Fit parameters x_{sig} and x_{other} give the normalizations of the signal and 'other' background shapes.

Tag Mode	q^2 bin	x_{sig}	x_{other}	-2lnL	Yield
$K\pi$	1	0.007±0.001	0.060±0.016	19	58±8
$K\pi$	2	0.005±0.001	0.035±0.015	24	41±7
$K\pi$	3	0.006±0.001	0.056±0.019	15	51±7
$K\pi$	4	0.007±0.001	0.029±0.016	14	48±7
$K\pi$	5	0.007±0.001	0.000±0.013	17	41±7
$K\pi$	6	0.005±0.001	0.020±0.016	11	40±7
$K\pi$	7	0.007±0.001	0.073±0.010	5	34±6
$K\pi\pi^0$	1	0.006±0.001	0.066±0.011	13	96±10
$K\pi\pi^0$	2	0.006±0.001	0.044±0.011	13	106±11
$K\pi\pi^0$	3	0.006±0.001	0.048±0.014	19	89±10
$K\pi\pi^0$	4	0.006±0.001	0.049±0.014	22	89±10
$K\pi\pi^0$	5	0.006±0.001	0.028±0.015	16	74±9
$K\pi\pi^0$	6	0.005±0.001	0.048±0.012	20	78±9
$K\pi\pi^0$	7	0.007±0.001	0.062±0.006	32	68±9
$K\pi\pi\pi$	1	0.007±0.001	0.043±0.012	12	96±10
$K\pi\pi\pi$	2	0.007±0.001	0.085±0.016	16	85±10
$K\pi\pi\pi$	3	0.006±0.001	0.072±0.019	27	64±9
$K\pi\pi\pi$	4	0.006±0.001	0.059±0.015	15	57±8
$K\pi\pi\pi$	5	0.005±0.001	0.087±0.022	22	46±7
$K\pi\pi\pi$	6	0.005±0.001	0.065±0.015	10	56±8
$K\pi\pi\pi$	7	0.008±0.001	0.069±0.008	21	57±8

Table 5.4: Signal Yield Fit Results for $D^0 \rightarrow K^- e^+ \nu_e$. Fit parameters x_{sig} and x_{other} give the normalizations of the signal and 'other' background shapes.

Tag Mode	q^2 bin	x_{sig}	x_{other}	-2lnL	Yield
$K\pi$	1	0.0072±0.0003	0.0556±0.0088	9	603±25
$K\pi$	2	0.0070±0.0003	0.0517±0.0100	7	544±24
$K\pi$	3	0.0077±0.0003	0.0595±0.0110	15	548±24
$K\pi$	4	0.0070±0.0003	0.0438±0.0095	8	435±21
$K\pi$	5	0.0075±0.0004	0.0376±0.0091	10	386±20
$K\pi$	6	0.0069±0.0004	0.0367±0.0093	17	266±17
$K\pi$	7	0.0073±0.0005	0.0500±0.0111	9	192±14
$K\pi$	8	0.0067±0.0007	0.0751±0.0136	10	95±10
$K\pi$	9	0.0098±0.0015	0.0563±0.0145	15	44±7
$K\pi\pi^0$	1	0.0074±0.0002	0.0391±0.0052	33	1239±36
$K\pi\pi^0$	2	0.0072±0.0002	0.0473±0.0071	12	1112±34
$K\pi\pi^0$	3	0.0068±0.0002	0.0595±0.0081	19	947±32
$K\pi\pi^0$	4	0.0074±0.0003	0.0495±0.0072	5	912±31
$K\pi\pi^0$	5	0.0071±0.0003	0.0477±0.0069	21	727±28
$K\pi\pi^0$	6	0.0072±0.0003	0.0555±0.0075	10	548±24
$K\pi\pi^0$	7	0.0078±0.0004	0.0384±0.0071	15	401±21
$K\pi\pi^0$	8	0.0079±0.0005	0.0622±0.0088	17	221±15
$K\pi\pi^0$	9	0.0073±0.0010	0.0619±0.0114	28	65±9
$K\pi\pi\pi$	1	0.0073±0.0002	0.0473±0.0067	17	909±31
$K\pi\pi\pi$	2	0.0077±0.0003	0.0513±0.0084	21	885±30
$K\pi\pi\pi$	3	0.0079±0.0003	0.0562±0.0087	11	831±30
$K\pi\pi\pi$	4	0.0075±0.0003	0.0358±0.0072	24	688±27
$K\pi\pi\pi$	5	0.0072±0.0003	0.0565±0.0077	17	549±24
$K\pi\pi\pi$	6	0.0075±0.0004	0.0361±0.0073	16	429±21
$K\pi\pi\pi$	7	0.0081±0.0005	0.0453±0.0082	11	310±18
$K\pi\pi\pi$	8	0.0085±0.0007	0.0627±0.0101	21	180±14
$K\pi\pi\pi$	9	0.0086±0.0012	0.0445±0.0101	14	57±8

Table 5.5: Signal Yield Fit Results for $D^+ \rightarrow \pi^0 e^+ \nu_e$. Fit parameters x_{sig} and x_{other} give the normalizations of the signal and 'other' background shapes.

Tag Mode	q^2 bin	x_{sig}	x_{other}	-2lnL	Yield
$K\pi\pi$	1	0.007±0.001	0.109±0.044	22	71±9
$K\pi\pi$	2	0.008±0.001	0.122±0.077	26	71±9
$K\pi\pi$	3	0.007±0.001	0.000±0.061	23	56±8
$K\pi\pi$	4	0.008±0.001	0.046±0.061	10	59±8
$K\pi\pi$	5	0.009±0.001	0.202±0.081	21	51±8
$K\pi\pi$	6	0.008±0.001	0.022±0.035	22	59±9
$K\pi\pi$	7	0.006±0.001	0.090±0.026	25	43±9
$K\pi\pi\pi^0$	1	0.007±0.002	0.088±0.058	10	20±5
$K\pi\pi\pi^0$	2	0.006±0.002	0.080±0.082	17	19±5
$K\pi\pi\pi^0$	3	0.009±0.002	0.260±0.112	17	23±5
$K\pi\pi\pi^0$	4	0.008±0.002	0.000±0.021	13	19±5
$K\pi\pi\pi^0$	5	0.003±0.002	0.096±0.102	18	7±4
$K\pi\pi\pi^0$	6	0.008±0.002	0.031±0.042	15	17±5
$K\pi\pi\pi^0$	7	0.004±0.002	0.100±0.040	11	9±5
$K^0\pi$	1	0.010±0.003	0.096±0.117	11	14±4
$K^0\pi$	2	0.008±0.003	0.000±1.007	18	10±3
$K^0\pi$	3	0.008±0.003	0.028±0.161	22	9±3
$K^0\pi$	4	0.009±0.003	0.000±0.062	16	9±3
$K^0\pi$	5	0.004±0.003	0.015±0.317	12	3±2
$K^0\pi$	6	0.003±0.002	0.687±0.291	17	3±2
$K^0\pi$	7	0.009±0.004	0.169±0.078	8	7±3
$K^0\pi\pi^0$	1	0.008±0.002	0.017±0.055	39	26±5
$K^0\pi\pi^0$	2	0.008±0.002	0.214±0.119	19	24±5
$K^0\pi\pi^0$	3	0.005±0.002	0.006±0.258	9	15±4
$K^0\pi\pi^0$	4	0.006±0.002	0.010±0.108	8	13±4
$K^0\pi\pi^0$	5	0.012±0.003	0.015±0.061	12	24±5
$K^0\pi\pi^0$	6	0.006±0.002	0.000±0.387	11	15±4
$K^0\pi\pi^0$	7	0.013±0.003	0.054±0.037	17	25±6
$K^0\pi\pi\pi$	1	0.006±0.002	0.167±0.101	13	12±4
$K^0\pi\pi\pi$	2	0.007±0.002	0.000±0.049	19	14±4
$K^0\pi\pi\pi$	3	0.007±0.002	0.000±0.097	18	12±4
$K^0\pi\pi\pi$	4	0.011±0.003	0.000±0.060	8	17±4
$K^0\pi\pi\pi$	5	0.008±0.003	0.000±0.166	11	10±3
$K^0\pi\pi\pi$	6	0.007±0.003	0.039±0.073	23	10±4
$K^0\pi\pi\pi$	7	0.009±0.003	0.000±0.028	21	13±5
$KK\pi$	1	0.005±0.004	0.055±0.077	22	4±3
$KK\pi$	2	0.007±0.004	0.054±0.100	17	5±3
$KK\pi$	3	0.016±0.005	0.000±0.038	14	10±3
$KK\pi$	4	0.007±0.004	0.000±0.023	16	4±2
$KK\pi$	5	0.009±0.005	0.000±0.128	20	4±2
$KK\pi$	6	0.004±0.004	0.134±0.077	19	2±2
$KK\pi$	7	0.000±0.004	0.133±0.052	19	0±2

Table 5.6: Signal Yield Fit Results for $D^+ \rightarrow \bar{K}^0 e^+ \nu_e$, first three tag modes. Fit parameters x_{sig} and x_{other} give the normalizations of the signal and 'other' background shapes

Tag Mode	q^2 bin	x_{sig}	x_{other}	-2lnL	Yield
$K\pi\pi$	1	0.0083±0.0003	0.0314±0.0062	13	846±30
$K\pi\pi$	2	0.0080±0.0003	0.0649±0.0093	25	738±28
$K\pi\pi$	3	0.0085±0.0003	0.0423±0.0077	16	695±27
$K\pi\pi$	4	0.0086±0.0004	0.0445±0.0078	14	610±25
$K\pi\pi$	5	0.0078±0.0004	0.0509±0.0080	17	446±22
$K\pi\pi$	6	0.0095±0.0005	0.0483±0.0088	23	419±21
$K\pi\pi$	7	0.0078±0.0005	0.0590±0.0089	20	245±16
$K\pi\pi$	8	0.0078±0.0007	0.0423±0.0075	14	144±12
$K\pi\pi$	9	0.0089±0.0012	0.0535±0.0089	9	66±9
$K\pi\pi\pi^0$	1	0.0074±0.0005	0.0457±0.0131	5	235±16
$K\pi\pi\pi^0$	2	0.0084±0.0005	0.0250±0.0113	24	239±16
$K\pi\pi\pi^0$	3	0.0071±0.0005	0.0456±0.0145	14	182±14
$K\pi\pi\pi^0$	4	0.0083±0.0006	0.0709±0.0162	26	181±14
$K\pi\pi\pi^0$	5	0.0075±0.0007	0.0738±0.0164	15	133±12
$K\pi\pi\pi^0$	6	0.0077±0.0008	0.0351±0.0116	21	104±11
$K\pi\pi\pi^0$	7	0.0066±0.0009	0.0618±0.0157	23	64±8
$K\pi\pi\pi^0$	8	0.0056±0.0010	0.0411±0.0122	15	32±6
$K\pi\pi\pi^0$	9	0.0082±0.0021	0.0459±0.0141	18	18±5
$K^0\pi$	1	0.0089±0.0008	0.0712±0.0229	11	118±11
$K^0\pi$	2	0.0104±0.0010	0.0106±0.0155	15	123±11
$K^0\pi$	3	0.0084±0.0009	0.0409±0.0208	18	90±10
$K^0\pi$	4	0.0101±0.0011	0.0677±0.0262	17	90±10
$K^0\pi$	5	0.0087±0.0011	0.0711±0.0268	23	62±8
$K^0\pi$	6	0.0094±0.0013	0.0642±0.0275	19	53±8
$K^0\pi$	7	0.0109±0.0017	0.0353±0.0193	10	44±7
$K^0\pi$	8	0.0105±0.0021	0.0707±0.0239	23	25±5
$K^0\pi$	9	0.0120±0.0037	0.0470±0.0243	19	11±4

Table 5.7: Signal Yield Fit Results for $D^+ \rightarrow \bar{K}^0 e^+ \nu_e$, second three tag modes. Fit parameters x_{sig} and x_{other} give the normalizations of the signal and 'other' background shapes

Tag Mode	q^2 bin	x_{sig}	x_{other}	-2lnL	Yield
$K^0\pi\pi^0$	1	0.0081±0.0005	0.0333±0.0101	19	265±17
$K^0\pi\pi^0$	2	0.0070±0.0005	0.0632±0.0155	15	205±15
$K^0\pi\pi^0$	3	0.0084±0.0006	0.0443±0.0143	15	222±15
$K^0\pi\pi^0$	4	0.0086±0.0006	0.0122±0.0092	17	196±14
$K^0\pi\pi^0$	5	0.0075±0.0007	0.0202±0.0101	28	139±12
$K^0\pi\pi^0$	6	0.0080±0.0008	0.0439±0.0127	20	114±11
$K^0\pi\pi^0$	7	0.0092±0.0010	0.0511±0.0139	9	93±10
$K^0\pi\pi^0$	8	0.0069±0.0011	0.0255±0.0109	16	40±7
$K^0\pi\pi^0$	9	0.0063±0.0017	0.0457±0.0138	12	14±4
$K^0\pi\pi\pi$	1	0.0080±0.0006	0.0534±0.0156	21	173±13
$K^0\pi\pi\pi$	2	0.0075±0.0006	0.0357±0.0157	14	147±12
$K^0\pi\pi\pi$	3	0.0079±0.0007	0.0380±0.0163	14	136±12
$K^0\pi\pi\pi$	4	0.0075±0.0007	0.0597±0.0161	16	111±11
$K^0\pi\pi\pi$	5	0.0082±0.0009	0.0665±0.0203	23	97±10
$K^0\pi\pi\pi$	6	0.0086±0.0010	0.0642±0.0202	11	79±9
$K^0\pi\pi\pi$	7	0.0076±0.0011	0.0719±0.0199	11	49±7
$K^0\pi\pi\pi$	8	0.0068±0.0014	0.0329±0.0150	20	26±5
$K^0\pi\pi\pi$	9	0.0060±0.0021	0.0420±0.0168	17	9±3
$KK\pi$	1	0.0081±0.0010	0.0581±0.0248	20	67±8
$KK\pi$	2	0.0082±0.0011	0.0085±0.0152	10	59±8
$KK\pi$	3	0.0097±0.0012	0.0102±0.0141	11	64±8
$KK\pi$	4	0.0073±0.0012	0.0872±0.0306	17	41±7
$KK\pi$	5	0.0076±0.0013	0.0290±0.0227	12	35±6
$KK\pi$	6	0.0115±0.0018	0.0201±0.0178	8	40±6
$KK\pi$	7	0.0078±0.0019	0.0632±0.0294	8	19±5
$KK\pi$	8	0.0056±0.0020	0.0625±0.0294	12	8±3
$KK\pi$	9	0.0082±0.0041	0.0488±0.0274	9	5±2

5.4   Signal Efficiency Matrices

In 5.3, we described our extraction of signal yields in bins of q^2. These yields differ from the true spectra because of reconstruction inefficiency and smearing of the reconstructed q^2, which moves some events out of the correct q^2 bin. To handle both of these effects, we define an efficiency matrix ϵ_{ij}^α that relates the number of reconstructed decays in the ith bin ($n_i^{obs,\alpha}$) to the number that occurred in the jth bin (n_j^α). The superscript α refers to the tag mode. Specifically,

$$n_j^{obs,\alpha} = \sum_i n_i^\alpha \epsilon_{ji}^\alpha. \tag{5.12}$$

where the summation is over the number of q^2 bins (seven for $D^0 \to \pi^- e^+ \nu_e$ and $D^+ \to \pi^0 e^+ \nu_e$ and nine for $D^0 \to K^- e^+ \nu_e$ and $D^+ \to \bar{K}^0 e^+ \nu_e$).

We determine the efficiency matrix separately for each tag and semileptonic mode using the signal Monte Carlo, reweighted for known biases in the electron reconstruction and hadron identification efficiencies. Each ϵ_{ij}^α gives the fraction of events generated in q^2 bin j with tag mode α that are reconstructed in q^2 bin i with the same tag. The efficiency matrix thus accounts for reconstruction of both the signal decay and the tag. In the case of $D^+ \to \bar{K}^0 e^+ \nu_e$, the efficiency matrix includes the $K_S \to \pi^+ \pi^-$ branching fraction and the K_S amplitude. The efficiency matrices for $D^0 \to \pi^- e^+ \nu_e$ and $D^0 \to K^- e^+ \nu_e$ versus the $\bar{D}^0 \to K^+ \pi^-$ tag and for $D^+ \to \pi^0 e^+ \nu_e$ and $D^+ \to \bar{K}^0 e^+ \nu_e$ versus the $D^- \to K^+ \pi^- \pi^-$ tag are shown in Table 5.8. The diagonal elements range from about 0.05 to 0.5 depending on the semileptonic and tag mode, and the correlation coefficient between neighboring bins ranges between 2% and 15% depending on the semileptonic and tag mode.

Table 5.8: Selected efficiency matrices in percent. Columns give the true q^2 bin i, while rows give the reconstructed (Rec) q^2 bin j. The elements account for the reconstruction efficiencies of both the tag and the semileptonic decay. The statistical uncertainties in the least significant digits are given in the parentheses.

$D^0 \to \pi^- e^+ \nu_e, \bar{D}^0 \to K^+ \pi^-$

Rec q^2 (GeV^2)	True q^2 (GeV^2)						
	[0,0.3]	[0.3,0.6]	[0.6,0.9]	[0.9,1.2]	[1.2,1.5]	[1.5,2.0]	[2.0,∞)
[0, 0.3]	40.99(34)	1.18(8)	0.02(1)	0.00(0)	0.00(0)	0.00(0)	0.00(0)
[0.3, 0.6]	0.76(6)	42.39(36)	1.55(10)	0.01(1)	0.00(0)	0.00(0)	0.00(0)
[0.6, 0.9]	0.04(1)	1.12(8)	44.56(38)	1.54(10)	0.02(1)	0.00(0)	0.00(0)
[0.9, 1.2]	0.02(1)	0.08(2)	1.09(8)	45.73(41)	1.37(10)	0.03(1)	0.00(0)
[1.2, 1.5]	0.01(1)	0.03(1)	0.09(2)	1.33(9)	46.09(44)	0.91(8)	0.00(0)
[1.5, 2.0]	0.01(1)	0.02(1)	0.02(1)	0.11(3)	1.20(10)	47.00(40)	0.74(8)
[2.0, ∞)	0.00(0)	0.00(0)	0.01(1)	0.02(1)	0.04(2)	0.56(6)	47.32(48)

$D^0 \to K^- e^+ \nu_e, \bar{D}^0 \to K^+ \pi^-$

Rec q^2 (GeV^2)	True q^2 (GeV^2)								
	[0,0.2]	[0.2,0.4]	[0.4,0.6]	[0.6,0.8]	[0.8,1.0]	[1.0,1.2]	[1.2,1.4]	[1.4,1.6]	[1.6,∞)
[0, 0.2]	35.13(10)	1.27(2)	0.04(1)	0.00(0)	0.00(0)	0.00(0)	0.00(0)	0.00(0)	0.00(0)
[0.2, 0.4]	0.0069(2)	35.57(11)	1.63(3)	0.05(1)	0.00(0)	0.01(0)	0.00(0)	0.00(0)	0.00(0)
[0.4, 0.6]	0.0002(0)	0.0086(2)	37.18(11)	1.83(3)	0.06(1)	0.01(0)	0.01(0)	0.01(0)	0.01(1)
[0.6, 0.8]	0.01(0)	0.02(0)	0.95(2)	38.40(13)	1.81(4)	0.05(1)	0.00(0)	0.00(0)	0.00(0)
[0.8, 1.0]	0.01(0)	0.02(0)	0.05(1)	1.00(3)	39.31(14)	1.65(4)	0.04(1)	0.01(0)	0.00(0)
[1.0, 1.2]	0.01(0)	0.01(0)	0.03(0)	0.04(1)	0.91(3)	38.95(16)	1.55(5)	0.01(1)	0.00(0)
[1.2, 1.4]	0.00(0)	0.00(0)	0.01(0)	0.01(0)	0.04(1)	0.81(3)	38.41(19)	1.49(6)	0.00(0)
[1.4, 1.6]	0.00(0)	0.00(0)	0.00(0)	0.00(0)	0.01(0)	0.02(0)	0.0063(3)	36.41(25)	1.24(9)
[1.6, ∞)	0.00(0)	0.00(0)	0.00(0)	0.00(0)	0.00(0)	0.00(0)	0.01(0)	0.40(3)	30.10(38)

$D^+ \to \pi^0 e^+ \nu_e, D^- \to K^+ \pi^- \pi^-$

Rec q^2 (GeV^2)	True q^2 (GeV^2)						
	[0,0.3]	[0.3,0.6]	[0.6,0.9]	[0.9,1.2]	[1.2,1.5]	[1.5,2.0]	[2.0,∞)
[0, 0.3]	22.44(20)	0.83(5)	0.02(1)	0.00(0)	0.00(0)	0.00(0)	0.00(0)
[0.3, 0.6]	1.23(5)	21.69(21)	1.02(5)	0.01(1)	0.00(0)	0.00(0)	0.00(0)
[0.6, 0.9]	0.03(1)	1.62(6)	0.2123(22)	1.14(6)	0.01(1)	0.00(0)	0.00(0)
[0.9, 1.2]	0.02(1)	0.03(1)	1.75(7)	2.112(23)	1.05(6)	0.00(0)	0.00(0)
[1.2, 1.5]	0.02(1)	0.03(1)	0.06(1)	1.61(7)	19.72(25)	0.65(4)	0.00(0)
[1.5, 2.0]	0.02(1)	0.03(1)	0.04(1)	0.13(2)	1.47(7)	20.50(22)	0.49(5)
[2.0, ∞)	0.17(2)	0.19(2)	0.31(3)	0.47(4)	0.70(5)	1.65(7)	22.81(27)

$D^+ \to \bar{K}^0 e^+ \nu_e, D^- \to K^+ \pi^- \pi^-$

Rec q^2 (GeV^2)	True q^2 (GeV^2)								
	[0,0.2]	[0.2,0.4]	[0.4,0.6]	[0.6,0.8]	[0.8,1.0]	[1.0,1.2]	[1.2,1.4]	[1.4,1.6]	[1.6,∞)
[0, 0.2]	20.62(6)	0.01(1)	0.00(0)	0.00(0)	0.00(0)	0.00(0)	0.00(0)	0.00(0)	0.00(0)
[0.2, 0.4]	0.00(1)	20.31(6)	0.01(2)	0.00(0)	0.00(0)	0.00(0)	0.00(0)	0.00(0)	0.00(0)
[0.4, 0.6]	0.00(0)	0.01(1)	20.54(7)	0.01(2)	0.00(0)	0.00(0)	0.00(0)	0.00(0)	0.00(0)
[0.6, 0.8]	0.00(0)	0.00(0)	0.01(1)	21.07(7)	0.01(2)	0.00(0)	0.00(0)	0.00(0)	0.00(0)
[0.8, 1.0]	0.00(0)	0.00(0)	0.00(0)	0.01(1)	21.07(8)	0.01(2)	0.00(0)	0.00(0)	0.00(0)
[1.0, 1.2]	0.00(0)	0.00(0)	0.00(0)	0.00(0)	0.01(1)	21.10(9)	0.01(4)	0.00(0)	0.00(0)
[1.2, 1.4]	0.00(0)	0.00(0)	0.00(0)	0.00(0)	0.00(0)	0.01(2)	21.63(15)	0.01(3)	0.0000(0)
[1.4, 1.6]	0.00(0)	0.00(0)	0.00(0)	0.00(0)	0.00(0)	0.00(0)	0.01(3)	21.89(15)	0.01(6)
[1.6, ∞)	0.00(0)	0.00(0)	0.00(0)	0.00(0)	0.00(0)	0.00(0)	0.00(1)	0.00(2)	22.42(24)

Table 5.9: The partial rates and statistical covariance matrix for $D^0 \to \pi^- e^+ \nu_e$. The statistical uncertainties in the least significant digits are given in the parentheses.

	q^2 (GeV^2)						
	[0,0.3)	[0.3,0.6)	[0.6,0.9)	[0.9,1.2)	[1.2,1.5)	[1.5,2.0)	[2.1,∞)
$\Delta\Gamma(\text{sec}^{-1})$	1.40(9)	1.23(8)	1.02(8)	0.97(7)	0.78(7)	0.84(7)	0.79(6)
q^2 (GeV^2)							
[0.0, 0.3)	0.0091	-0.0004	0	0	0	0	0
[0.3, 0.6)	-0.0004	0.008	-0.0004	0	0	0	0
[0.6, 0.9)	0	-0.0004	0.0065	-0.0003	0	0	0
[0.9, 1.2)	0	0	-0.0003	0.0062	-0.0003	0	0
[1.2, 1.5)	0	0	0	-0.0003	0.0049	-0.0002	0
[1.5, 2.0)	0	0	0	0	-0.0002	0.005	-0.0001
[2.0, ∞)	0	0	0	0	0	-0.0001	0.0047

Table 5.10: The partial rates and statistical covariance matrix for $D^0 \to K^- e^+ \nu_e$. The statistical uncertainties in the least significant digits are given in the parentheses.

	q^2 (GeV^2)								
	[0,0.2)	[0.2,0.4)	[0.4,0.6)	[0.6,0.8)	[0.8,1.0)	[1.0,1.2)	[1.2,1.4)	[1.4,1.6)	[1.6,∞)
$\Delta\Gamma(\text{sec}^{-1})$	17.84(36)	15.85(34)	13.91(32)	11.68(28)	9.36(25)	7.08(22)	5.34(19)	3.07(15)	1.27(10)
q^2 (GeV^2)									
[0.0, 0.2)	0.1317	-0.0068	0.0006	0.0003	0.0002	0.0002	0.0001	0	0
[0.2, 0.4)	-0.0068	0.1204	-0.0075	0.0005	0.0002	0.0001	0.0001	0	0
[0.4, 0.6)	0.0006	-0.0075	0.103	-0.0066	0.0003	0	0.0001	0	0
[0.6, 0.8)	0.0003	0.0005	-0.0066	0.0833	-0.0052	0.0002	0	0	0
[0.8, 1.0)	0.0002	0.0002	0.0003	-0.0052	0.0651	-0.0036	0.0001	0	0
[1.0, 1.2)	0.0002	0.0001	0	0.0002	-0.0036	0.0495	-0.0025	0	0
[1.2, 1.4)	0.0001	0.0001	0.0001	0	0.0001	-0.0025	0.0377	-0.0015	0
[1.4, 1.6)	0	0	0	0	0	0	-0.0015	0.0227	-0.0007
[1.6, ∞)	0	0	0	0	0	0	0	-0.0007	0.0115

Table 5.11: The partial rates and statistical covariance matrix for $D^+ \to \pi^0 e^+ \nu_e$. The statistical uncertainties in the least significant digits are given in the parentheses.

	q^2 (GeV^2)						
	[0,0.3)	[0.3,0.6)	[0.6,0.9)	[0.9,1.2)	[1.2,1.5)	[1.5,2.0)	[2.1,∞)
$\Delta\Gamma$(sec^{-1})	0.71(6)	0.65(6)	0.56(6)	0.56(6)	0.48(6)	0.53(6)	0.37(6)
q^2 (GeV^2)							
[0.0, 0.3)	0.0043	-0.0004	0	0	0	0	0
[0.3, 0.6)	-0.0004	0.0045	-0.0005	0	0	0	0
[0.6, 0.9)	0	-0.0005	0.004	-0.0005	0	0	0
[0.9, 1.2)	0	0	-0.0005	0.004	-0.0005	0	0
[1.2, 1.5)	0	0	0	-0.0005	0.0042	-0.0004	0
[1.5, 2.0)	0	0	0	0	-0.0004	0.0044	-0.0004
[2.0, ∞)	0	0	0	0	0	-0.0004	0.0045

Table 5.12: The partial rates and statistical covariance matrix for $D^+ \to \bar{K}^0 e^+ \nu_e$. The statistical uncertainties in the least significant digits are given in the parentheses.

	q^2 (GeV^2)								
	[0,0.2)	[0.2,0.4)	[0.4,0.6)	[0.6,0.8)	[0.8,1.0)	[1.0,1.2)	[1.2,1.4)	[1.4,1.6)	[1.6,∞)
$\Delta\Gamma$(sec^{-1})	17.79(46)	15.62(45)	14.02(42)	12.28(39)	8.92(34)	8.16(32)	4.96(25)	2.66(18)	1.18(12)
q^2 (GeV^2)									
[0.0, 0.2)	0.2196	-0.0115	0.0009	0.0005	0.0004	0.0003	0.0002	0	0
[0.2, 0.4)	-0.0115	0.2054	-0.0131	0.0009	0.0003	0.0003	0.0001	0	0
[0.4, 0.6)	0.0009	-0.0131	0.1819	-0.0118	0.0006	0.0002	0.0001	0	0
[0.6, 0.8)	0.0005	0.0009	-0.0118	0.1569	-0.0095	0.0005	0	0	0
[0.8, 1.0)	0.0004	0.0003	0.0006	-0.0095	0.1159	-0.0077	0.0002	0	0
[1.0, 1.2)	0.0003	0.0003	0.0002	0.0005	-0.0077	0.1054	-0.0051	0.0001	0
[1.2, 1.4)	0.0002	0.0001	0.0001	0	0.0002	-0.0051	0.0626	-0.0026	0
[1.4, 1.6)	0	0	0	0	0	0.0001	-0.0026	0.0337	-0.0012
[1.6, ∞)	0	0	0	0	0	0	0	-0.0012	0.0159

5.5 Partial Rate Results
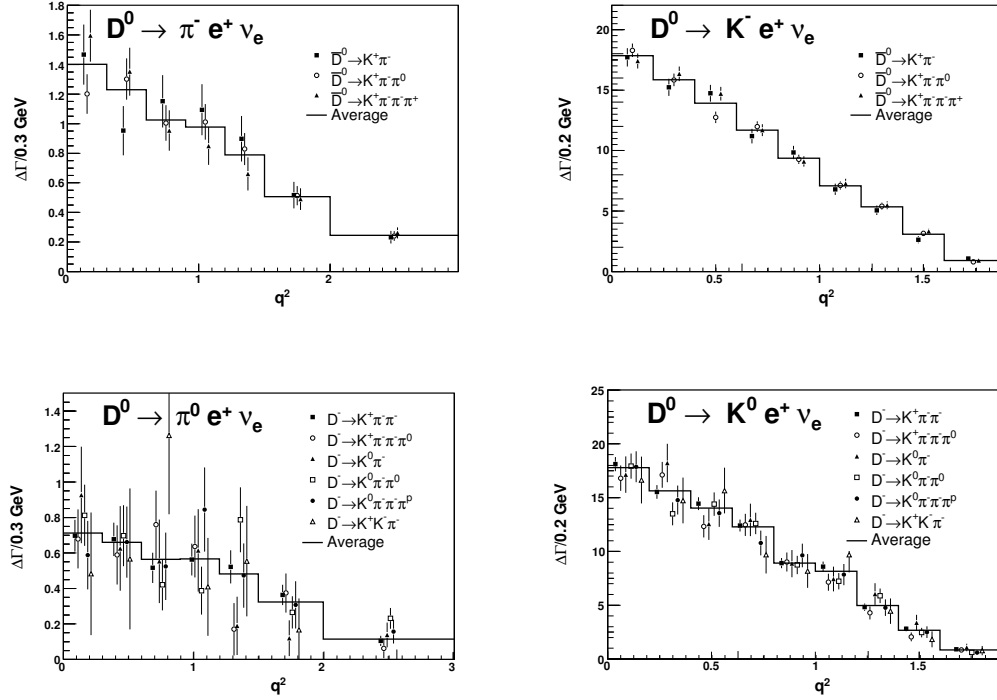
Figure 5.2: The partial rate distributions measured in the various tag modes (points), and the weighted average over tag modes (solid line).

Armed with the tag yields, tag efficiencies, signal yields and signal efficiency matrices, we use Eq. 5.4 to solve for the partial rates in each q^2 bin and tag mode, $\Delta\Gamma_i^\alpha$. We then average these over tag modes, obtaining $\Delta\Gamma_i$, which are shown in Tables 5.9 - 5.12 along with their statistical covariance matrices. We use the procedure detailed in [34] to calculate uncertainties and correlations in the inverted efficiency matrix.

In Section 7 we present the results of fitting the $\Delta\Gamma_i$ to obtain total branching fractions and form factor parameters. First, however, we address the systematic uncertainties in the $\Delta\Gamma_i$.

SYSTEMATIC UNCERTAINTIES

In order to measure form factor shapes, it is necessary to understand systematic uncertainties on the $\Delta\Gamma_i$ and how these uncertainties are correlated across q^2 bins. For each source of systematic uncertainty, we construct a covariance matrix that provides both pieces of information, and sum these matrices into a combined systematic uncertainty covariance matrix. A summary of the systematic uncertainties is shown in table 6.1. Below we describe how each of the covariance matrices are constructed.

6.1 Tracking Efficiencies

Tracking efficiencies in data and Monte Carlo have been measured using 818 pb^{-1} of CLEO-c data [35]. No evidence of disagreement between data and Monte Carlo was found, so we do not weight our efficiency matrices for tracking efficiency bias.

Tracking efficiency systematics have been estimated in two ways. First, kaon and pion efficiencies in several momentum bins have been measured directly with a standard recoil technique: fully hadronic events containing a particle of type X, where $X = \pi^-$, K^-, are selected by reconstructing all particles in the event except for X. Missing mass squared distributions are formed and peak at M_X^2 for correctly reconstructed events. The fraction of events with the appropriate M_X^2 in which X was successfully reconstructed are tallied after correcting for backgrounds. By doing this in bins of missing momentum for both data and MC, we compare the data and MC efficiencies as a function of particle momentum.

An alternate method builds on the first, taking advantage of evidence that nearly all tracking inefficiencies are the result of particle decay within the drift chambers. Accounting for pion and kaon decay and interaction rates, the pion and kaon efficiency

Table 6.1: Summary of partial rate ($\Delta\Gamma_i$) uncertainties (%). The sign gives the direction of change relative to the change in the first q^2 bin.

	$\sigma(\Delta\Gamma_1)$	$\sigma(\Delta\Gamma_2)$	$\sigma(\Delta\Gamma_3)$	$\sigma(\Delta\Gamma_4)$	$\sigma(\Delta\Gamma_5)$	$\sigma(\Delta\Gamma_6)$	$\sigma(\Delta\Gamma_7)$	$\sigma(\Delta\Gamma_8)$	$\sigma(\Delta\Gamma_9)$
$D^0 \to \pi^- e^+ \nu_e$									
Tag Line Shape	0.40	0.40	0.40	0.40	0.40	0.40	0.40		
Tag Fakes	0.40	0.40	0.40	0.40	0.40	0.40	0.40		
Tracking Efficiency	0.48	0.48	0.48	0.48	0.48	0.49	0.51		
$\pi^\pm$ ID	0.46	0.40	0.44	0.37	0.27	0.22	0.78		
$e^\pm$ ID	0.37	0.38	0.38	0.39	0.33	0.18	-0.14		
FSR	0.18	0.11	0.09	-0.02	-0.10	-0.20	-0.24		
Signal Shape	0.56	0.46	0.58	0.49	0.50	0.56	0.49		
Backgrounds	0.39	0.43	0.60	0.61	0.58	0.52	0.76		
MC Form Factor	0.06	-0.05	-0.05	-0.05	-0.07	-0.11	-0.04		
q^2 Smearing	0.84	-0.11	-0.26	-0.16	0.30	-0.60	-0.28		
All	1.19	1.13	1.25	1.20	1.14	1.12	1.45		
Statistical	6.84	7.29	7.90	8.06	8.87	8.42	8.63		
$D^0 \to K^- e^+ \nu_e$									
Tag Line Shape	0.40	0.40	0.40	0.40	0.40	0.40	0.40	0.40	0.00
Tag Fakes	0.40	0.40	0.40	0.40	0.40	0.40	0.40	0.40	0.40
Tracking Efficiency	0.69	0.72	0.75	0.79	0.84	0.92	1.04	1.26	1.22
$K^\pm$ ID	1.02	0.97	0.92	0.89	1.02	0.71	0.32	-0.26	0.50
$e^\pm$ ID	0.41	0.42	0.43	0.45	0.47	0.48	0.44	0.33	0.21
FSR	0.12	0.08	0.07	0.01	-0.10	-0.15	-0.23	-0.28	-0.32
Signal Shape	0.16	0.12	0.12	0.14	0.12	0.11	0.09	0.14	0.21
Backgrounds	0.14	0.04	0.12	0.09	0.08	0.08	0.04	0.10	0.33
MC Form Factor	0.02	-0.02	-0.02	-0.01	-0.01	-0.01	0.00	0.02	-0.08
q^2 Smearing	0.62	-0.11	0.07	-0.12	-0.06	-0.51	0.08	-0.62	-2.05
All	1.44	1.41	1.39	1.40	1.53	1.39	1.33	1.48	1.48
Statistical	2.03	2.19	2.31	2.47	2.73	3.14	3.63	4.90	8.43
$D^+ \to \pi^0 e^+ \nu_e$									
Tag Line Shape	0.40	0.40	0.40	0.40	0.40	0.40	0.40		
Tag Fakes	0.70	0.70	0.70	0.70	0.70	0.70	0.70		
Tracking Efficiency	0.25	0.25	0.25	0.24	0.24	0.24	0.23		
π^0 ID	1.06	0.98	1.04	1.22	1.83	2.14	1.96		
$e^\pm$ ID	0.32	0.32	0.34	0.32	0.27	0.13	-0.22		
FSR	0.14	0.20	0.08	-0.05	-0.14	-0.22	-0.21		
Signal Shape	1.72	0.93	1.91	-1.24	3.51	2.43	3.26		
Backgrounds	0.92	0.82	-1.01	0.72	0.74	1.38	-6.04		
MC Form Factor	0.15	-0.03	-0.07	-0.06	-0.10	-0.15	0.57		
q^2 Smearing	1.69	0.28	-1.74	1.45	-0.17	-1.22	-1.41		
All	2.38	1.80	2.57	2.05	4.12	3.60	-6.98		
Statistical	9.25	10.23	11.24	11.28	13.44	12.38	17.98		
$D^+ \to \bar{K}^0 e^+ \nu_e$									
Tag Line Shape	0.40	0.40	0.40	0.40	0.40	0.40	0.40	0.40	0.00
Tag Fakes	0.70	0.70	0.70	0.70	0.70	0.70	0.70	0.70	0.70
Tracking Efficiency	0.76	0.77	0.78	0.79	0.81	0.83	0.87	0.91	0.96
K^0 ID	2.00	1.96	1.90	1.83	1.71	1.51	1.25	1.36	1.89
$e^\pm$ ID	0.42	0.43	0.43	0.45	0.48	0.48	0.44	0.33	0.20
FSR	0.17	0.13	0.08	0.01	-0.11	-0.16	-0.23	-0.24	-0.28
Signal Shape	0.20	0.22	0.17	0.20	0.23	0.26	0.38	0.26	0.47
Backgrounds	0.13	0.13	0.11	0.11	0.14	0.15	0.27	0.23	1.46
MC Form Factor	0.03	-0.02	-0.02	-0.02	-0.02	-0.01	0.01	0.02	0.08
q^2 Smearing	0.63	-0.24	-0.02	0.29	-1.06	0.75	-0.67	-0.78	-1.11
All	2.34	2.31	2.26	2.21	2.13	1.99	1.85	1.90	2.73
Statistical	2.63	2.90	3.04	3.23	3.82	3.98	5.04	6.88	10.63

results are averaged, resulting in a tracking efficiency systematic uncertainty which is in general higher for kaons than pions and higher for low momentum tracks than high momentum tracks. Since kaons and low momentum tracks are more likely to undergo particle death in the drift chamber, these results are physically motivated. For this reason, and because this technique results in a more conservative tracking systematic uncertainty for kaons, we have chosen to use this alternate estimation, which results in a systematic uncertainty that varies from $0.2\% - 0.3\%$ for pions and from $0.4\% - 1.4\%$ for kaons. We assume that uncertainties for electrons are the same as those for pions.

This technique is not valid for tracks with momentum less than 200 MeV. Tracks in this region are generally curlers, for which the assumptions relating particle death rates and tracking efficiencies are not applicable. For these low momentum tracks, we use the results of the first method, resulting in a 0.92% tracking systematic uncertainty for low momentum tracks. We take all uncertainties for momentum bins greater than 200 MeV to be fully correlated across q^2. Because the results for the low momentum bin were measured with a separate sample, and because these tracks are curlers, we treat the uncertainty of this bin as uncorrelated with higher momentum bins.

The results of the tracking efficiency study provide a covariance matrix binned in tracking momentum. To determine tracking uncertainties binned in q^2, we relate the q^2 binned tracking efficiencies, $\epsilon^{q^2}_{track}$, to momentum binned tracking efficiencies, ϵ^{p}_{track} via:

$$\epsilon^{\mathbf{q^2}}_{\mathbf{track}} = \mathbf{A}\epsilon^{\mathbf{p}}_{\mathbf{track}} \tag{6.1}$$

where $\mathbf{A}$ is a matrix that gives the fraction of tracks in a given momentum bin contained in semileptonic decays in a given q^2 bin; we obtain this matrix using signal Monte Carlo.

The fractional tracking efficiency covariance matrix binned in q^2, $\mathbf{M^{q^2}}$, is then given by:

$$\mathbf{M^{q^2}} = \mathbf{A}\mathbf{M^p}\mathbf{A^T} \tag{6.2}$$

where $\mathbf{M^p}$ is the covariance matrix of the tracking efficiency in momentum bins.

The systematic uncertainties on each of the $\Delta\Gamma_i$ due to tracking efficiency and the correlation matrices are shown in Tables 6.2-6.5.

Table 6.2: Tracking efficiency systematic uncertainties (in percent) and correlation matrix for for $D^0 \to \pi^- e^+ \nu_e$.

	q^2 (GeV^2)						
	$[0.0, 0.3)$	$[0.3, 0.6)$	$[0.6, 0.9)$	$[0.9, 1.2)$	$[1.2, 1.5)$	$[1.5, 2.0)$	$[2.0, \infty)$
$\sigma_{\Delta\Gamma}$ (%)	0.48	0.48	0.48	0.48	0.48	0.49	0.51
q^2 (GeV^2)							
$[0.0, 0.3)$	1	1	1	1	1	1	0.9
$[0.3, 0.6)$		1	1	1	1	1	0.9
$[0.6, 0.9)$			1	1	1	1	0.9
$[0.9, 1.2)$				1	1	1	0.9
$[1.2, 1.5)$					1	1	0.9
$[1.5, 2.0)$						1	0.9
$[2.0, \infty)$							1

Table 6.3: Tracking efficiency systematic uncertainties (in percent) and correlation matrix for for $D^0 \to K^- e^+ \nu_e$.

	q^2 (GeV^2)								
	$[0.0, 0.2)$	$[0.2, 0.4)$	$[0.4, 0.6)$	$[0.6, 0.8)$	$[0.8, 1.0)$	$[1.0, 1.2)$	$[1.2, 1.4)$	$[1.4, 1.6)$	$[1.6, \infty)$
$\sigma_{\Delta\Gamma}$ (%)	0.69	0.72	0.75	0.79	0.84	0.92	1	1.3	1.2
q^2 (GeV^2)									
$[0.0, 0.2)$	1	1	1	1	1	1	1	1	0.96
$[0.2, 0.4)$		1	1	1	1	1	1	1	0.96
$[0.4, 0.6)$			1	1	1	1	1	1	0.96
$[0.6, 0.8)$				1	1	1	1	1	0.96
$[0.8, 1.0)$					1	1	1	1	0.96
$[1.0, 1.2)$						1	1	1	0.96
$[1.2, 1.4)$							1	1	0.96
$[1.4, 1.6)$								1	0.96
$[1.6, \infty)$									1

6.2 Charged Hadron ID Efficiencies

Charged hadron identification efficiencies have been measured in data and Monte Carlo using 281 pb^{-1} of CLEO-c data [36]. This study measured efficiencies in nine momen-

Table 6.4: Tracking efficiency systematic uncertainties (in percent) and correlation matrix for for $D^+ \to \pi^0 e^+ \nu_e$.

	q^2 (GeV^2)						
	[0.0, 0.3)	[0.3, 0.6)	[0.6, 0.9)	[0.9, 1.2)	[1.2, 1.5)	[1.5, 2.0)	[2.0, ∞)
$\sigma_{\Delta\Gamma}$ (%)	0.25	0.25	0.25	0.24	0.24	0.24	0.23
q^2 (GeV^2)							
[0.0, 0.3)	1	1	1	1	1	1	1
[0.3, 0.6)		1	1	1	1	1	1
[0.6, 0.9)			1	1	1	1	1
[0.9, 1.2)				1	1	1	1
[1.2, 1.5)					1	1	1
[1.5, 2.0)						1	1
[2.0, ∞)							1

Table 6.5: Tracking efficiency systematic uncertainties (in percent) and correlation matrix for for $D^+ \to \bar{K}^0 e^+ \nu_e$.

	q^2 (GeV^2)							
	[0.0, 0.2)	[0.2, 0.4)	[0.4, 0.6)	[0.6, 0.8)	[0.8, 1.0)	[1.0, 1.2)	[1.2, 1.4)	[1.4, 1.6)	[1.6, ∞)
$\sigma_{\Delta\Gamma}$ (%)	0.76	0.77	0.78	0.79	0.81	0.83	0.87	0.91	0.97
q^2 (GeV^2)									
[0.0, 0.2)	1	1	1	0.99	0.97	0.95	0.92	0.89	0.84
[0.2, 0.4)		1	1	0.99	0.98	0.96	0.94	0.91	0.86
[0.4, 0.6)			1	1	0.99	0.98	0.96	0.93	0.89
[0.6, 0.8)				1	1	0.99	0.97	0.95	0.91
[0.8, 1.0)					1	1	0.99	0.97	0.94
[1.0, 1.2)						1	1	0.98	0.96
[1.2, 1.4)							1	1	0.98
[1.4, 1.6)								1	1
[1.6, ∞)									1

tum bins for kaons and eleven momentum bins for pions. A bias between data and Monte Carlo efficiencies has been observed. Weighting the biases over the semileptonic momentum spectrum, the $D^0 \to \pi^- e^+ \nu_e$ efficiency is (0.34 ± 0.11)% higher in Monte Carlo than in data, while the $D^0 \to K^- e^+ \nu_e$ efficiency is (0.83 ± 0.15)% higher in Monte Carlo than in data. We have weighted the signal efficiency matrices to account for these biases.

A covariance matrix for $\pi^\pm$ and $K^\pm$ identification efficiency uncertainties can be estimated in a manner similar to that described above for tracking efficiencies. Using the $281~\mathrm{pb}^{-1}$ study, we construct a covariance matrix for the efficiencies binned in hadron momentum. We do this by assuming the statistical uncertainties are uncorrelated across momentum bins. Because the study has not yet been updated for the full data sample, we conservatively take 100% of the bias for a given momentum bin as the systematic uncertainty for that bin, and assume the systematic uncertainties are fully correlated across momentum bins. The final systematic uncertainties are obtained by transforming the covariance matrix binned in momentum to one binned in q^2. The fractional systematic uncertainties on each of the $\Delta\Gamma_i$ due to charged hadron identification efficiency are shown in Tables 6.6-6.7.

Table 6.6: Charged hadron systematic uncertainties and correlation matrix for $D^0 \to \pi^- e^+ \nu_e$.

	q^2 (GeV^2)						
	$[0.0, 0.3)$	$[0.3, 0.6)$	$[0.6, 0.9)$	$[0.9, 1.2)$	$[1.2, 1.5)$	$[1.5, 2.0)$	$[2.0, \infty)$
$\sigma_{\Delta\Gamma}$ (%)	0.46	0.4	0.44	0.37	0.27	0.22	0.79
q^2 (GeV^2)							
$[0.0, 0.3)$	1	0.92	0.68	0.64	0.64	0.64	0.65
$[0.3, 0.6)$		1	0.91	0.87	0.86	0.85	0.87
$[0.6, 0.9)$			1	0.99	0.97	0.96	0.97
$[0.9, 1.2)$				1	0.99	0.97	0.98
$[1.2, 1.5)$					1	0.98	0.99
$[1.5, 2.0)$						1	0.98
$[2.0, \infty)$							1

6.3 π^0 Finding Efficiencies

Efficiencies for reconstructing π^0's in data and Monte Carlo have been measured using the full CLEO-c data sample [33] in five momentum bins, and the π^0 finding efficiencies

Table 6.7: Charged hadron systematic uncertainties and correlation matrix for $D^0 \to \pi^- e^+ \nu_e$.

				q^2 (GeV^2)					
	[0.0, 0.2)	[0.2, 0.4)	[0.4, 0.6)	[0.6, 0.8)	[0.8, 1.0)	[1.0, 1.2)	[1.2, 1.4)	[1.4, 1.6)	[1.6, ∞)
$\sigma_{\Delta\Gamma}$ (%)	1	0.97	0.91	0.88	1	0.71	0.32	0.26	0.51
q^2 (GeV^2)									
[0.0, 0.2)	1	0.98	0.96	0.94	0.93	0.89	0.61	-0.13	0.6
[0.2, 0.4)		1	0.99	0.97	0.96	0.92	0.63	-0.14	0.61
[0.4, 0.6)			1	0.99	0.98	0.93	0.64	-0.14	0.62
[0.6, 0.8)				1	0.99	0.95	0.65	-0.14	0.62
[0.8, 1.0)					1	0.98	0.69	-0.12	0.62
[1.0, 1.2)						1	0.8	-0.049	0.6
[1.2, 1.4)							1	0.42	0.49
[1.4, 1.6)								1	0.43
[1.6, ∞)									1

have been found to be about 6% smaller in data than in Monte Carlo. We correct the $D^+ \to \pi^0 e^+ \nu_e$ efficiency matrices for the momentum-dependent biases.

The uncertainties on the bias come from three primary sources. Each bin has a statistical uncertainty which we assume is uncorrelated across momentum bins. There is also a systematic uncertainty due to background subtractions which we take to be fully correlated across momentum bins. Finally, there is a systematic uncertainty due to the presence of fake π^0's. Since this affects primarily the first two momentum bins, we assume this uncertainty is correlated between the first two momentum bins only. The π^0 finding covariance matrix binned in q^2 is calculated as described above for tracking efficiencies, with the resulting uncertainties and correlations each the $\Delta\Gamma_i$ shown in Table 6.8.

6.4 K_S^0 **Finding Efficiencies**

K_S^0 finding efficiencies have been measured in 818 pb^{-1} of CLEO-c data [37]. As this efficiency has been found to be $(0.14 \pm 0.76)\%$ higher in data than in Monte Carlo, no efficiency correction is necessary. The K_S^0 finding efficiencies are provided in four K_S^0

Table 6.8: π^0 finding systematic uncertainties and correlations matrix for $D^+ \rightarrow \pi^0 e^+ \nu_e$

	q^2 (GeV^2)						
	$[0.0, 0.3)$	$[0.3, 0.6)$	$[0.6, 0.9)$	$[0.9, 1.2)$	$[1.2, 1.5)$	$[1.5, 2.0)$	$[2.0, \infty)$
$\sigma_{\Delta\Gamma}$ (%)	1.1	0.98	1	1.2	1.8	2.1	2
q^2 (GeV^2)							
$[0.0, 0.3)$	1	0.95	0.76	0.74	0.7	0.69	0.65
$[0.3, 0.6)$		1	0.92	0.89	0.76	0.71	0.68
$[0.6, 0.9)$			1	0.95	0.73	0.64	0.62
$[0.9, 1.2)$				1	0.89	0.83	0.66
$[1.2, 1.5)$					1	0.99	0.66
$[1.5, 2.0)$						1	0.71
$[2.0, \infty)$							1

momentum bins. We take the bias measured for a particular momentum bin, added in quadrature with the uncertainty on the bias as the total systematic uncertainty for that momentum bin (resulting in uncertainties of 1.2-2.1% depending on momentum). We assume the uncertainties are fully correlated across momentum bins. The K^0_S finding covariance matrix binned in momentum is transformed into a q^2 matrix as described above for tracking uncertainties, and the systematic uncertainties in each of the $\Delta\Gamma_i$ and their correlations are shown in Table 6.9.

Table 6.9: K^0_S finding systematic uncertianties and correlation matrix for $D^+ \rightarrow \bar{K}^0 e^+ \nu_e$

	q^2 (GeV^2)								
	$[0.0, 0.2)$	$[0.2, 0.4)$	$[0.4, 0.6)$	$[0.6, 0.8)$	$[0.8, 1.0)$	$[1.0, 1.2)$	$[1.2, 1.4)$	$[1.4, 1.6)$	$[1.6, \infty)$
$\sigma_{\Delta\Gamma}$ (%)	2	2	1.9	1.8	1.7	1.5	1.2	1.4	1.9
q^2 (GeV^2)									
$[0.0, 0.2)$	1	1	1	1	1	1	1	1	1
$[0.2, 0.4)$		1	1	1	1	1	1	1	1
$[0.4, 0.6)$			1	1	1	1	1	1	1
$[0.6, 0.8)$				1	1	1	1	1	1
$[0.8, 1.0)$					1	1	1	1	1
$[1.0, 1.2)$						1	1	1	1
$[1.2, 1.4)$							1	1	1
$[1.4, 1.6)$								1	1
$[1.6, \infty)$									1

6.5 Electron Identification

Electron identification efficiencies as a function of electron momentum are measured in Monte Carlo and in data using radiative bhabha (*eeγ*) and two-photon (*eeee*) events [38]. Since the electrons in these events are rather isolated, they are embedded into hadronic events to determine the decrease in efficiency due to event environment. Biases of around 1.5% are observed, originating primarily in the isolated electron efficiency, and the signal efficiency matrices and *U* distributions in MC are corrected for these biases.

Uncertainty in the electron ID efficiency arises from (1) systematic uncertainty in identifying isolated electrons, (2) systematic uncertainty in the event environment effects and (3) statistical uncertainty in the corrections. We estimate the effect of (1) by altering our nominal corrections by the uncertainties on the single electron efficiency bias. We take the uncertainty on the event environment bias to be half of itself, altering the corrections by half of event environment biases and recalculating the partial rates. The shifts in yields with each of these variations in corrections is shown in Table 6.10.

Covariance matrices due to a given effect are calculated from the shifts in $\Delta\Gamma_i$ via:

$$\mathbf{M}_{ij} = \Delta\left(\Delta\Gamma_i\right)\Delta\left(\Delta\Gamma_j\right) \tag{6.3}$$

To obtain the total electron ID systematic uncertainties, also shown in Table 6.10, we add the covariance matrices for single track efficiency bias and event environment effects together with a diagonal matrix accounting for the 0.1% due to statistical uncertainties on the bias.

Table 6.10: EID Systematics: Changes in $\Delta\Gamma_i$ in percent when electron identification weights are varied, and the combined systematic uncertainties on partial rates due to Electron ID

	$\Delta\Gamma_1$	$\Delta\Gamma_2$	$\Delta\Gamma_3$	$\Delta\Gamma_4$	$\Delta\Gamma_5$	$\Delta\Gamma_6$	$\Delta\Gamma_7$	$\Delta\Gamma_8$	$\Delta\Gamma_9$
$D^0 \to \pi^- e^+ \nu_e$									
Single e	0.28	0.30	0.31	0.33	0.29	0.12	-0.09		
Event Env.	0.22	0.21	0.20	0.17	0.14	0.08	0.05		
Bias Stat. Unc.	0.10	0.10	0.10	0.10	0.10	0.10	0.10		
Total EID Sys. Unc.	0.37	0.38	0.38	0.39	0.33	0.23	0.14		
$D^0 \to K^- e^+ \nu_e$									
Single e	0.32	0.33	0.35	0.37	0.42	0.43	0.40	0.30	0.17
Event Env.	0.24	0.23	0.23	0.22	0.21	0.19	0.15	0.11	0.08
Bias Stat. Unc.	0.10	0.10	0.10	0.10	0.10	0.10	0.10	0.10	0.10
Total EID Sys. Unc.	0.41	0.42	0.43	0.45	0.47	0.43	0.44	0.33	0.21
$D^+ \to \pi^0 e^+ \nu_e$									
Single e	0.25	0.25	0.28	0.28	0.24	0.07	-0.19		
Event Env.	0.17	0.17	0.16	0.13	0.10	0.05	0.01		
Bias Stat. Unc.	0.10	0.10	0.10	0.10	0.10	0.10	0.10		
Total EID Sys. Unc.	0.32	0.32	0.34	0.32	0.27	0.17	0.22		
$D^+ \to \bar{K}^0 e^+ \nu_e$									
Single e	0.33	0.34	0.35	0.38	0.42	0.43	0.40	0.30	0.16
Event Env.	0.24	0.24	0.23	0.22	0.21	0.19	0.15	0.11	0.07
Bias Stat. Unc.	0.10	0.10	0.10	0.10	0.10	0.10	0.10	0.10	0.10
Total EID Sys. Unc.	0.42	0.43	0.43	0.45	0.48	0.43	0.44	0.33	0.20

6.6 Number of D Tags

As the number of D tags is obtained from fits to M_{BC} distributions, there is a systematic uncertainty arising from our tag fitting procedure. To estimate this uncertainty we have followed the procedure in [39] and made several variations to the fitting procedure by:

- Taking yields from signal shape integration rather than background subtraction

- Using an older parametrization of the $\psi(3770)$ line shape

- Varying the mass of the $\psi(3770)$ by ± 0.5 MeV/c^2

- Varying the width of the $\psi(3770)$ by ± 2.5 MeV/c^2

- Varying the Blatt-Weisskopf radius [29, 39] by ± 4 GeV/c^2

The change in yield with each of these variations is shown in Table 6.11.

For each variation described above, we compute the change in summed D^0 tags and the change in summed D^+ tags. We then combine these in quadrature, keeping positive and negative variations separate. The results are shown in the last two columns of Table 6.11. The systematic uncertainty in the number of D^0 (D^+) tags is estimated to be 0.42% (0.40%). We take 0.4% as the systematic uncertainty on the number of tags for both D^0 and D^+.

Table 6.11: Changes in tag yields in percent when variations are made to the tag fitting procedure.

Tag mode	Integrate	MARKII	$M(3770)$	$M(3770)$	$\Gamma(3770)$	$\Gamma(3770)$	r	r	Total	Total
			+	−	+	−	+	−	−	+
$D^0 \to K^-\pi^+$	0.31	0.03	-0.02	0.03	0.06	-0.11	0.02	-0.03		
$D^0 \to K^-\pi^+\pi^0$	0.27	0.05	-0.09	0.13	0.25	0.24	0.04	-0.07		
$D^0 \to K^-\pi^+\pi^+\pi^-$	0.42	0.04	-0.12	0.12	0.32	-0.25	0.03	-0.06 d		
$D^+ \to K^-\pi^+\pi^+$	0.22	-0.01	-0.07	0.08	0.14	-0.16	0.04	-0.09		
$D^+ \to K^-\pi^+\pi^+\pi^0$	0.50	0.06	-0.48	-0.22	-0.13	-0.59	0.14	-0.10		
$D^+ \to K^0_S\pi^+$	0.31	0.00	-0.10	0.10	0.14	-0.26	0.01	-0.17		
$D^+ \to K^0_S\pi^+\pi^0$	0.49	0.00	-0.10	0.15	0.23	-0.21	0.08	-0.09		
$D^+ \to K^0_S\pi^+\pi^+\pi^-$	0.68	-0.04	-0.16	0.16	0.26	0.10	0.02	-0.12		
$D^+ \to K^-K^+\pi^+$	0.51	-0.01	-0.14	0.14	0.22	-0.25	0.05	-0.10		
D^0 total	0.33	0.04	-0.09	0.10	0.23	-0.01	0.03	-0.06	-0.10	0.42
D^+ total	0.37	0.00	-0.15	0.06	0.13	-0.22	0.06	-0.10	-0.28	0.40

The systematic uncertainty due to the number of D tags is independent of the kinematics of the semileptonic decay recoiling against the tag. These uncertainties are thus fully correlated across q^2.

6.7 Tag Fakes

Choosing one tag per mode per flavor introduces another systematic uncertainty related to the number of tags. This choice results in a reduction in tag efficiency, since occasionally a false tag will be chosen over a correct tag. This occurs most often due to fake π^0's, which are usually formed from a true π^0 shower combining with an hadronic shower.

This causes the rate of fake π^0's on the tag side to depend heavily on the decay opposite the tag. Relatively clean semileptonic decays are less likely to cause a fake π^0 than a decay with several hadrons. This effect, combined with an incorrect π^0 fake rate in the Monte Carlo could result in an overall mismeasurement of our rates. There is evidence [33] that the π^0 fake rate is about 15% higher in data than in Monte Carlo. Monte Carlo studies indicate that the best tag selection results in an efficiency loss of around 6.5% in modes with π^0's. We therefore apply a $6.5\% \times 15\% = 1\%$ overall systematic uncertainty to tag modes with π^0's only. This results in a 0.4% systematic uncertainty for D^0 modes and a 0.7% systematic uncertainty for $D^\pm$ modes, fully correlated across q^2.

6.8 FSR
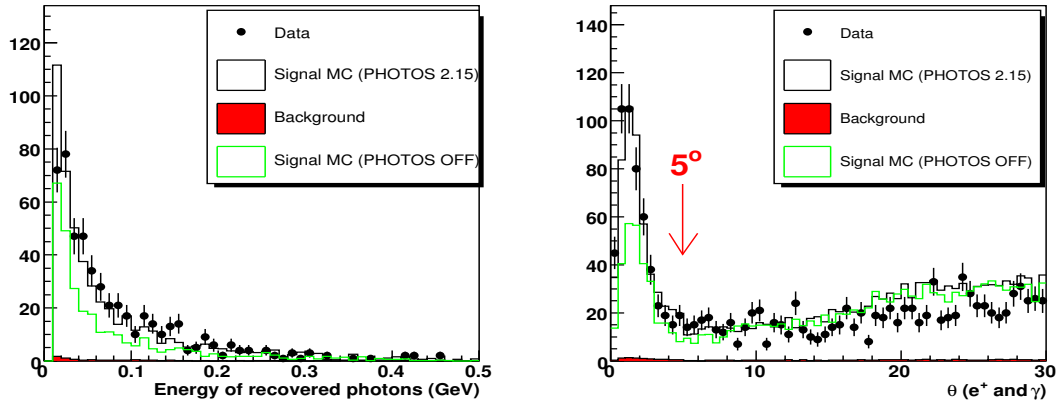
Figure 6.1: Recovered FSR energy and angular distributions in data and MC. Plots show reconstructed $D^0 \rightarrow K^- e^+ \nu_e$ events with all q^2 and all tag modes. $E_{FSR} > 10$ MeV has been applied to both plots. The energy distributions are for photons within 5° of the electron momentum.

Our estimation of the systematic uncertainties associated with FSR simulation is based on discrepancies between data and Monte Carlo in the energy distribution of the photons surrounding electrons, as shown in Figure 6.1. We reweight the Monte Carlo

Table 6.12: FSR Systematics: Changes in $\Delta\Gamma_i$ in percent when FSR energy spectra in MC are reweighted

	$\sigma_{\Delta\Gamma_1}$	$\sigma_{\Delta\Gamma_2}$	$\sigma_{\Delta\Gamma_3}$	$\sigma_{\Delta\Gamma_4}$	$\sigma_{\Delta\Gamma_5}$	$\sigma_{\Delta\Gamma_6}$	$\sigma_{\Delta\Gamma_7}$	$\sigma_{\Delta\Gamma_8}$	$\sigma_{\Delta\Gamma_9}$
$D^0 \to \pi^- e^+ \nu_e$	0.02	0.11	0.09	-0.02	-0.10	-0.20	-0.24		
$D^0 \to K^- e^+ \nu_e$	0.01	0.08	0.07	0.01	-0.10	-0.14	-0.23	-0.28	-0.32
$D^+ \to \pi^0 e^+ \nu_e$	0.01	0.20	0.08	-0.05	-0.14	-0.22	-0.21		
$D^+ \to \bar{K}^0 e^+ \nu_e$	0.02	0.13	0.08	0.01	-0.11	-0.16	-0.23	-0.24	-0.28

events used in the efficiency matrix determination so that the distributions shown in Figure 6.1 match data, and remeasure the efficiency matrices. The very small changes in the partial rates when the unweighted efficiency matrix is replaced with the weighted efficiency matrix are given in Table 6.12. These are used to calculate covariance matrices for the FSR systematic uncertainty.

6.9 U Fit: Signal Shape

The shape used to model signal events in the U fits is taken from signal Monte Carlo and convolved with a double Gaussian. For each mode, the widths of the two Gaussians and their relative normalization are fixed to values that minimize the fit likelihood summed over all tag modes and q^2 bins. To estimate systematic uncertainties due to signal shape, we vary the fixed parameters by values that increase the log-likelihood by unity. These values are shown in Table 6.13, and the resulting changes in the $\Delta\Gamma$ are shown in Table 6.14. We use Equation 6.3 to transform these shifts into systematic covariance matrices for signal shape, averaging the effects of positive and negative variations.

We have studied whether the Monte Carlo signal shapes appear shifted with respect to the data. The likelihoods summed over all tag modes and q^2 bins for $D^0 \to \pi^- e^+ \nu_e$, $D^0 \to K^- e^+ \nu_e$ and $D^+ \to \bar{K}^0 e^+ \nu_e$ prefer unshifted signal shapes. However, $D^+ \to \pi^0 e^+ \nu_e$ prefers a shift of about -1.5 MeV. Lacking a physical motivation for this shift, we have

chosen not to shift any of the signal Monte Carlo distributions, but to assign a systematic uncertainty to the $D^+ \to \pi^0 e^+ \nu_e$ rates equal to the change in rates when a 1.5 MeV shift is applied. These changes in rates are shown in the row labeled "shift+" in Table 6.14.

Table 6.13: The double Gaussian widths (σ_1,σ_2) and relative normalization (N_{12}) and the positive (+) and negative (−) variations used to obtained signal shape systematic uncertainties

mode	σ_1 (MeV)	σ_1- (MeV)	σ_1+ (MeV)	σ_2 (MeV)	σ_2- (MeV)	σ_2+ (MeV)	N_{12} (%) (%)	$N_{12}-$(%) (%)	$N_{12}+$ (%) (%)
$D^0 \to \pi^- e^+ \nu_e$	6	2	7	30	15	55	5	1	8
$D^0 \to K^- e^+ \nu_e$	5	4	7	30	25	40	4	3	6
$D^+ \to \pi^0 e^+ \nu_e$	13	11	15	35	5	100	7	0	17
$D^+ \to \bar{K}^0 e^+ \nu_e$	7	6	8	35	30	55	3	1	4

6.10 U Fit: Backgrounds

The treatment of backgrounds in the signal yield fitter leads to a number of sources of systematic uncertainty:

- Those associated with the fixed non-$D\bar{D}$ background to all modes and $D^0 \to \rho^- e^+ \nu_e$ background to $D^0 \to \pi^- e^+ \nu_e$ are estimated by varying these normalizations within their uncertainties ($\pm 20\%$ and $\pm 12.5\%$ respectively) and remeasuring the $\Delta\Gamma_i$.

- The $D^0 \to K^- e^+ \nu_e$ background to $D^0 \to \pi^- e^+ \nu_e$ and $D^+ \to \bar{K}^0 e^+ \nu_e$ background to $D^+ \to \pi^0 e^+ \nu_e$ are fixed to values that minimize the combined likelihood over all q^2 and all tag modes. To estimate the systematic uncertainty associated with this choice, we vary the normalizations by amounts that shift the log-likelihood by unity and remeasure the partial rates.

- One background shape combines many different background modes. The relative normalizations of these different backgrounds may be different in the data and in

70

Table 6.14: Signal Shape Systematics: Changes in $\Delta\Gamma_i$ and χ^2 in percent when variations to signal shape parameters. The combined systematic uncertainties on the partial rates due to signal shape are also shown.

	$\Delta\Gamma_1$	$\Delta\Gamma_2$	$\Delta\Gamma_3$	$\Delta\Gamma_4$	$\Delta\Gamma_5$	$\Delta\Gamma_6$	$\Delta\Gamma_7$	$\Delta\Gamma_8$	$\Delta\Gamma_9$	$\Delta\chi^2$
$\mathbf{D^0 \to \pi^- e^+ \nu_e}$										
Smear+	0.11	0.09	0.11	0.11	0.06	0.09	0.10			0.98
Smear-	-0.39	-0.30	-0.39	-0.37	-0.34	-0.35	-0.30			1.58
Smear2+	0.40	0.38	0.44	0.30	0.34	0.50	0.45			1.07
Smear2-	-0.33	-0.25	-0.34	-0.30	-0.32	-0.31	-0.24			1.35
Norm+	0.23	0.18	0.23	0.21	0.21	0.22	0.19			1.07
Norm-	-0.37	-0.28	-0.37	-0.35	-0.34	-0.34	-0.28			1.44
Total Sys.	0.56	0.46	0.58	0.49	0.50	0.56	0.49			
$\mathbf{D^0 \to K^- e^+ \nu_e}$										
Smear+	0.07	0.05	0.06	0.07	0.07	0.07	0.05	0.09	0.15	18.48
Smear-	-0.08	-0.06	-0.06	-0.07	-0.06	-0.06	-0.04	-0.08	-0.12	3.01
Smear2+	0.15	0.10	0.11	0.12	0.10	0.09	0.08	0.11	0.14	4.09
Smear2-	-0.07	-0.05	-0.05	-0.06	-0.05	-0.04	-0.03	-0.05	-0.08	1.30
Norm+	0.09	0.07	0.07	0.08	0.07	0.06	0.05	0.09	0.14	2.28
Norm-	-0.05	-0.04	-0.04	-0.04	-0.04	-0.03	-0.03	-0.05	-0.07	1.23
Total Sys.	0.16	0.12	0.12	0.14	0.12	0.11	0.09	0.14	0.21	
$\mathbf{D^+ \to \pi^0 e^+ \nu_e}$										
Smear+	0.02	0.02	-0.01	0.08	0.08	0.12	0.28			1.29
Smear-	-0.44	-0.33	-0.60	-0.63	-1.21	-1.75	-2.46			2.05
Smear2+	1.04	1.16	1.19	0.98	1.59	1.83	1.37			0.53
Smear2-	-0.43	-0.31	-0.55	-0.54	-1.07	-1.49	-1.99			0.96
Norm+	0.35	0.18	0.42	0.42	0.93	1.27	1.80			1.34
Norm-	-0.32	-0.20	-0.44	-0.39	-0.84	-1.16	-1.59			0.61
Shift+	-1.45	-0.22	-1.55	0.75	-2.99	0.31	1.32			-42.69
Total Sys.	1.72	0.93	1.91	1.24	3.51	2.43	3.26			
$\mathbf{D^+ \to \bar{K}^0 e^+ \nu_e}$										
Smear+	0.01	0.03	0.02	0.04	0.05	0.04	0.02	0.06	0.19	18.98
Smear-	-0.11	-0.14	-0.10	-0.14	-0.16	-0.18	-0.24	-0.17	-0.40	7.25
Smear2+	0.20	0.22	0.19	0.18	0.22	0.25	0.36	0.26	0.32	0.77
Smear2-	-0.05	-0.06	-0.05	-0.05	-0.06	-0.07	-0.11	-0.07	-0.10	0.88
Norm+	0.06	0.07	0.05	0.06	0.07	0.08	0.12	0.07	0.16	2.24
Norm-	-0.13	-0.14	-0.10	-0.14	-0.15	-0.18	-0.27	-0.16	-0.33	1.91
Total Sys.	0.20	0.22	0.17	0.20	0.23	0.26	0.38	0.26	0.47	

the Monte Carlo, resulting in an incorrect background shape. We vary the relative weights of each of the largest constituents of these shapes within the uncertainties on their branching fractions. One component is fake tags; we vary the normalization of this background by ±25%, based on background levels in the tag yield fits in data and Monte Carlo. Another subset is composed of a variety of very small backgrounds. We vary the normalization of this background by ±50%.

- Inaccurate electron fake rates in the Monte Carlo may also result in incorrect background shapes. A study of Electron ID fake rates, documented in [38], found that kaon and pion faking electron rates may be several factors higher in data than in Monte Carlo. To estimate systematic uncertainties due to electron fakes, we increase the relative normalization of the electron fake backgrounds by the values observed in the EID fake rates study, and remeasure our results.

- Poorly simulated π^0 fake rates can cause the background shapes used in $D^+ \rightarrow \pi^0 e^+ \nu_e$ to be incorrect. These rates have been shown to be approximately 15% larger in data than in Monte Carlo [33]. We measure the systematic uncertainty due to π^0 fakes by increasing the π^0 fake rate in the Monte Carlo by 15%.

- The $D^+ \rightarrow \pi^0 e^+ \nu_e$ mode is also affected by a small background from $D \rightarrow K^0 e \nu$ in which the K^0 materializes as a K_L^0, which then showers in the calorimeter. This background occurs primarily in the final two q^2 bins. K_L^0 showering rates have been studied [40]. For K_L^0's with momentum above 50 MeV, showering rates are well mirrored in the Monte Carlo, so we do not correct the normalization of this background. To account for uncertainties in K_L^0 showering rates, we vary the normalization of this background by 10%, which approximates the uncertainty in the K_L^0 showering study .

The results of all the background variations are shown in Table 6.15 for $D^0 \rightarrow \pi^- e^+ \nu_e$ and $D^0 \rightarrow K^- e^+ \nu_e$ and in Table 6.16 for $D^+ \rightarrow \pi^0 e^+ \nu_e$ and $D^+ \rightarrow \bar{K}^0 e^+ \nu_e$. We again use

Equation 6.3 to construct a covariance matrix for each of the above describe background effects, and add these to obtain a total background covariance matrix. Where positive and negative variations have been made, we average the resulting covariance matrices.

Table 6.15: Background Systematics: Changes in $\Delta\Gamma_i$ in percent with variation in the treatment of backgrounds varied normalizations and total systematic uncertainties due to backgrounds, for $D^0 \rightarrow \pi^- e^+ \nu_e$ and $D^0 \rightarrow K^- e^+ \nu_e$

	$\Delta\Gamma_1$	$\Delta\Gamma_2$	$\Delta\Gamma_3$	$\Delta\Gamma_4$	$\Delta\Gamma_5$	$\Delta\Gamma_6$	$\Delta\Gamma_7$	$\Delta\Gamma_8$	$\Delta\Gamma_9$	$\Delta\chi^2$
$D^0 \rightarrow \pi^- e^+ \nu_e$										
Non-DDbar +	-0.14	-0.05	0.00	0.01	-0.07	-0.11	-0.03			0.82
Non-DDbar -	0.15	0.05	-0.00	-0.01	0.07	0.12	0.03			-0.72
Rhoenu +	-0.11	-0.19	-0.21	-0.22	-0.18	-0.15	-0.19			0.13
Rhoenu -	0.12	0.20	0.20	0.23	0.20	0.18	0.21			0.66
Kenu +	-0.34	-0.33	-0.21	-0.27	-0.24	-0.11	-0.13			1.53
Kenu -	0.20	0.21	0.13	0.17	0.15	0.08	0.08			0.99
Other, Kpipi0 +	0.04	0.05	0.07	0.05	0.03	0.02	0.12			-0.38
Other, Kpipi0 -	-0.04	-0.05	-0.07	-0.05	-0.03	-0.02	-0.12			0.47
Other, Kpi +	-0.01	-0.00	0.00	0.00	0.00	0.00	0.00			0.09
Other, Kpi -	-0.01	-0.00	0.00	0.00	0.00	0.00	0.00			0.09
Other, K*enu +	0.01	0.01	0.02	0.03	0.02	0.05	0.07			0.99
Other, K*enu -	-0.01	-0.01	-0.02	-0.03	-0.02	-0.05	-0.07			-0.90
Other, Kmunu +	-0.00	0.00	0.00	0.00	0.02	0.02	-0.01			-0.36
Other, Kmunu -	0.00	-0.00	-0.00	-0.00	-0.02	-0.02	0.01			-0.36
Other, Fake Tags +	-0.16	-0.23	-0.47	-0.44	-0.39	-0.38	-0.56			0.23
Other, Fake Tags -	0.16	0.24	0.48	0.48	0.45	0.46	0.62			0.12
Other, Other +	0.10	-0.02	0.05	0.17	0.16	0.09	-0.28			0.78
Other, Other -	-0.12	0.03	-0.09	-0.19	-0.17	-0.09	0.37			0.59
EID fakes, $\pi \rightarrow e$	-0.04	-0.00	-0.02	0.01	0.08	-0.02	-0.12			0.07
EID fakes, $K \rightarrow e$	-0.02	0.10	0.22	0.16	0.20	0.17	0.19			0.00
Total Bkgd. Sys.	0.39	0.43	0.60	0.61	0.58	0.52	0.76			
$D^0 \rightarrow K^- e^+ \nu_e$										
non-DDbar +	-0.01	0.00	0.00	0.00	0.00	-0.00	-0.00	0.00	0.00	52.59
non-DDbar -	0.00	-0.00	-0.00	-0.00	-0.00	0.00	0.00	-0.00	0.00	52.59
Other, Kpipi0 +	0.01	0.00	-0.00	-0.00	0.00	0.00	0.00	-0.00	0.00	52.47
Other, Kpipi0 -	-0.01	-0.00	0.00	0.00	-0.00	-0.00	-0.00	0.00	0.00	52.69
Other, K*enu +	0.01	0.00	0.01	0.01	0.02	0.02	0.01	0.02	0.05	52.76
Other, K*enu -	-0.02	-0.00	-0.01	-0.01	-0.02	-0.02	-0.01	-0.03	0.00	52.38
Other, Fake Tags +	-0.02	-0.03	-0.03	-0.02	-0.03	-0.03	-0.03	-0.07	-0.04	52.61
Other, Fake Tags -	0.01	0.03	0.03	0.03	0.03	0.03	0.03	0.07	0.00	52.58
Other, Other +	-0.11	0.01	0.01	-0.00	-0.07	-0.07	-0.02	-0.00	-0.28	52.90
Other, Other -	0.12	-0.01	-0.01	0.01	0.08	0.08	0.02	0.01	0.32	53.05
EID Fakes, $\pi \rightarrow e$	-0.07	-0.03	-0.12	-0.09	-0.00	0.01	0.01	-0.08	0.00	50.64
EID Fakes, $K \rightarrow e$	-0.02	0.00	0.00	0.00	0.00	-0.00	0.00	0.01	0.00	52.75
Total Bkgd. Sys.	0.14	0.04	0.12	0.09	0.08	0.08	0.04	0.10	0.33	

Table 6.16: Background Systematics: Changes in $\Delta\Gamma_i$ in percent with variation in the treatment of backgrounds and total systematic uncertainty due to backgrounds, for $D^+ \to \pi^0 e^+ \nu_e$ and $D^+ \to \bar{K}^0 e^+ \nu_e$

	$\Delta\Gamma_1$	$\Delta\Gamma_2$	$\Delta\Gamma_3$	$\Delta\Gamma_4$	$\Delta\Gamma_5$	$\Delta\Gamma_6$	$\Delta\Gamma_7$	$\Delta\Gamma_8$	$\Delta\Gamma_9$	$\Delta\chi^2$
$D^+ \to \pi^0 e^+ \nu_e$										
non-DDbar +	0.04	0.09	0.01	0.06	0.04	0.02	0.03			1.06
non-DDbar -	0.04	0.05	0.02	0.11	0.05	0.08	0.08			-0.93
K0enu +	0.22	0.37	-0.40	-0.28	0.29	-0.50	-1.54			1.90
K0enu -	-0.11	-0.22	0.46	0.47	-0.20	0.52	1.66			1.26
Other, $\eta e\nu$ +	0.04	0.09	0.02	0.09	0.05	0.07	0.07			0.07
Other, $\eta e\nu$ -	0.05	0.05	0.05	0.08	0.05	0.03	0.04			0.00
Other, $\Omega e\nu$ +	0.05	-0.03	-0.05	0.07	-0.47	0.19	-0.10			-0.42
Other, $\Omega e\nu$ -	0.07	0.14	0.13	0.07	0.59	-0.10	0.21			0.49
Other, $K^* e\nu$ +	0.07	0.11	0.05	0.08	0.19	0.05	0.36			0.22
Other, $K^* e\nu$ -	0.01	0.03	0.02	0.09	-0.10	0.06	-0.27			-0.13
Other, Fake Tags +	-0.13	-0.13	0.05	0.13	-0.17	-0.04	-0.90			-0.85
Other, Fake Tags -	0.24	0.32	0.00	0.07	0.31	0.22	1.07			1.13
Other, Other +	-0.24	-0.10	-0.09	0.11	-0.29	0.17	0.54			-1.84
Other -	-0.24	-0.10	-0.09	0.11	-0.29	0.17	0.54			-1.84
EID Fakes, $\pi \to e$ +	0.00	0.00	0.00	0.00	0.00	0.00	0.00			0.00
EID Fakes, $K \to e$ -	0.00	0.00	0.00	0.00	0.00	0.00	0.00			0.00
KL +	-0.08	-0.02	-0.13	-0.08	-0.14	-0.14	-1.94			0.19
KL −	0.08	0.02	0.11	0.08	0.16	0.13	1.89			0.20
π^0 Fakes	0.84	0.70	-0.89	0.55	0.10	1.24	-5.37			1.25
Total Bkgd. Sys.	0.92	0.82	1.01	0.72	0.74	1.38	6.04			
$D^+ \to \bar{K}^0 e^+ \nu_e$										
non-DDbar +	0.06	0.06	0.05	0.04	0.05	0.04	0.05	0.04	0.03	0.42
non-DDbar -	0.05	0.05	0.05	0.04	0.06	0.04	0.04	0.07	0.02	-0.38
Other, $K^0 \pi\pi^0$ +	0.06	0.06	0.05	0.04	0.05	0.04	0.05	0.05	0.03	0.30
Other, $K^0 \pi\pi^0$ -	0.04	0.04	0.05	0.04	0.06	0.04	0.04	0.05	0.03	-0.26
Other, $K^* e\nu$ +	0.06	0.06	0.06	0.05	0.07	0.06	0.09	0.09	0.21	-0.08
Other, $K^* e\nu$ -	0.04	0.05	0.03	0.03	0.04	0.01	-0.01	0.01	-0.17	0.10
Other, Fake Tags +	0.01	0.02	0.02	-0.01	0.01	0.01	-0.05	-0.02	-0.05	-0.07
Other, Fake Tags -	0.10	0.09	0.08	0.09	0.11	0.07	0.14	0.13	0.11	0.27
Other, Other +	0.01	0.04	0.04	0.02	0.02	-0.07	-0.16	-0.11	-1.22	-0.26
Other, Other -	0.09	0.08	0.04	0.07	0.10	0.15	0.29	0.23	1.63	1.65
EID Fakes, $\pi \to e$	0.00	0.00	0.00	0.00	0.00	0.00	0.00	0.00	0.00	0.00
EID Fakes, $K \to e$	0.00	0.00	0.00	0.00	0.00	0.00	0.00	0.00	0.00	0.00
Total Bkgd. Sys.	0.13	0.13	0.11	0.11	0.14	0.15	0.27	0.23	1.46	

6.11   Form Factor Parameterizations

Since we bin our data in q^2 and use efficiency matrices, we are not sensitive at first order to the form factor input to Monte Carlo; however, we may be sensitive to non-linear variations within q^2 bins. Systematic uncertainties due to this effect are estimated by reweighting signal MC using alternate form factors. The alternate parameterizations follow the three-parameter series expansion model, with parameters chosen based on measurements in data. We choose four combinations of parameters that lie along the error ellipse of our 3-parameter series expansion fits, and average the covariance matrices resulting from each combination. The resulting systematic uncertainties on the partial rates are shown in Table 6.17.

Table 6.17: Form Factor Systematics: Changes in $\Delta\Gamma_i$ in percent when efficiency matrices are reformed with MC weighted to follow the three parameter series expansion model with parameters r_1 and r_2

	$\Delta\Gamma_1$	$\Delta\Gamma_2$	$\Delta\Gamma_3$	$\Delta\Gamma_4$	$\Delta\Gamma_5$	$\Delta\Gamma_6$	$\Delta\Gamma_7$	$\Delta\Gamma_8$	$\Delta\Gamma_9$
$D^0 \to \pi^- e^+ \nu_e$	0.06	-0.05	-0.05	-0.05	-0.07	-0.11	-0.04		
$D^0 \to K^- e^+ \nu_e$	0.02	-0.02	-0.02	-0.01	-0.01	-0.01	0.00	0.02	-0.08
$D^+ \to \pi^0 e^+ \nu_e$	0.15	-0.03	-0.07	-0.06	-0.10	-0.15	0.57		
$D^+ \to \bar{K}^0 e^+ \nu_e$	0.03	-0.02	-0.02	-0.02	-0.02	-0.01	0.01	0.02	0.08

6.12   ISR

The effect of initial state radiation was found to be negligible for the 281 pb^{-1} analysis. To arrive at this conclusion, that analysis measured efficiencies using Monte Carlo samples split into samples of events with ISR energies $\geq$ 25 keV or $<$ 25 keV. We have followed this procedure, remeasuring rates in data with the following changes in procedure:

- Signal Efficiencies are taken from signal MC events with either $E_{ISR} \geq 25$ keV or $E_{ISR} < 25$ keV.

- Signal shapes are taken from the same sample used to obtain signal efficiencies

- Tagging Efficiencies are taken from generic Monte Carlo events with either $E_{ISR} \geq 25$ keV or $E_{ISR} < 25$ keV.

The changes in rates are around 0.1-0.2%, with the shifts dominated by the statistical uncertainty of the procedure. Because these are extreme variations – the limits of no ISR or all ISR can be ruled out. The small rate variations are therefore large over-estimates of the systematic uncertainty due to ISR simulation. We assume the true ISR systematic uncertainties are negligible.

6.13 Smearing in q^2

We have already noted that the U distributions in data appear to be slightly wider than those in the Monte Carlo, indicating that may be additional q^2 smearing in the data. Estimates of this discrepancy are somewhat difficult to come by, but one fairly simple estimate can be made by assuming that the majority of the smearing in U originates in hadron momentum measurements. A supporting piece of evidence for this hypothesis is the larger U smearing discrepancy in $D^+ \rightarrow \pi^0 e^+ \nu_e$ than in the other semileptonic modes. Using $q^2 = m_D^2 - m_{had}^2 - 2m_D E_{had}$, it follows that $\delta q^2 = -2m_D \delta E_{had}$. Given the ~ 6 MeV of additional smearing in $D^0 \rightarrow \pi^- e^+ \nu_e$, $D^0 \rightarrow K^- e^+ \nu_e$ and $D^+ \rightarrow \bar{K}^0 e^+ \nu_e$ U distributions, q^2 distributions in these modes will be smeared by an additional 0.02 GeV^2. The additional U smearing of 13 MeV in $D^+ \rightarrow \pi^0 e^+ \nu_e$ corresponds to extra q^2 smearing of 0.05 GeV^2.

To estimate the effect of such smearing, we have recalculated signal efficiency matrices by randomly smearing the reconstructed q^2 of each event in the signal Monte Carlo

Table 6.18: q^2 Smearing Systematics: Changes in $\Delta\Gamma_i$ in percent when efficiency matrices are altered to increase q^2 smearing. To reduce statistical uncetainties, the procedure was repeated 10 times with different random seeds.

	$\Delta\Gamma_1$	$\Delta\Gamma_2$	$\Delta\Gamma_3$	$\Delta\Gamma_4$	$\Delta\Gamma_5$	$\Delta\Gamma_6$	$\Delta\Gamma_7$	$\Delta\Gamma_8$	$\Delta\Gamma_9$
$\mathbf{D^0 \to \pi^- e^+ \nu_e}$									
seed 1	0.76	-0.10	-0.06	-0.27	0.17	-0.53	-0.23		
seed 2	1.02	-0.19	-0.44	-0.16	0.44	-0.60	-0.35		
seed 3	1.02	-0.19	-0.44	-0.16	0.44	-0.60	-0.35		
seed 4	0.65	0.12	-0.27	-0.18	0.31	-0.64	-0.24		
seed 5	0.83	-0.07	-0.35	-0.10	0.42	-0.63	-0.37		
seed 6	0.83	-0.07	-0.35	-0.10	0.42	-0.63	-0.37		
seed 7	0.87	-0.10	-0.34	0.10	0.05	-0.43	-0.49		
seed 8	0.85	-0.36	0.08	-0.43	0.13	-0.30	-0.21		
seed 9	0.91	-0.11	-0.30	-0.08	0.31	-0.84	-0.19		
seed 10	0.68	0.00	-0.18	-0.21	0.33	-0.84	-0.02		
avg	0.84	-0.11	-0.26	-0.16	0.30	-0.60	-0.28		
$\mathbf{D^0 \to K^- e^+ \nu_e}$									
seed 1	0.66	-0.13	-0.02	0.03	-0.22	-0.40	-0.08	-0.40	-1.89
seed 2	0.67	-0.12	0.10	-0.09	-0.26	-0.46	0.24	-0.89	-1.96
seed 3	0.52	0.03	-0.03	-0.17	0.09	-0.48	-0.06	-0.41	-2.28
seed 4	0.61	-0.10	0.19	-0.28	0.01	-0.50	0.10	-0.79	-2.22
seed 5	0.65	-0.24	0.20	-0.13	-0.16	-0.47	0.16	-0.44	-2.68
seed 6	0.66	-0.06	-0.17	0.02	-0.06	-0.47	-0.02	-0.60	-1.71
seed 7	0.66	-0.20	0.20	-0.21	0.01	-0.60	0.15	-0.73	-2.07
seed 8	0.62	-0.11	0.05	-0.06	-0.06	-0.63	0.19	-0.77	-1.73
seed 9	0.61	-0.10	0.11	-0.19	0.00	-0.56	0.03	-0.57	-2.00
seed 10	0.58	-0.06	0.05	-0.15	0.01	-0.50	0.04	-0.64	-2.01
avg	0.62	-0.11	0.07	-0.12	-0.06	-0.51	0.08	-0.62	-2.05
$\mathbf{D^+ \to \pi^0 e^+ \nu_e}$									
seed 1	1.64	-0.16	-0.84	0.60	0.58	-0.99	-1.82		
seed 2	1.49	0.47	-1.33	0.98	0.10	-1.17	-1.69		
seed 3	1.39	0.60	-1.46	0.71	0.57	-1.58	-1.12		
seed 4	2.07	0.12	-2.02	1.82	-0.74	-0.89	-1.78		
seed 5	2.00	0.30	-1.69	1.44	-0.60	-1.18	-1.55		
seed 6	1.76	0.55	-1.91	1.45	-0.56	-1.16	-1.34		
seed 7	1.59	0.69	-2.52	2.20	-0.60	-1.19	-1.41		
seed 8	1.91	0.51	-2.35	1.79	-0.48	-1.10	-1.60		
seed 9	1.19	0.20	-1.88	1.94	0.11	-1.54	-0.81		
seed 10	1.90	-0.48	-1.36	1.58	-0.11	-1.41	-1.02		
avg	1.69	0.28	-1.74	1.45	-0.17	-1.22	-1.41		
$\mathbf{D^+ \to \bar{K}^0 e^+ \nu_e}$									
seed 1	0.72	-0.18	0.04	0.12	-1.04	0.74	-0.77	-0.85	-1.38
seed 2	0.16	-0.13	-0.09	0.46	-0.90	0.78	-0.29	-0.51	-0.54
seed 3	0.16	-0.13	-0.09	0.46	-0.90	0.78	-0.29	-0.51	-0.54
seed 4	0.76	-0.28	-0.04	0.33	-1.03	0.61	-0.88	-0.67	-1.29
seed 5	0.66	-0.28	0.12	0.28	-1.21	0.80	-0.83	-0.88	-0.92
seed 6	0.73	-0.19	-0.05	0.16	-1.06	0.85	-0.86	-0.51	-1.89
seed 7	0.84	-0.37	0.03	0.25	-1.06	0.67	-0.77	-0.94	-1.06
seed 8	0.76	-0.36	-0.05	0.33	-1.06	0.75	-0.58	-1.02	-1.26
seed 9	0.72	-0.23	0.01	0.23	-1.14	0.79	-0.71	-1.06	-0.99
seed 10	0.77	-0.24	-0.09	0.29	-1.17	0.73	-0.70	-0.80	-1.19
avg	0.63	-0.24	-0.02	0.29	-1.06	0.75	-0.67	-0.78	-1.11

using a Gaussian of width $0.02\,\mathrm{GeV}^2$ or $0.05\,\mathrm{GeV}^2$, depending on the semileptonic mode in question. To reduce the statistical uncertainty on the calculation, we repeated the process ten times using a different random number seed each time. The change in partial rates resulting from each of the ten smeared efficiency matrices are shown in table 6.18. To assign a systematic uncertainty to the rates, we average the results of the ten tests. Although the resulting systematic uncertainties on the partial rates appear quite large, they actually have only a small effect on our results. Because this effect does not impact the overall efficiency, it has no effect on branching fraction measurements. The primary impact is on the form factor shape parameters, which have statistical uncertainties much larger than the systematic uncertainties.

CHAPTER 7

FORM FACTOR FITS

In the previous sections, we have extracted the partial rates $\Delta\Gamma_i$ in each mode and deter-

mined their systematic uncertainties. We now use this information to derive the semilep-

tonic branching fractions, form factor parameters and CKM matrix elements.

7.1 Fitting Technique

We fit the partial rates by minimizing:

$$\chi^2 = \sum_{i,j=1}^{m} (\Delta\Gamma_i - g(q^2)_i) C_{ij}^{-1} (\Delta\Gamma_j - g(q^2)_j) \tag{7.1}$$

where C_{ij} is the sum of the statistical and systematic covariance matrices for the $\Delta\Gamma_j$,

and $g(q^2)_j$ is the predicted partial rate in the jth bin, obtained by integrating Equation 1.1

over the q^2 bin and using a hypothesized $||V_{cd}|||f_+(q^2)|$. We perform separate fits using

five different parameterizations of $|f_+(q^2)|$. In each case, we vary $|V_{cd}||f_+(0)|$ and one

or more form factor parameters: α in the modified pole model, M_{pole} in the simple pole

model, r_{ISGW} in the ISGW2 model, r_1 in the two-parameter series expansion and r_1 and

r_2 in the three parameter series expansion. See Section 2.1 for further details on the

parameterizations. To separate the statistical and systematic uncertainties on each of

the parameters, we redo the fits using only statistical covariance matrices, taking the

systematic uncertainty to be the difference between the statistical/systematic combined

and statistical only fits in quadrature.

The form factors for $D^0 \to \pi^- e^+ \nu_e$ and $D^+ \to \pi^0 e^+ \nu_e$ are expected to be similar,

as are the form factors for $D^0 \to K^- e^+ \nu_e$ and $D^+ \to \bar{K}^0 e^+ \nu_e$. For this reason, we also

provide the results of combined fits to these isospin conjugate pairs. To accomplish this,

we again minimize the χ^2 given in Eq. 7.1, now modified so that the $\Delta\Gamma_i$ for the isospin

conjugate modes are combined into one vector of length $2m$ and C_{ij} becomes a $2m \times 2m$

covariance matrix for the combined $\Delta\Gamma_i$; m is the number of q^2 bins for the modes in question. The individual covariance matrices for each semileptonic mode (described in section 6) form the diagonal blocks of the combined covariance matrices. The off-diagonal blocks are formed by assuming that that the systematic uncertainties related to tag line shapes, fake tags, positron identification and final state radiation are fully correlated across semileptonic mode while all other systematic and statistical uncertainties are uncorrelated. The combined covariance matrices are shown in Tables 7.1-7.4.
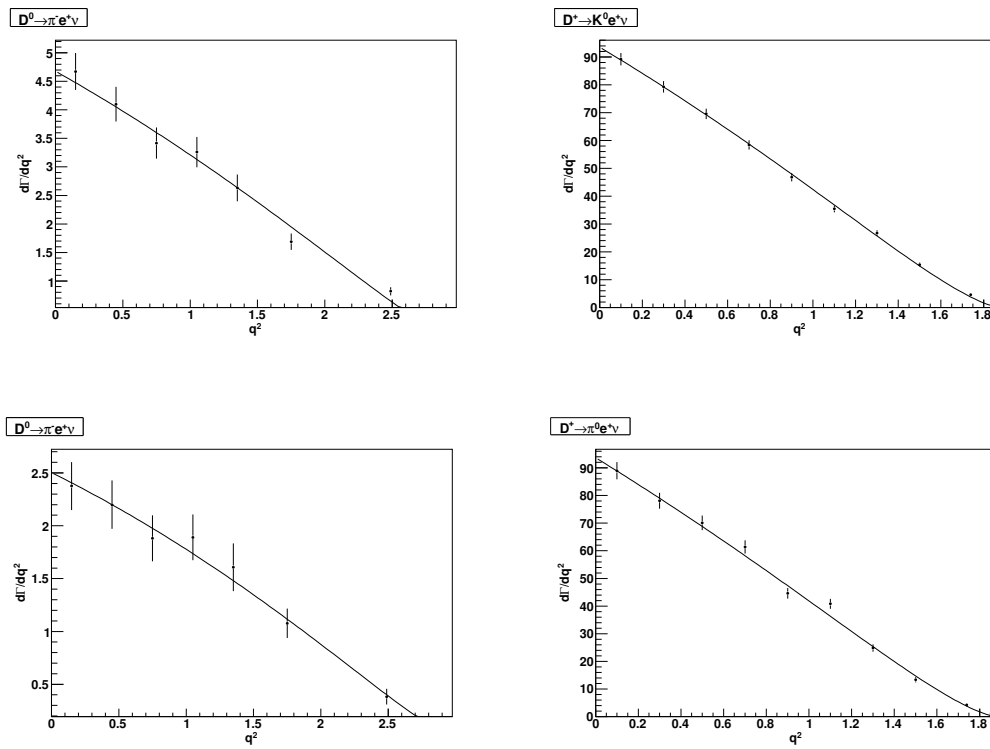
Figure 7.1: Fits to partial rates using a series parameterization with 2 parameters. Error bars show statistical and systematic uncertainties.
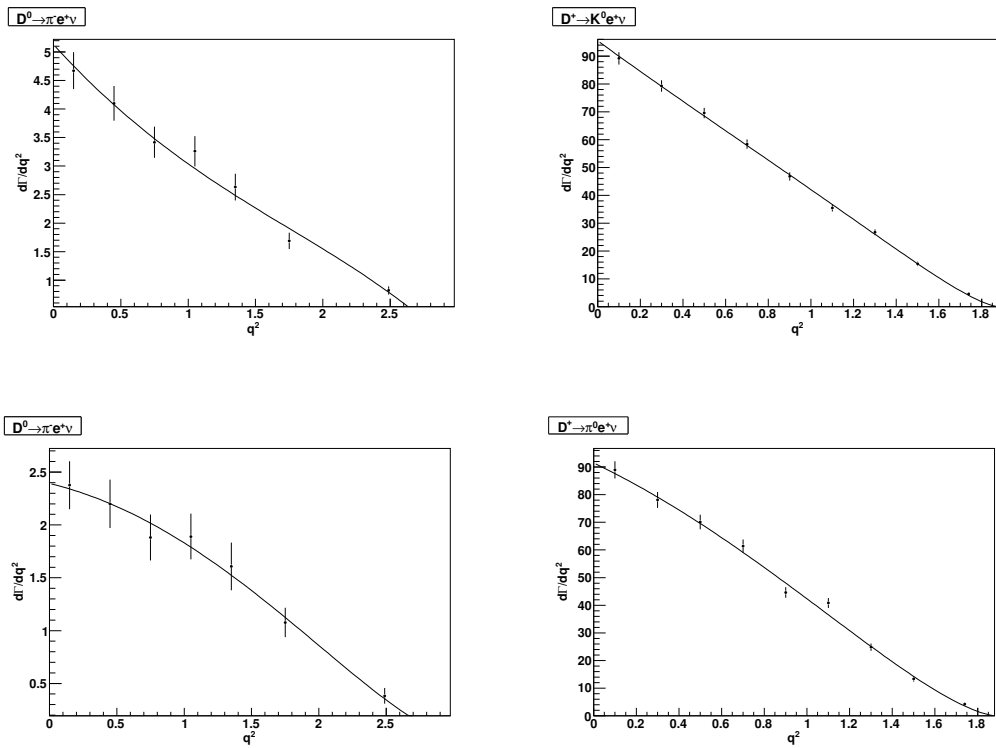
Figure 7.2: Fits to partial rates using a series parameterization with 3 parameters. Error bars show statistical and systematic uncertainties.
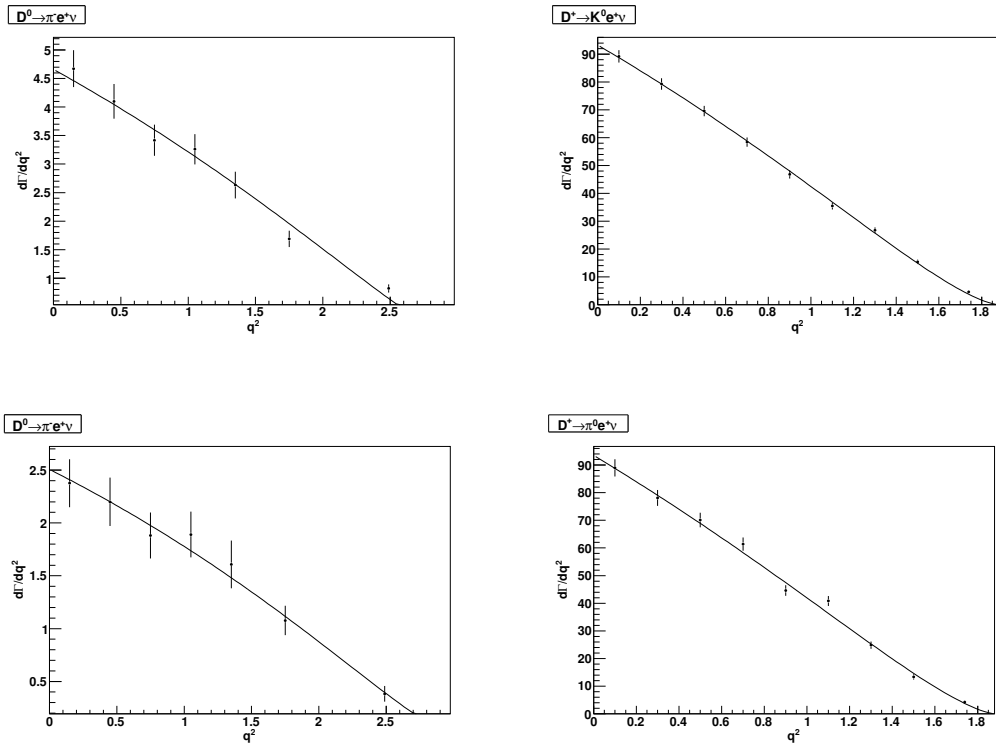
Figure 7.3: Fits to partial rates using a modified pole parameterization. Error bars show statistical and systematic uncertainties.
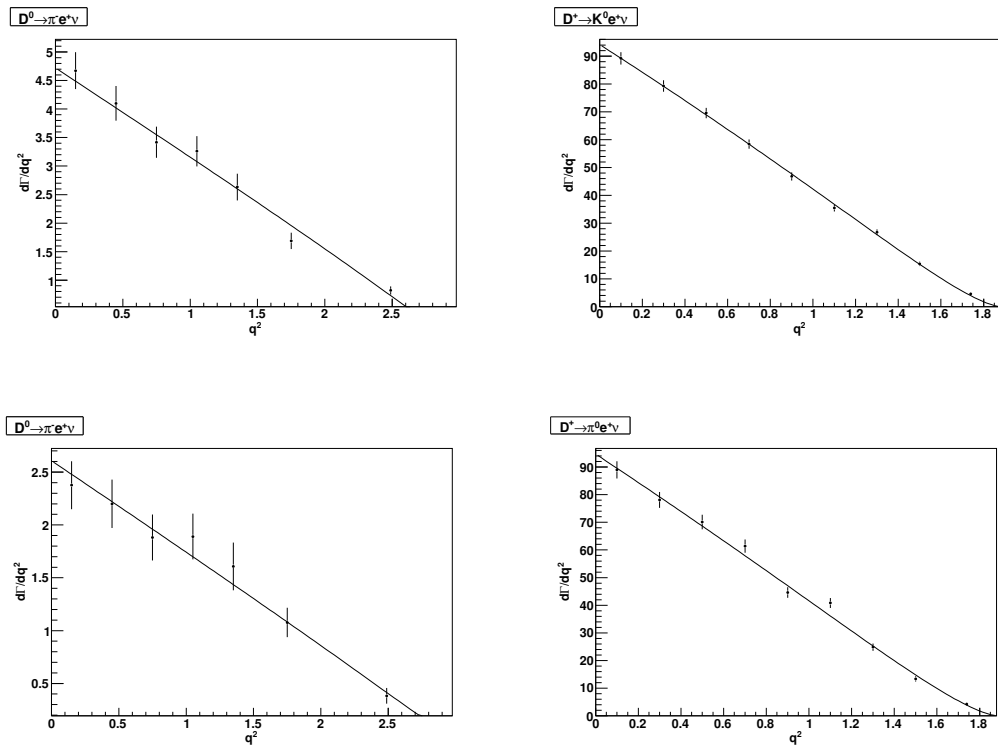
Figure 7.4: Fits to partial rates using a single pole parameterization. Error bars show statistical and systematic uncertainties.
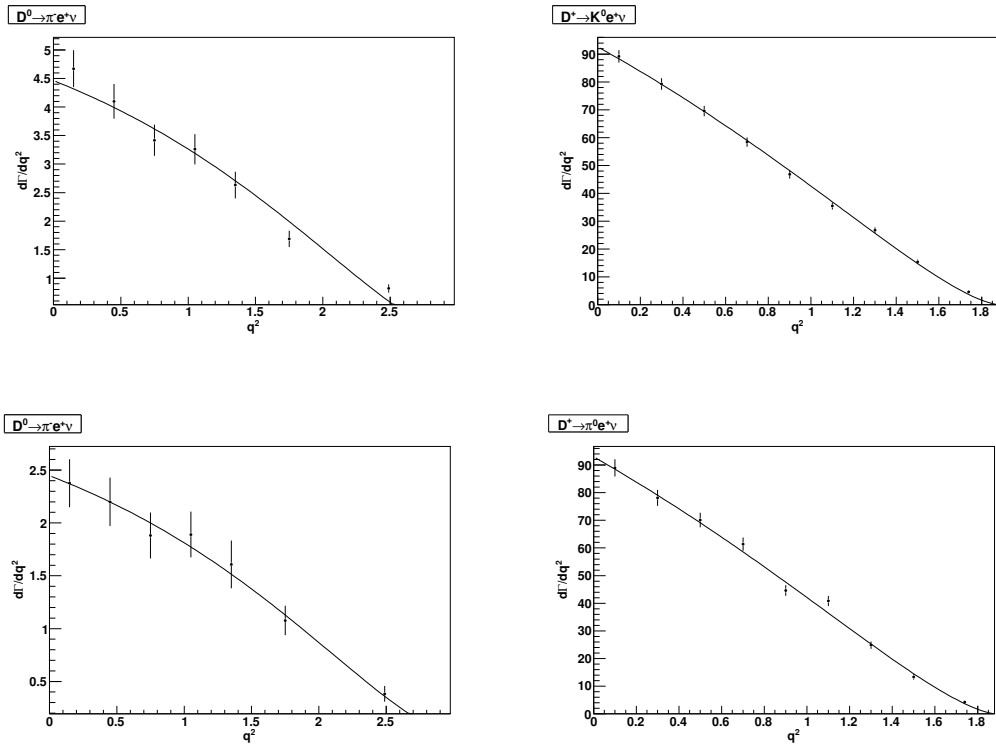
Figure 7.5: Fits to partial rates using the ISGW2 parameterization. Error bars show statistical and systematic uncertainties.
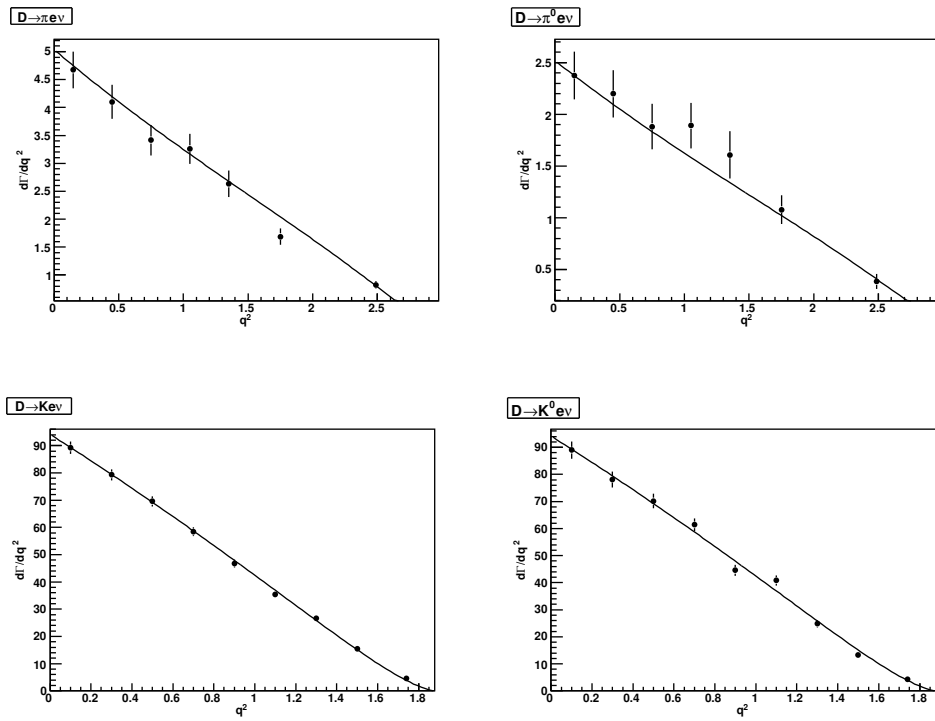
Figure 7.6: Isospin-combined fits to partial rates using a series parameterization with 3 parameters. Error bars show statistical and systematic uncertainties.

7.2 Form Factor Parameter Results

Fits to the partial rates of each semileptonic modes using each of models described above are shown in Figures 7.2-7.5. The form factor parameters resulting from these fits are shown in Table 7.5; the parameters obtained from isospin-combined fits are shown in Table 7.6

The quality of the fits are reasonable for all parameterizations; as long as at the normalization and at least one shape parameter are allowed to float, all models describe the data well. However, our results do support several conclusions that cast doubt on the ISGW2, simple pole and modified pole models. The $r_{ISGW2} = 1.12$ GeV^{-1} parameter predicted by the ISGW2 quark model is completely ruled out by our measurements. The preferred value for M_{pole} is also many standard deviations from the D^* mass predicted by the simple pole model. Calculating $1 + 1/\beta - \alpha$, defined in Eq. 2.14, using the results of the three parameter series expansion fits to each semileptonic mode, we find:

$$1 + 1/\beta - \delta\left(D^0 \rightarrow \pi^- e^+ \nu_e\right) = 1.03 \pm 0.11 \pm 0.01$$

$$1 + 1/\beta - \delta\left(D^0 \rightarrow K^- e^+ \nu_e\right) = 0.94 \pm 0.05 \pm 0.02$$

$$1 + 1/\beta - \delta\left(D^+ \rightarrow \pi^0 e^+ \nu_e\right) = 0.73 \pm 0.19 \pm 0.05$$

$$1 + 1/\beta - \delta\left(D^+ \rightarrow \bar{K}^0 e^+ \nu_e\right) = 0.80 \pm 0.06 \pm 0.01$$

. From the isospin-combined fits, we find:

$$1 + 1/\beta - \delta\left(D \rightarrow \pi/\pi^0 ev\right) = 0.94 \pm 0.09 \pm 0.02$$

$$1 + 1/\beta - \delta\left(D \rightarrow K/K^0 ev\right) = 0.89 \pm 0.04 \pm 0.01$$

. These values do not support the assumption by the modified pole model that $1 + 1/\beta - \alpha \approx 2$.

Both the two and three parameter formulations of the series model produce fits of reasonable quality. In all modes but the $D^+ \rightarrow \bar{K}^0 e^+ \nu_e$ (where all parameterizations

Table 7.1: Statistical correlation matrix for $D^0 \to \pi^- e^+ \nu_e$ and $D^+ \to \pi^0 e^+ \nu_e$ using the standard q^2 binning. q^2 increases from left to right and from top to bottom

	$D^0 \to \pi^- e^+ \nu_e$							$D^+ \to \pi^0 e^+ \nu_e$						
$D^0 \to \pi^- e^+ \nu_e$	1.000	-0.050	0.001	0.000	0.000	0.000	0.000	0.000	0.000	0.000	0.000	0.000	0.000	0.000
		1.000	-0.060	0.001	0.000	0.000	0.000	0.000	0.000	0.000	0.000	0.000	0.000	0.000
			1.000	-0.060	0.001	0.000	0.000	0.000	0.000	0.000	0.000	0.000	0.000	0.000
				1.000	-0.062	0.000	0.000	0.000	0.000	0.000	0.000	0.000	0.000	0.000
					1.000	-0.046	0.000	0.000	0.000	0.000	0.000	0.000	0.000	0.000
						1.000	-0.030	0.000	0.000	0.000	0.000	0.000	0.000	0.000
							1.000	0.000	0.000	0.000	0.000	0.000	0.000	0.000
$D^+ \to \pi^0 e^+ \nu_e$								1.000	-0.092	0.008	0.000	0.000	0.000	-0.005
									1.000	-0.121	0.011	0.000	0.000	-0.006
										1.000	-0.133	0.011	-0.001	-0.008
											1.000	-0.128	0.006	-0.013
												1.000	-0.104	-0.016
													1.000	-0.095
														1.000

Table 7.2: Systematic correlation matrix for $D^0 \to \pi^- e^+ \nu_e$ and $D^+ \to \pi^0 e^+ \nu_e$ using the standard q^2 binning. q^2 increases from left to right and from top to bottom

	$D^0 \to \pi^- e^+ \nu_e$							$D^+ \to \pi^0 e^+ \nu_e$						
$D^0 \to \pi^- e^+ \nu_e$	1.000	0.690	0.586	0.469	0.753	0.302	0.322	0.124	0.170	0.096	0.139	0.045	0.054	0.036
		1.000	0.930	0.845	0.841	0.793	0.746	0.148	0.279	0.173	0.122	0.144	0.128	0.039
			1.000	0.791	0.794	0.885	0.722	0.181	0.269	0.159	0.193	0.097	0.103	0.054
				1.000	0.887	0.729	0.818	0.081	0.351	0.247	-0.046	0.309	0.231	0.012
					1.000	0.663	0.696	0.168	0.412	0.277	0.091	0.291	0.243	0.050
						1.000	0.706	0.181	0.278	0.176	0.203	0.134	0.147	0.075
							1.000	0.056	0.301	0.220	-0.053	0.296	0.236	0.028
$D^+ \to \pi^0 e^+ \nu_e$								1.000	0.715	0.103	0.593	0.563	0.205	-0.212
									1.000	0.347	0.551	0.606	0.627	-0.082
										1.000	-0.167	0.708	0.480	0.460
											1.000	0.031	0.345	0.103
												1.000	0.555	0.094
													1.000	0.240
														1.000

Table 7.3: Statistical correlation matrix for $D^0 \to K^- e^+ \nu_e$ and $D^+ \to \bar{K}^0 e^+ \nu_e$ using the standard q^2 binning. q^2 increases from left to right and from top to bottom

		$K^\pm$									K^0							
$K^\pm$	1.00	-0.05	0.01	0.00	0.00	0.00	0.00	0.00	0.00	0.00	0.00	0.00	0.00	0.00	0.00	0.00	0.00	0.00
		1.00	-0.07	0.01	0.00	0.00	0.00	0.00	0.00	0.00	0.00	0.00	0.00	0.00	0.00	0.00	0.00	0.00
			1.00	-0.07	0.00	0.00	0.00	0.00	0.00	0.00	0.00	0.00	0.00	0.00	0.00	0.00	0.00	0.00
				1.00	-0.07	0.00	0.00	0.00	0.00	0.00	0.00	0.00	0.00	0.00	0.00	0.00	0.00	0.00
					1.00	-0.06	0.00	0.00	0.00	0.00	0.00	0.00	0.00	0.00	0.00	0.00	0.00	0.00
						1.00	-0.06	0.00	0.00	0.00	0.00	0.00	0.00	0.00	0.00	0.00	0.00	0.00
							1.00	-0.05	0.00	0.00	0.00	0.00	0.00	0.00	0.00	0.00	0.00	0.00
								1.00	-0.04	0.00	0.00	0.00	0.00	0.00	0.00	0.00	0.00	0.00
									1.00	0.00	0.00	0.00	0.00	0.00	0.00	0.00	0.00	0.00
K^0										1.00	-0.05	0.01	0.00	0.00	0.00	0.00	0.00	0.00
											1.00	-0.07	0.01	0.00	0.00	0.00	0.00	0.00
												1.00	-0.07	0.01	0.00	0.00	0.00	0.00
													1.00	-0.07	0.00	0.00	0.00	0.00
														1.00	-0.07	0.00	0.00	0.00
															1.00	-0.06	0.00	-0.00
																1.00	-0.06	0.00
																	1.00	-0.05
																		1.00

Table 7.4: Systematic correlation matrix for $D^0 \to K^- e^+ \nu_e$ and $D^+ \to \bar{K}^0 e^+ \nu_e$ using the standard q^2 binning. q^2 increases from left to right and from top to bottom

	$K^\pm$									K^0								
$K^\pm$	1.00	0.86	0.90	0.83	0.84	0.63	0.68	0.35	0.07	0.02	0.02	0.02	0.02	0.02	0.02	0.02	0.02	0.01
		1.00	0.97	0.96	0.96	0.88	0.75	0.60	0.49	0.02	0.02	0.02	0.02	0.02	0.03	0.03	0.02	0.01
			1.00	0.98	0.96	0.86	0.79	0.56	0.41	0.03	0.03	0.03	0.03	0.03	0.03	0.03	0.03	0.02
				1.00	0.98	0.92	0.81	0.61	0.52	0.03	0.03	0.03	0.03	0.04	0.04	0.04	0.04	0.03
					1.00	0.92	0.81	0.60	0.49	0.04	0.04	0.04	0.04	0.04	0.04	0.05	0.04	0.03
						1.00	0.85	0.79	0.75	0.05	0.05	0.05	0.06	0.06	0.06	0.07	0.06	0.04
							1.00	0.81	0.48	0.08	0.08	0.08	0.09	0.09	0.10	0.11	0.10	0.07
								1.00	0.80	0.12	0.13	0.15	0.13	0.13	0.15	0.15	0.15	0.08
									1.00	0.17	0.18	0.20	0.20	0.19	0.22	0.23	0.23	0.14
K^0										1.00	0.93	0.94	0.98	0.73	0.96	0.74	0.73	0.60
											1.00	0.97	0.96	0.93	0.87	0.90	0.90	0.76
												1.00	0.94	0.87	0.90	0.83	0.84	0.65
													1.00	0.82	0.95	0.84	0.83	0.70
														1.00	0.68	0.96	0.97	0.83
															1.00	0.74	0.72	0.58
																1.00	0.99	0.89
																	1.00	0.88
																		1.00

Table 7.5: Results of form factor fits; statistical and systematic uncertainties on the least significant digits are shown in parentheses

3 Par Series	$f_+(0)\left\vert V_{cq}\right\vert$	r_1	r_2	$\rho_{01}, \rho_{02}, \rho_{12}$	$\chi^2/d.o.f$
$D^0 \to \pi^- e^+ \nu_e$	0.152(5)(1)	-2.80(49)(5)	7(3)(0)	-0.44 0.69 -0.94	4.5/4
$D^0 \to K^- e^+ \nu_e$	0.726(8)(6)	-2.62(34)(10)	13(9)(2)	-0.15 -0.56 0.83	2.9/6
$D^+ \to \pi^0 e^+ \nu_e$	0.146(7)(2)	-1.36(88)(23)	-4(5)(1)	-0.44 0.65 -0.96	0.9/4
$D^+ \to \bar{K}^0 e^+ \nu_e$	0.709(10)(10)	-1.61(44)(9)	-14(11)(2)	-0.12 0.55 -0.82	13.3/6
	a_0	a_1	a_2	$\rho_{01}, \rho_{02}, \rho_{12}$	
$D^0 \to \pi^- e^+ \nu_e$	0.071(2)(1)	-0.20(4)(0)	0.5(2)(0)	-0.44 0.69 -0.94	
$D^0 \to K^- e^+ \nu_e$	-0.026(0)(0)	0.07(1)(0)	-0.3(2)(0)	-0.15 -0.56 0.83	
$D^+ \to \pi^0 e^+ \nu_e$	0.074(3)(2)	-0.10(7)(2)	-0.3(4)(1)	-0.44 0.65 -0.96	
$D^+ \to \bar{K}^0 e^+ \nu_e$	-0.026(0)(0)	0.04(1)(0)	0.4(3)(0)	-0.12 0.55 -0.82	
2 Par Series	$f_+(0)\left\vert V_{cq}\right\vert$	r_1		ρ	$\chi^2/d.o.f$
$D^0 \to \pi^- e^+ \nu_e$	0.145(4)(1)	-1.85(18)(2)		0.83	8.2/5
$D^0 \to K^- e^+ \nu_e$	0.719(6)(6)	-2.20(19)(6)		0.67	4.9/7
$D^+ \to \pi^0 e^+ \nu_e$	0.150(5)(2)	-1.93(25)(7)		0.80	1.3/5
$D^+ \to \bar{K}^0 e^+ \nu_e$	0.717(7)(10)	-2.04(25)(7)		0.63	14.7/7
	a_0	a_1		ρ	
$D^0 \to \pi^- e^+ \nu_e$	0.071(2)(1)	-0.13(2)(0)		-0.89	
$D^0 \to K^- e^+ \nu_e$	-0.027(0)(0)	0.06(1)(0)		-0.55	
$D^+ \to \pi^0 e^+ \nu_e$	0.074(3)(1)	-0.14(2)(1)		-0.92	
$D^+ \to \bar{K}^0 e^+ \nu_e$	-0.026(0)(0)	0.05(1)(0)		-0.45	
Modified Pole	$f_+(0)\left\vert V_{cq}\right\vert$	α		ρ	$\chi^2/d.o.f$
$D^0 \to \pi^- e^+ \nu_e$	0.145(4)(1)	0.20(8)(1)		-0.82	8.5/5
$D^0 \to K^- e^+ \nu_e$	0.718(6)(6)	0.30(4)(1)		-0.66	5.4/7
$D^+ \to \pi^0 e^+ \nu_e$	0.150(5)(2)	0.24(11)(3)		-0.77	1.3/5
$D^+ \to \bar{K}^0 e^+ \nu_e$	0.717(7)(10)	0.26(6)(1)		-0.61	14.4/7
Simple Pole	$f_+(0)\left\vert V_{cq}\right\vert$	$M_{pole}(GeV)$		ρ	$\chi^2/d.o.f$
$D^0 \to \pi^- e^+ \nu_e$	0.146(3)(2)	1.91(3)(0)		0.71	5.9/5
$D^0 \to K^- e^+ \nu_e$	0.721(5)(6)	1.92(2)(1)		0.61	3.3/7
$D^+ \to \pi^0 e^+ \nu_e$	0.153(4)(3)	1.92(4)(1)		0.64	2.2/5
$D^+ \to \bar{K}^0 e^+ \nu_e$	0.721(6)(10)	1.95(3)(1)		0.56	15.9/7
ISGW2	$f_+(0)\left\vert V_{cq}\right\vert$	r		ρ	$\chi^2/d.o.f$
$D^0 \to \pi^- e^+ \nu_e$	0.142(4)(2)	1.99(9)(1)		-0.80	12.2/5
$D^0 \to K^- e^+ \nu_e$	0.715(5)(6)	1.60(3)(1)		-0.64	6.9/7
$D^+ \to \pi^0 e^+ \nu_e$	0.148(5)(3)	2.02(12)(4)		-0.74	0.9/5
$D^+ \to \bar{K}^0 e^+ \nu_e$	0.715(7)(10)	1.57(4)(1)		-0.60	13.8/7

Table 7.6: Results of combined form factor fits to isospin conjugate pairs; statistical and systematic uncertainties on the least significant digits are shown in parentheses

3 Par Series	$f_+(0)|V_{cq}|$	r_1	r_2	$\rho_{01},\rho_{02},\rho_{12}$	$\chi^2/d.o.f$
$D \to \pi/\pi^0 e\nu$	0.150(4)(1)	-2.35(43)(7)	3(3)(0)	-0.43 0.68 -0.94	10.3/8
$D \to K/K^0 e\nu$	0.719(6)(7)	-2.23(27)(9)	2(7)(1)	-0.11 0.53 -0.81	18.6/12
	a_0	a_1	a_2	$\rho_{01},\rho_{02},\rho_{12}$	
$D \to \pi/\pi^0 e\nu$	0.072(2)(1)	-0.17(3)(1)	0.3(2)(0)	-0.43 0.68 -0.94	
$D \to K/K^0 e\nu$	-0.026(0)(0)	0.06(1)(0)	-0.1(2)(0)	-0.11 0.53 -0.81	
2 Par Series	$f_+(0)|V_{cq}|$	r_1		ρ	$\chi^2/d.o.f$
$D \to \pi/\pi^0 e\nu$	0.147(3)(1)	-1.86(15)(4)		0.81	11.6/10
$D \to K/K^0 e\nu$	0.718(4)(7)	-2.16(15)(7)		0.62	18.7/14
	a_0	a_1		ρ	
$D \to \pi/\pi^0 e\nu$	0.071(2)(1)	-0.13(1)(0)		-0.89	
$D \to K/K^0 e\nu$	-0.026(0)(0)	0.06(0)(0)		-0.51	
Modified Pole	$f_+(0)|V_{cq}|$	α		ρ	$\chi^2/d.o.f$
$D \to \pi/\pi^0 e\nu$	0.147(3)(1)	0.21(7)(2)		-0.80	12.1/10
$D \to K/K^0 e\nu$	0.717(4)(7)	0.29(3)(2)		-0.61	18.9/14
Simple Pole	$f_+(0)|V_{cq}|$	$M_{pole}(GeV)$		ρ	$\chi^2/d.o.f$
$D \to \pi/\pi^0 e\nu$	0.148(2)(2)	1.92(2)(1)		0.69	10.2/10
$D \to K/K^0 e\nu$	0.721(4)(7)	1.93(2)(1)		0.55	18.7/14
ISGW2	$f_+(0)|V_{cq}|$	r		ρ	$\chi^2/d.o.f$
$D \to \pi/\pi^0 e\nu$	0.144(3)(2)	1.99(7)(2)		-0.78	15.9/10
$D \to K/K^0 e\nu$	0.715(4)(7)	1.59(2)(1)		-0.59	19.8/14

have slightly large values of χ^2 due to a statistical fluctuation between the fifth and sixth q^2 bins), the χ^2 per degree of freedom using a three parameter fit is smaller than that obtained with a two parameter fit. The strongest evidence for a non-zero value of a_2 is in $D^0 \to \pi^- e^+ \nu_e$, where $r_2 = a_2/a_0$ is slightly more than two standard deviations larger than zero. Thus, although there are hints of a preference for the three parameter fit, we do not have sufficient statistical evidence to draw strong conclusions on this point.
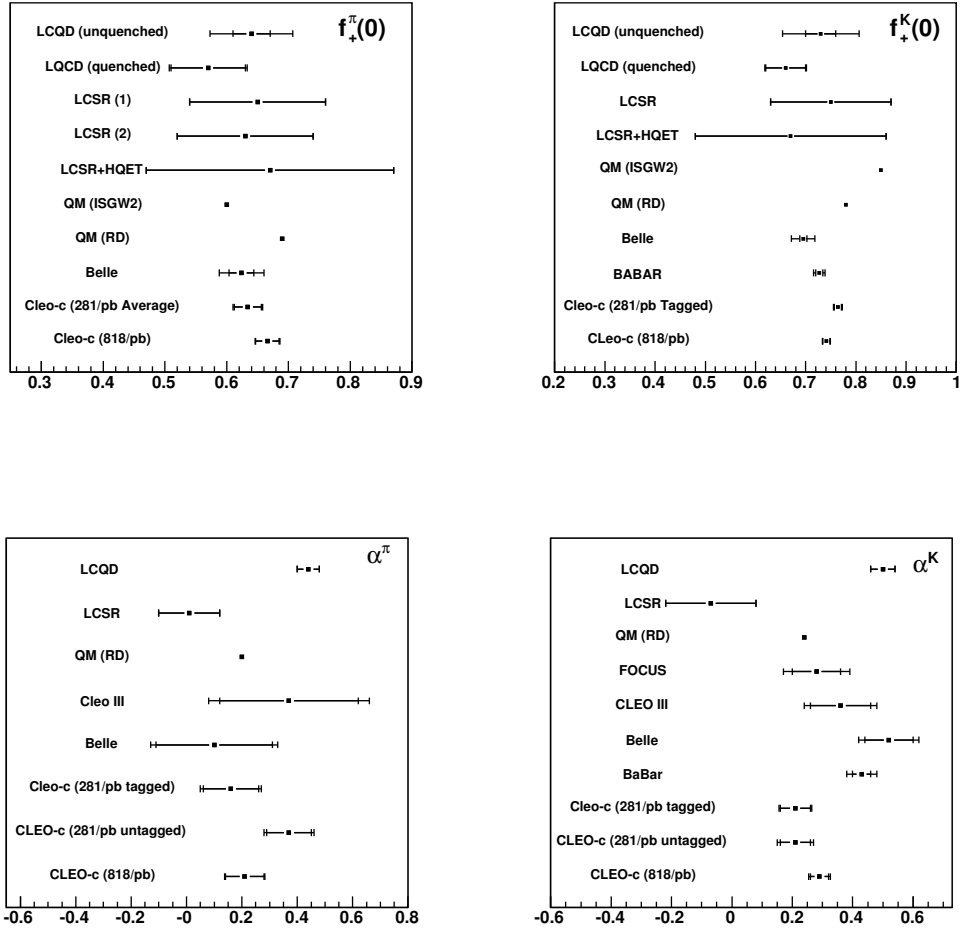
Figure 7.7: Comparison of theoretical predictions and experimental measurements of D semileptonic form factor parameters.

Figures 7.7 gives an update of the form factor parameter comparisons shown in Section 2.4, now with our results shown by the points labeled "CLEO-c 818/pb." In all cases, our results are in reasonable agreement with the results of other experiments. We also agree well with Lattice QCD results for $f_+(0)$. Our α parameter is lower than the LQCD prediction, but as systematic uncertainties on the LQCD value are not available, the size of the discrepancy is difficult to quantify.

7.3 Branching Fraction Results

Branching fractions are extracted from the three parameter series expansion fit by integrating the optimized $d\Gamma/dq^2$ over the entire q^2 range. We find the branching fractions to be:

$$\mathcal{B}\left(D^0 \to \pi^- e^+ \nu_e\right) = (0.289 \pm 0.008 \pm 0.003)\%$$

$$\mathcal{B}\left(D^0 \to K^- e^+ \nu_e\right) = (3.51 \pm 0.03 \pm 0.05)\%$$

$$\mathcal{B}\left(D^+ \to \pi^0 e^+ \nu_e\right) = (0.405 \pm 0.016 \pm 0.009)\%$$

$$\mathcal{B}\left(D^+ \to \bar{K}^0 e^+ \nu_e\right) = (8.83 \pm 0.10 \pm 0.19)\%$$

Figure 7.8 shows our branching fraction measurements in comparison with other experimental results. Included in these plots are the averaged results of a tagged and an untagged analysis of the initial 281 pb^{-1} of CLEO-c data. While this sample forms a subset corresponding to about one third of the data analyzed here, the systematic uncertainties of the measurements in this work are largely uncorrelated with those of the previous measurements due to significantly different analysis techniques. The differences between the results reported here and those of previous CLEO-c measurements are consistent within statistical and systematic uncertainties. We also find the branching

fractions reported here to be in excellent agreement with all available results from other experiments.
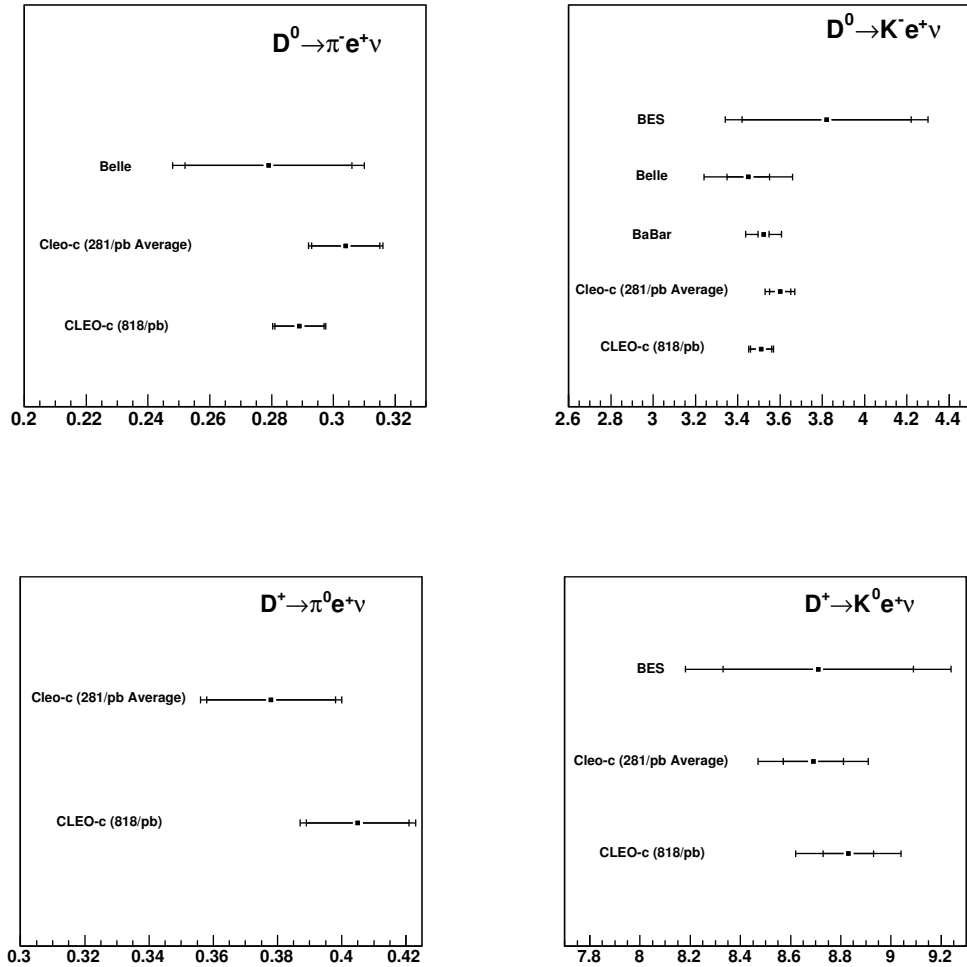
Figure 7.8: Comparison of measurements of *D* semileptonic branching fractions.

7.4 Extraction of V_{cd} and V_{cs}
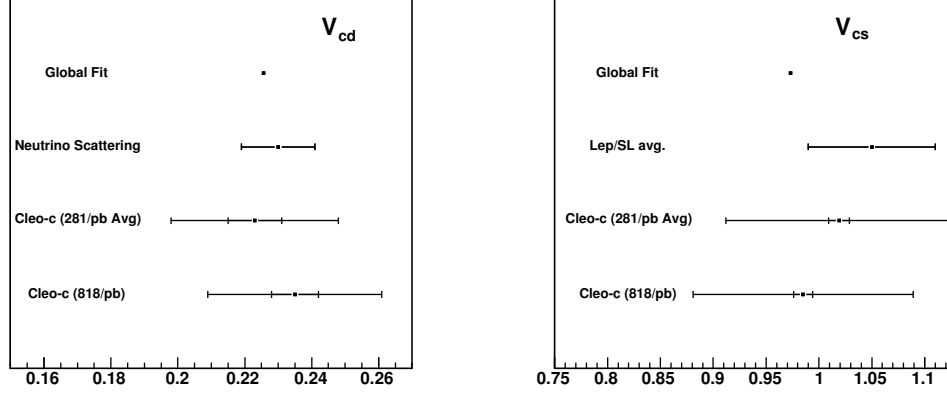
Figure 7.9: Comparison of measurements of CKM matrix elements.

To extract the CKM matrix elements V_{cd} and V_{cs}, we take the $f_+(0)V_{cq}$ values from the isospin-combined three parameter series expansion fits and use the Lattice QCD measurements [8] $f_+(0) = 0.64 \pm 0.03 \pm 0.06$ for $D \to \pi$ transitions and $f_=(0) = 0.73 \pm 0.03 \pm 0.07$ for $D \to K$ transition, finding:

$$V_{cd} = 0.235 \pm 0.007 \pm 0.002 \pm 0.025$$

$$V_{cs} = 0.985 \pm 0.009 \pm 0.007 \pm 0.103$$

where the third error is due to LQCD. These values are in agreement with other CKM measurements, shown in figure 7.9.

CROSS-CHECKS

We have executed several consistency checks to look for possible problems with the analysis procedure. These include comparisons of the results across different tag modes, between isospin conjugate modes and in different data samples. As further verification of the signal yield fits, we have studied data/Monte Carlo agreement in kinematic distributions other than U and q^2. None of these tests, each of which is documented below, indicates a problem with the analysis.

8.1   Consistency of Results Across Tag Modes

Table 8.1: Variance of Partial Rates Across Tag Modes

SL mode	Expected	Variance
$D^0 \to \pi^- e^+ \nu_e$	12	14 ± 5
$D^0 \to K^- e^+ \nu_e$	21	18 ± 6
$D^+ \to \pi^0 e^+ \nu_e$	36	35 ± 8
$D^+ \to \bar{K}^0 e^+ \nu_e$	37	45 ± 9

The decision to fit signal and tag yields separately for each tag mode was made in order to allow for different background normalizations in the different tag modes. The choice also allows comparisons of results in different tag modes. The partial rates as a function of q^2 are shown in Figure 5.2 for each of the tag modes. By eye, the tag modes agree reasonably well; to quantify this agreement, we compute the variance of the rates using:

$$Var\left(\Gamma\right) = \sum_{i}^{N_{tags}} \sum_{j}^{N_{qsqbins}} \frac{\left(\Gamma_{ij} - \bar{\Gamma}_j\right)^2}{\sigma_{ij}^2} \tag{8.1}$$

where Γ_{ij} is the partial rate for bin j measured in tag mode i, $\bar{\Gamma}_j$ is the rate for bin j averaged over tag modes and σ_{ij} is the uncertainty on Γ_{ij}. This variance is expected to

have a χ^2 distribution, with mean n_{dof} and variance $2n_{dof}$, where the number of degrees of freedom $n_{dof} = n_{q^2 \text{ bins}} \times (n_{\text{tag modes}} - 1)$. The observed variances for each mode are given in Table 8.1; they agree well with their expected values.

8.2 Isospin Conjugate Comparison

Figure 8.1: $|f_+(q^2)|^2|V_{cq}|^2$ for each mode, with isospin conjugate modes overlaid. Points have been symmetrically offset from bin centers to facilitate display.
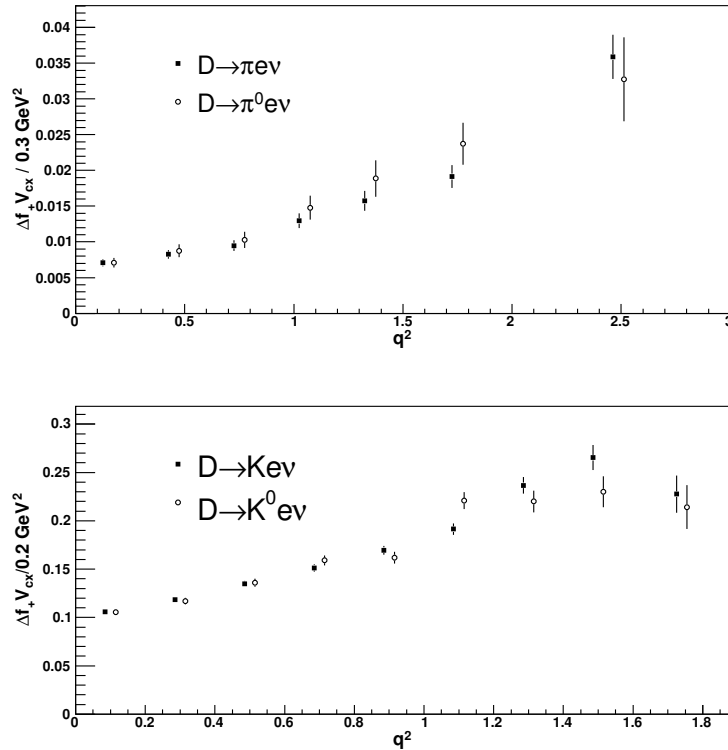
Figure 8.1 shows $\left|f_+(q^2)\right|\left|V_{cq}\right|^2$ for each semileptonic mode, with isospin conjugate modes overlaid. This plot is formed by normalizing the standard partial rate results by $p^3 G_F^2/24\pi^3$ (where p is the average momentum for the q^2 bin). This quantity is expected to be the same for isospin conjugate modes (within a theoretical uncertainty of up to a

few percent). Indeed, we find that $\left|f_+\left(q^2\right)\right|^2 \left|V_{cq}\right|^2$ integrated over q^2 differ by -0.07 ± 0.08 for the $\pi e\nu$ modes and 0.023 ± 0.026 for the $Ke\nu$ modes.

Figure 8.2: Partial rates with isospin conjugate modes overlaid. Points have been symmetrically offset from q^2 bin centers to facilitate display.
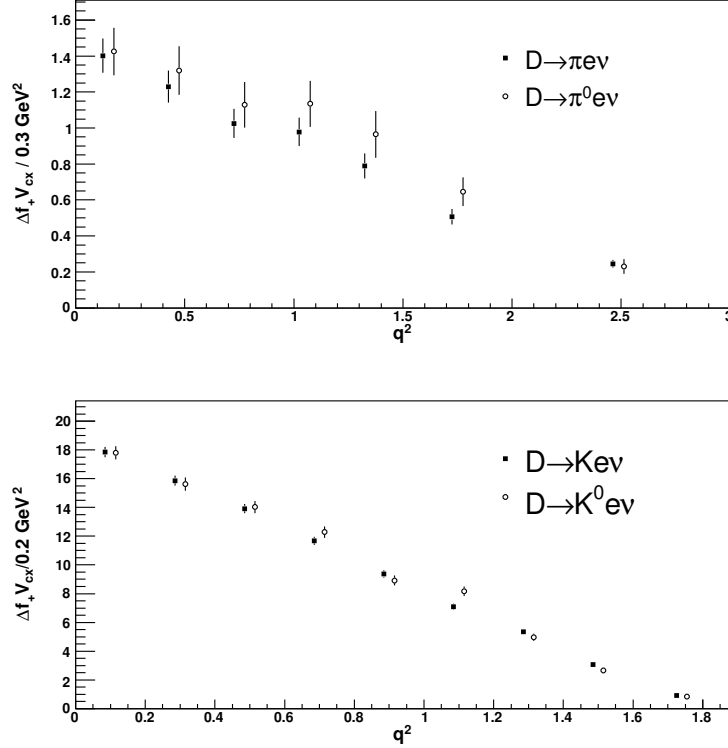
The partial rates are also expected to roughly agree for the isospin conjugate modes. These are shown in figure 8.2. The rates summed over q^2 differ by 0.10 ± 0.06 for the $\pi e\nu$ modes and 0.002 ± 0.015 for the $Ke\nu$ modes. Part of the rate asymmetries arise from the difference between the $\pi^\pm/\pi^0$ and $K^\pm/K^0$ masses. Taking this into account, the summed rates differ by 0.08 ± 0.06 and 0.006 ± 0.015. Whether one considers integrated form factors or rates, the conclusion is the same: the results for isospin conjugate modes agree.

8.3 Comparison of Results in Earlier and Later Data

Table 8.2: Tag Yields in 281 pb^{-1} of data and 537 pb^{-1} of data using the procedures of this analysis. All tag cuts, including M_{BC} have been applied. Based on the luminosities in the two samples, the ratio of yields is expected to be 1.91.

mode	Yield (281)	Yield (537)	Ratio	Yield/pb (281)	Yield/pb (537)
$D^0 \to K^-\pi^+$	51535 ± 230	97905 ± 318	1.900 ± 0.010	183	182
$D^0 \to K^-\pi^+\pi^0$	98510 ± 347	186847 ± 479	1.897 ± 0.008	351	348
$D^0 \to K^-\pi^+\pi^+\pi^-$	78351 ± 303	148800 ± 419	1.899 ± 0.009	279	277
$D^+ \to K^-\pi^+\pi^+$	80566 ± 291	153110 ± 403	1.900 ± 0.008	287	285
$D^+ \to K^-\pi^+\pi^+\pi^0$	24119 ± 195	45644 ± 266	1.892 ± 0.019	86	85
$D^+ \to K^0_S\pi^+$	11559 ± 116	22287 ± 157	1.928 ± 0.023	41	42
$D^+ \to K^0_S\pi^+\pi^0$	25652 ± 210	49407 ± 272	1.926 ± 0.019	91	92
$D^+ \to K^0\pi^+\pi^+\pi^-$	16815 ± 190	32271 ± 245	1.919 ± 0.026	60	60
$D^+ \to K^+K^-\pi^+$	6882 ± 100	13033 ± 138	1.894 ± 0.034	24	24

We have compared our results in the initial 281 pb^{-1} and final 537 pb^{-1} of CLE0-c data to exclude significant changes in detector performance through the several years of data-taking. Table 8.2 shows the yields produced by our tag yield fitter when run over the 281 pb^{-1} and 537 pb^{-1} data samples separately. The ratios of these yields agree well with the expected ratio of 1.91. Signal yields in the two samples are shown in Table 8.3. While the yield ratios here are also consistent with 1.91, the $D^0 \to \pi^- e^+ \nu_e$ and $D^0 \to K^- e^+ \nu_e$ ratios are all slightly smaller than expected. We have studied these fits in detail and find no evidence that this is anything other than a statistical fluctuation. The partial rates observed in these two data samples, obtained using the same signal and tag efficiencies, are shown in Figure 8.3.

Table 8.3: Signal Yields in 281 pb^{-1} of data and 537 pb^{-1} using the standard procedures of this analysis (and summing yields from all q^2 bins). Based on the luminosities in the two samples, the ratio of yields is expected to be 1.91.

SL mode	tagmode	281 pb^{-1}	537 pb^{-1}	Ratio (%)
$D^0 \to \pi^- e^+ \nu_e$	$D^0 \to K^- \pi^+$	115 ± 11	197 ± 13	1.71 ± 0.21
$D^0 \to \pi^- e^+ \nu_e$	$D^0 \to K^- \pi^+ \pi^0$	212 ± 15	386 ± 21	1.82 ± 0.16
$D^0 \to \pi^- e^+ \nu_e$	$D^0 \to K^- \pi^+ \pi^+ \pi^-$	164 ± 14	297 ± 18	1.81 ± 0.19
$D^0 \to \pi^- e^+ \nu_e$	All Tags	492 ± 23	879 ± 31	1.79 ± 0.11
$D^0 \to K^- e^+ \nu_e$	$D^0 \to K^- \pi^+$	1100 ± 34	2013 ± 46	1.83 ± 0.07
$D^0 \to K^- e^+ \nu_e$	$D^0 \to K^- \pi^+ \pi^0$	2146 ± 47	4023 ± 65	1.87 ± 0.05
$D^0 \to K^- e^+ \nu_e$	$D^0 \to K^- \pi^+ \pi^+ \pi^-$	1698 ± 42	3140 ± 57	1.85 ± 0.06
$D^0 \to K^- e^+ \nu_e$	All Tags	4944 ± 72	9176 ± 98	1.86 ± 0.03
$D^+ \to \pi^0 e^+ \nu_e$	$D^+ \to K^- \pi^+ \pi^+$	140 ± 13	269 ± 18	1.93 ± 0.22
$D^+ \to \pi^0 e^+ \nu_e$	$D^+ \to K^- \pi^+ \pi^+ \pi^0$	37 ± 7	76 ± 10	2.08 ± 0.49
$D^+ \to \pi^0 e^+ \nu_e$	$D^+ \to K^0_S \pi^+$	21 ± 5	32 ± 6	1.49 ± 0.45
$D^+ \to \pi^0 e^+ \nu_e$	$D^+ \to K^0_S \pi^+ \pi^0$	50 ± 8	91 ± 10	1.84 ± 0.36
$D^+ \to \pi^0 e^+ \nu_e$	$D^+ \to K^0 \pi^+ \pi^+ \pi^-$	32 ± 6	56 ± 9	1.74 ± 0.43
$D^+ \to \pi^0 e^+ \nu_e$	$D^+ \to K^+ K^- \pi^+$	9 ± 5	21 ± 9	2.34 ± 1.31
$D^+ \to \bar{K}^0 e^+ \nu_e$	All Tags	289 ± 19	546 ± 36	1.89 ± 0.19
$D^+ \to \bar{K}^0 e^+ \nu_e$	$D^+ \to K^- \pi^+ \pi^+$	1441 ± 39	2769 ± 54	1.92 ± 0.06
$D^+ \to \bar{K}^0 e^+ \nu_e$	$D^+ \to K^- \pi^+ \pi^+ \pi^0$	426 ± 21	761 ± 28	1.79 ± 0.11
$D^+ \to \bar{K}^0 e^+ \nu_e$	$D^+ \to K^0_S \pi^+$	202 ± 14	413 ± 21	2.05 ± 0.18
$D^+ \to \bar{K}^0 e^+ \nu_e$	$D^+ \to K^0_S \pi^+ \pi^0$	437 ± 22	852 ± 30	1.95 ± 0.12
$D^+ \to \bar{K}^0 e^+ \nu_e$	$D^+ \to K^0 \pi^+ \pi^+ \pi^-$	270 ± 17	558 ± 24	2.06 ± 0.16
$D^+ \to \bar{K}^0 e^+ \nu_e$	$D^+ \to K^+ K^- \pi^+$	128 ± 12	207 ± 15	1.63 ± 0.20
$D^+ \to \bar{K}^0 e^+ \nu_e$	All Tags	2904 ± 55	5561 ± 76	1.92 ± 0.04
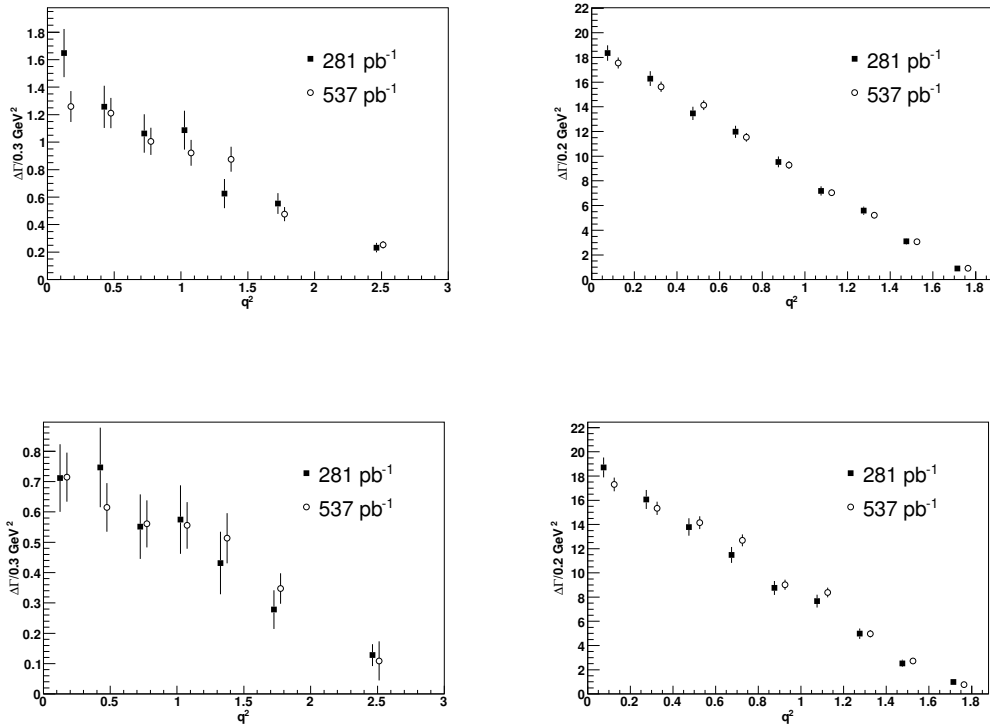
Figure 8.3: The partial rate distributions measured separately in 281 and 537 pb^{-1} of data. The same signal and tagging efficiencies were used in each case. Upper left: $D^0 \to \pi^- e^+ \nu_e$, upper right: $D^0 \to K^- e^+ \nu_e$; lower left: $D^+ \to \pi^0 e^+ \nu_e$; lower right: $D^+ \to \bar{K}^0 e^+ \nu_e$.
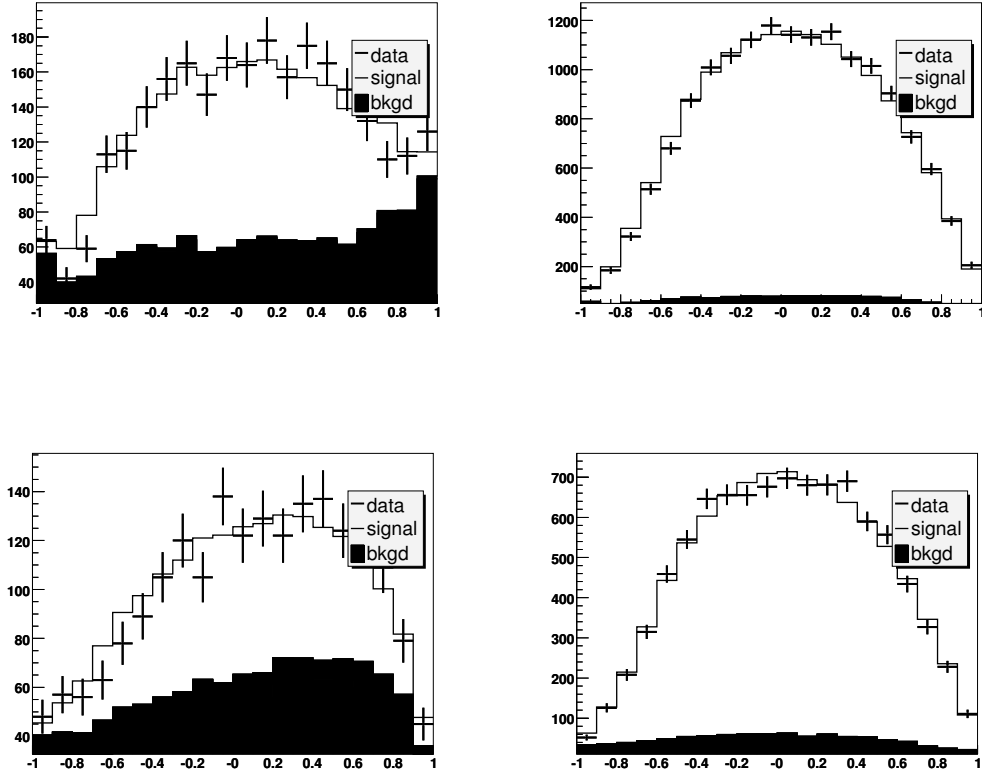
Figure 8.4: Distributions of $\cos\theta_{We}$, the cosine of the angle between the W in the semileptonic D rest frame and the e in the W rest frame, using MC scale factors from the signal U fits. $D^0 \to \pi^- e^+ \nu_e$ is shown in the top left, $D^0 \to K^- e^+ \nu_e$ in the top right, $D^+ \to \pi^0 e^+ \nu_e$ in the bottom left and $D^+ \to \bar{K}^0 e^+ \nu_e$ in the bottom right. The standard $-0.10 < U < 0.24$ GeV cut has been applied
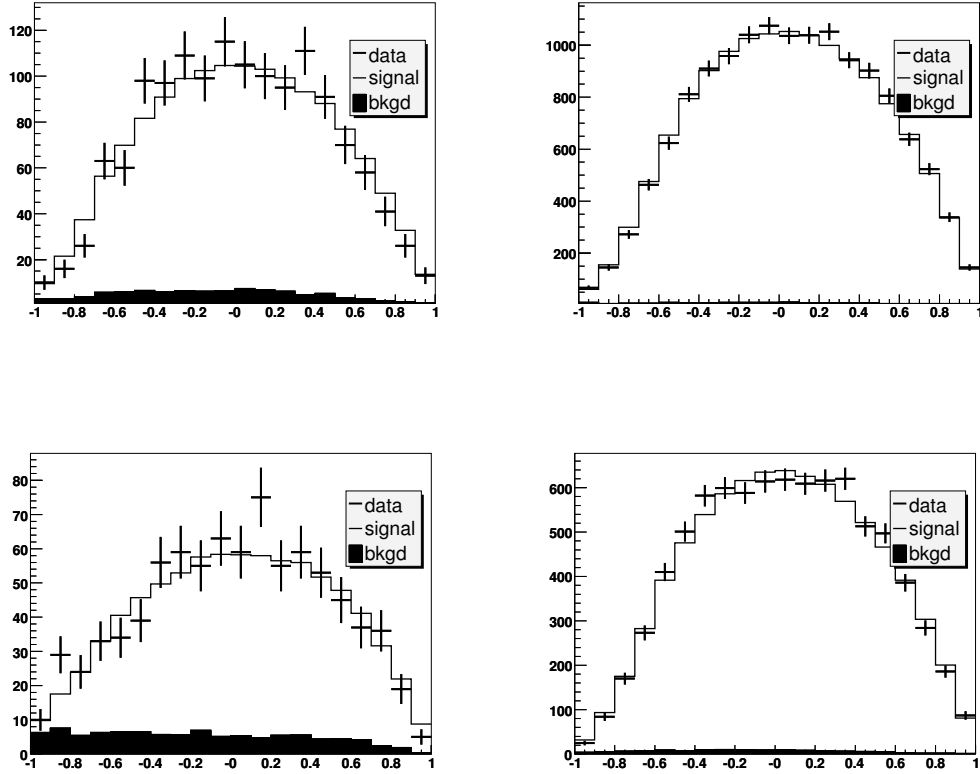
Figure 8.5: Distributions of $\cos\theta_{We}$, the cosine of the angle between the W in the semileptonic D rest frame and the e in the W rest frame, using MC scale factors from the signal U fits. $D^0 \to \pi^- e^+ \nu_e$ is shown in the top left, $D^0 \to K^- e^+ \nu_e$ in the top right, $D^+ \to \pi^0 e^+ \nu_e$ in the bottom left and $D^+ \to \bar{K}^0 e^+ \nu_e$ in the bottom right. A narrow $|U| < 0.06$ GeV cut has been applied.
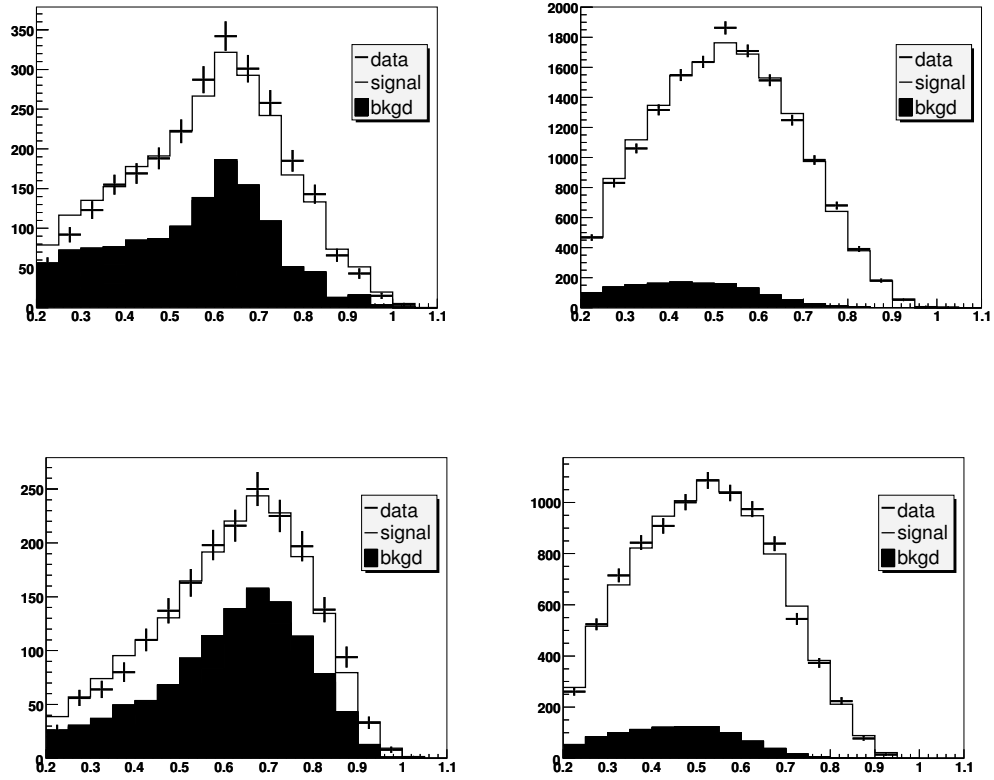
Figure 8.6: Distributions of $|P|_e$, the momentum of the semileptonic electron daughter, using MC scale factors from the signal U fits. $D^0 \rightarrow \pi^- e^+ \nu_e$ is shown in the top left, $D^0 \rightarrow K^- e^+ \nu_e$ in the top right, $D^+ \rightarrow \pi^0 e^+ \nu_e$ in the bottom left and $D^+ \rightarrow \bar{K}^0 e^+ \nu_e$ in the bottom right. The standard $-0.10 < U < 0.24$ GeV cut has been applied
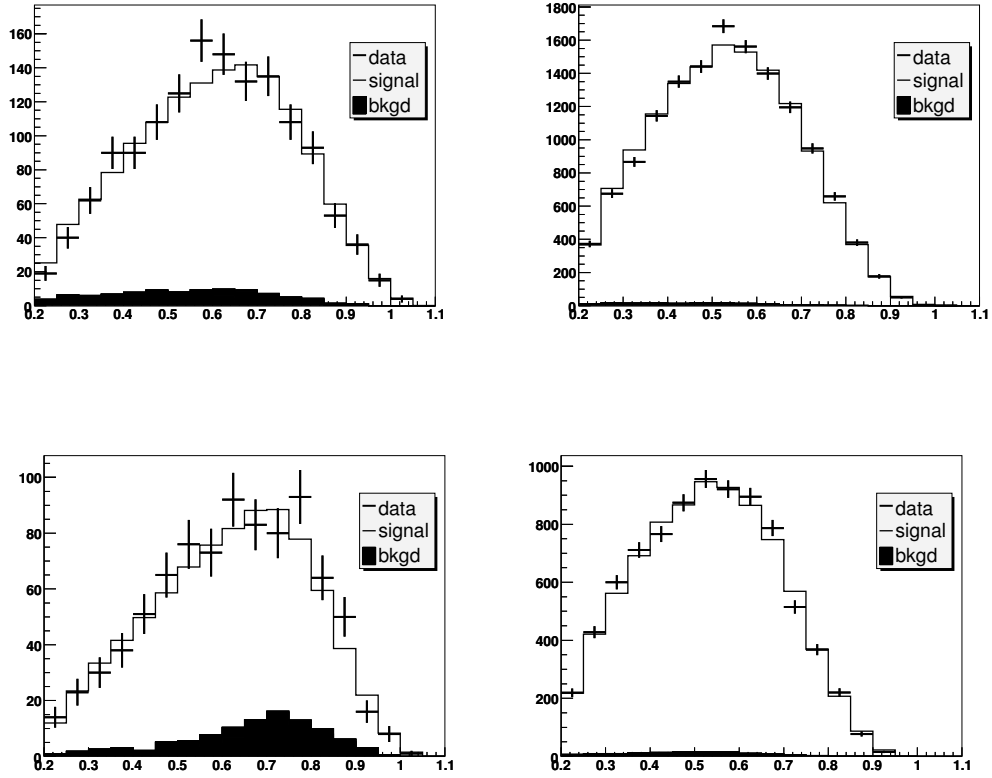
Figure 8.7: Distributions of $|P|_e$, the momentum of the semileptonic electron daughter, using MC scale factors from the signal U fits. $D^0 \to \pi^- e^+ \nu_e$ is shown in the top left, $D^0 \to K^- e^+ \nu_e$ in the top right, $D^+ \to \pi^0 e^+ \nu_e$ in the bottom left and $D^+ \to \bar{K}^0 e^+ \nu_e$ in the bottom right. A narrow $|U| < 0.06$ GeV cut has been applied.
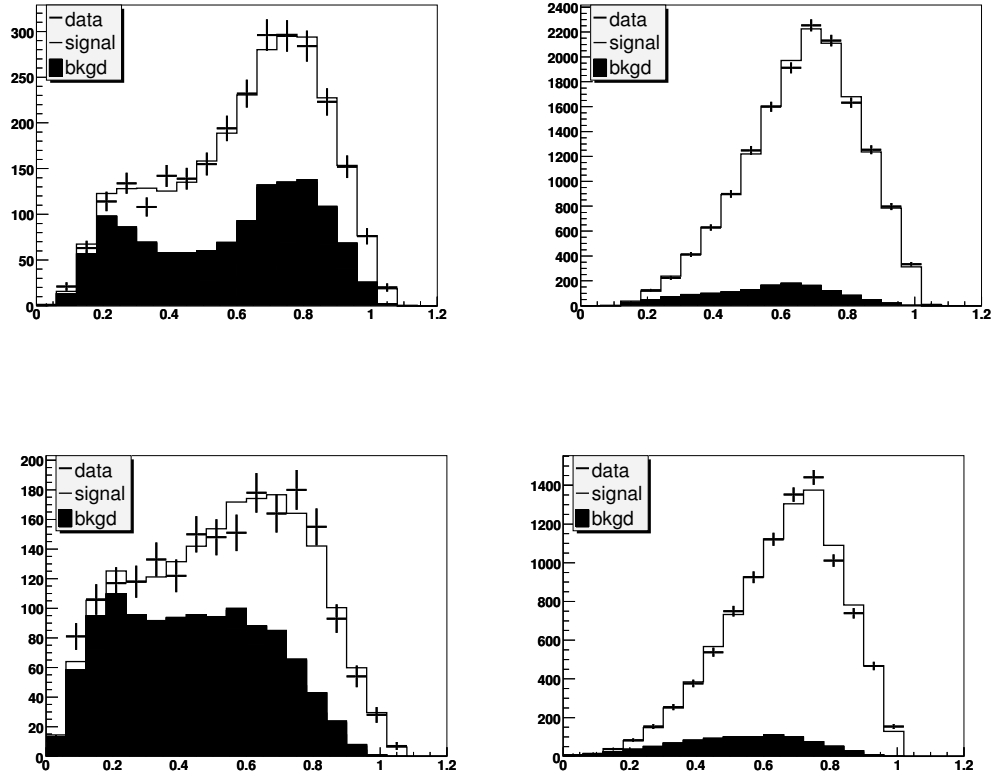
Figure 8.8: Distributions of $|P|_h$, the momentum of the semileptonic hadron daughter, using MC scale factors from the signal U fits. $D^0 \to \pi^- e^+ \nu_e$ is shown in the top left, $D^0 \to K^- e^+ \nu_e$ in the top right, $D^+ \to \pi^0 e^+ \nu_e$ in the bottom left and $D^+ \to \bar{K}^0 e^+ \nu_e$ in the bottom right. The standard $-0.10 < U < 0.24$ GeV cut has been applied
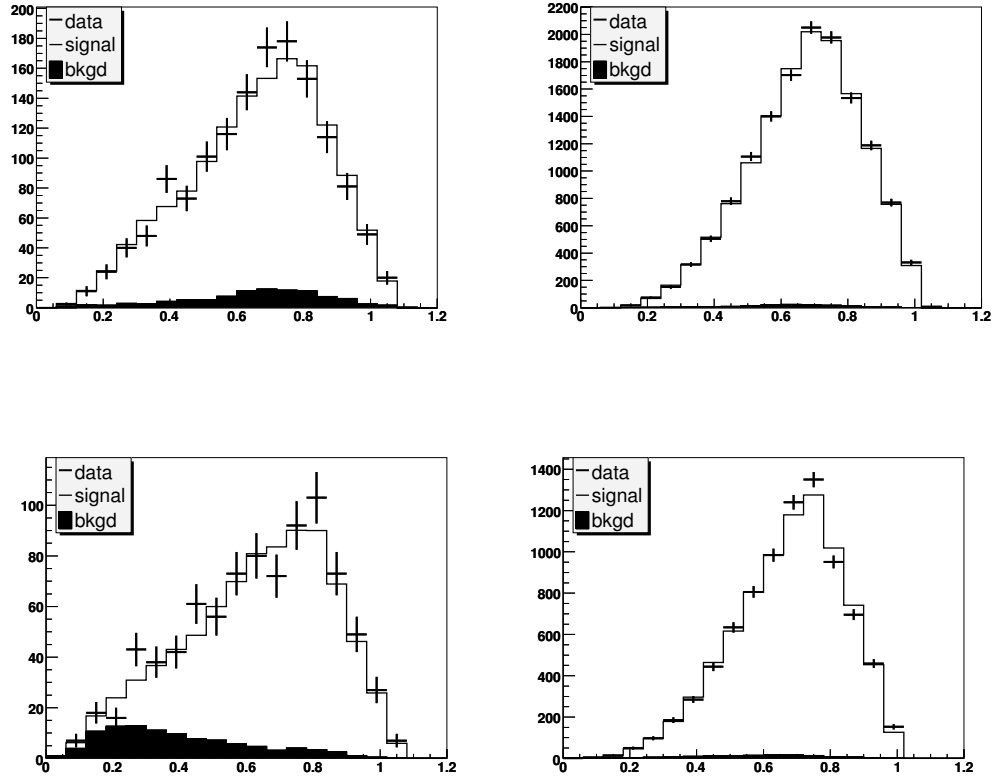
Figure 8.9: Distributions of $|P|_h$, the momentum of the semileptonic hadron daughter, using MC scale factors from the signal U fits. $D^0 \to \pi^- e^+ \nu_e$ is shown in the top left, $D^0 \to K^- e^+ \nu_e$ in the top right, $D^+ \to \pi^0 e^+ \nu_e$ in the bottom left and $D^+ \to \bar{K}^0 e^+ \nu_e$ in the bottom right. A narrow $|U| < 0.06$ GeV cut has been applied.

8.4 Alternate Kinematic Distributions

Signal yields are extracted from distributions of the variable U using signal shapes taken from Monte Carlo. To check the validity of these fits, we have compared data and Monte Carlo in distributions other than U. To produce these plots, we scale signal and background shapes from the Monte Carlo for each q^2 bin and tag mode as they are scaled in the signal yield fits and then sum over all q^2 bins and tag modes. Like the shapes used in the signal fits, these distributions are corrected for biases in electron, π^0 and charged hadron ID. In each case we provide two versions of the plots: one using the standard (-0.1,0.24) GeV U range and another using a tighter (-0.06,0.06) GeV U range. While the first version provides an estimate of data/MC agreement including backgrounds, the majority of backgrounds have been eliminated in the second version. We provide distributions of three variables. Figures 8.4 and 8.5 show the cosine of the angle between the virtual W (in the rest frame of the semileptonic D) and the e (in the rest frame of the W). Figures 8.6 and 8.7 show the electron momentum (including recovered bremsstrahlung showers) and Figures 8.8 and 8.9 show the meson momentum. In all cases, we find the agreement between data and Monte Carlo to be acceptable.

CHAPTER 9

CONCLUSION

We have measured partial semileptonic rates for the decays $D^0 \rightarrow \pi^- e^+ \nu_e$, $D^0 \rightarrow K^- e^+ \nu_e$, $D^+ \rightarrow \pi^0 e^+ \nu_e$ and $D^+ \rightarrow \bar{K}^0 e^+ \nu_e$. Using these partial rates, we have extracted branching fractions, the CKM parameters $|V_{cd}|$ and $|V_{cs}|$ and form factor shape parameters using several parameterizations. The branching fraction measurements are by far the most precise to date, as are nearly all of the form factor measurments. The later are significantly more precise than the best available theoretical predictions and, in particular, provide excellent goals for future LQCD form factor studies.

APPENDIX
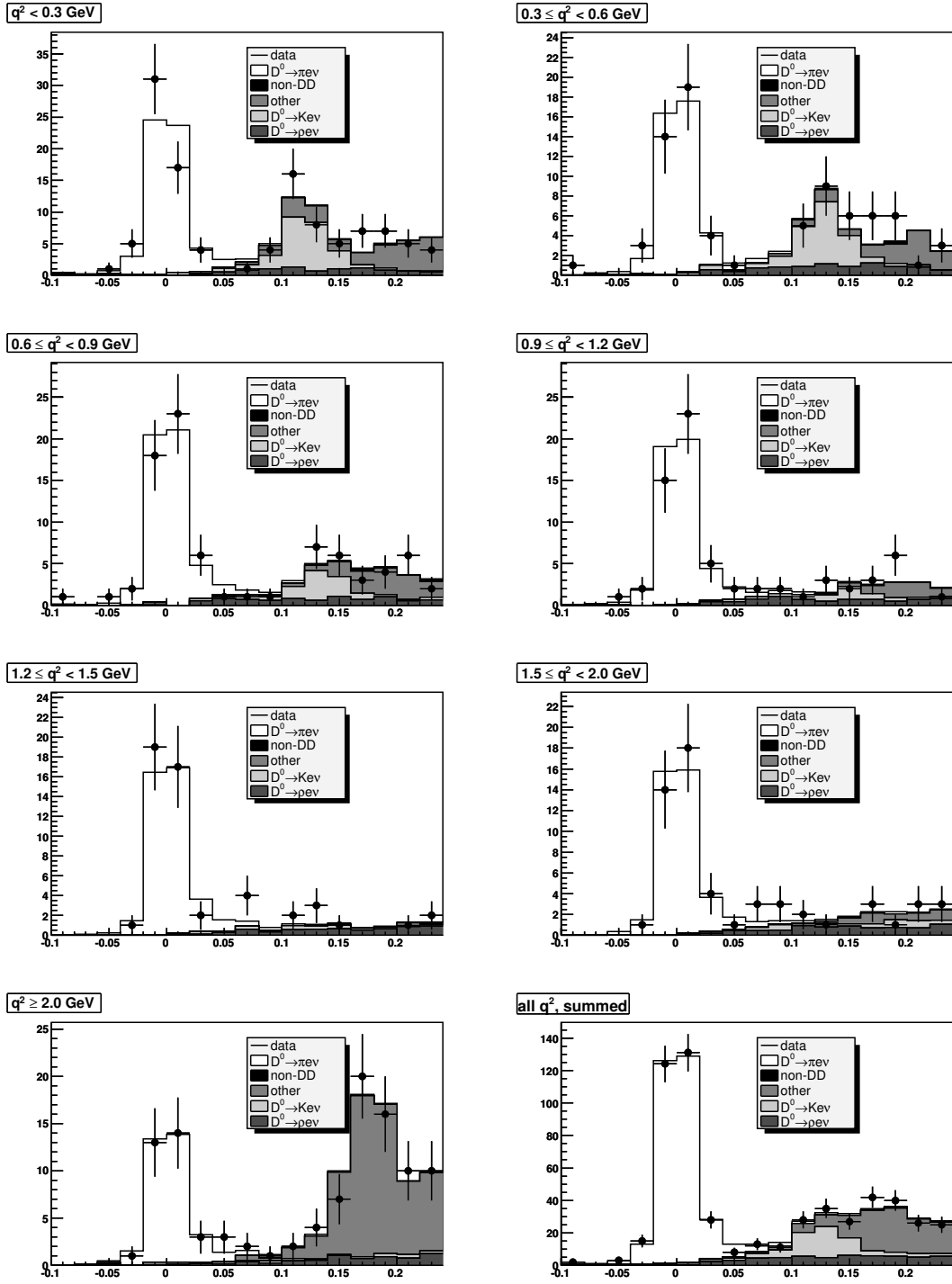
Figure 1: Signal yield fits $D^0 \to \pi^- e^+ \nu_e$ candidates opposite $\bar{D}^0 \to K^+ \pi^-$ tags in data. The q^2 bin increases from left to right and down the page. The lower right-hand plot shows the sum of all q^2 bins.

112
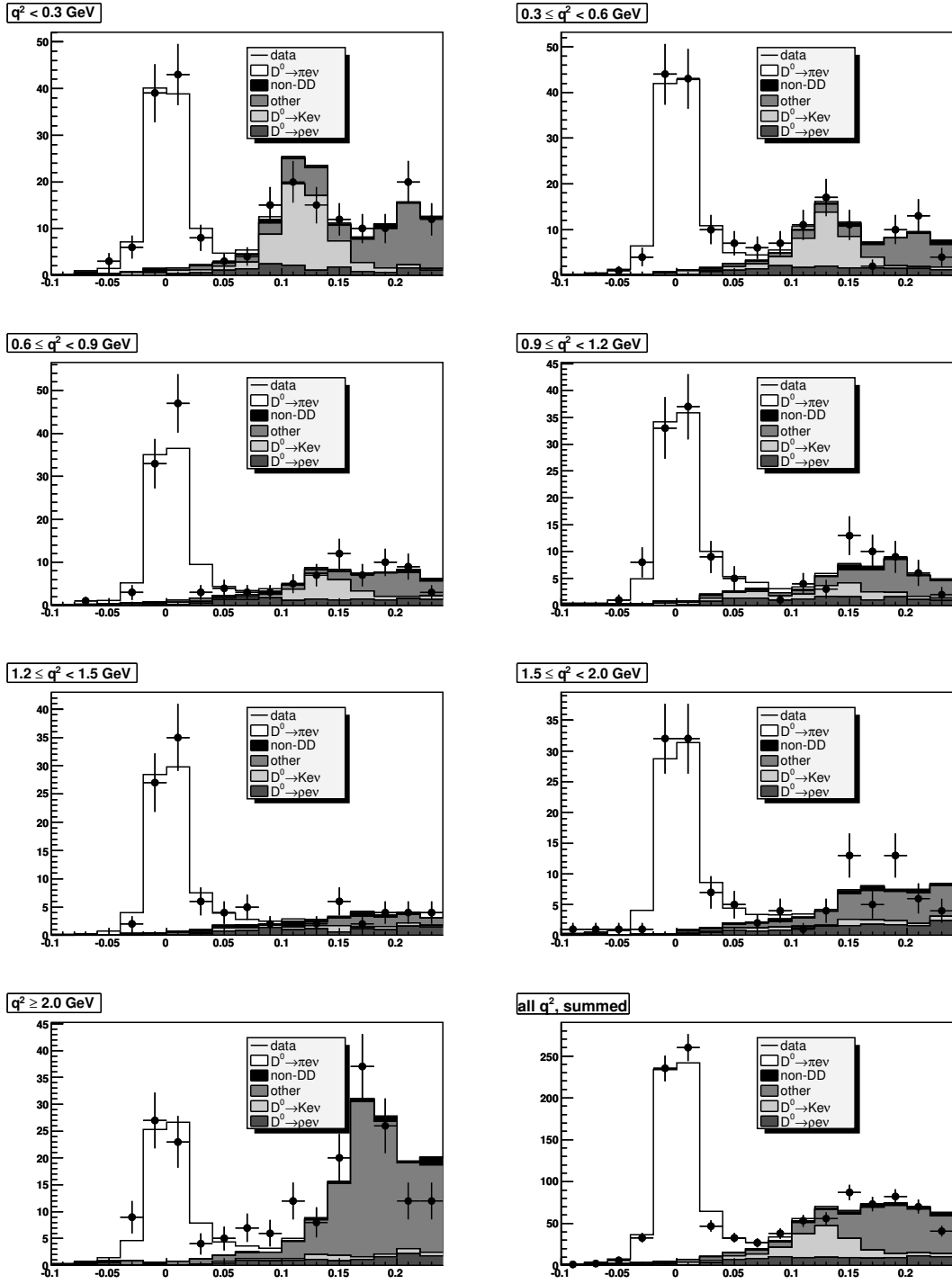
Figure 2: Signal yield fits to $D^0 \rightarrow \pi^- e^+ \nu_e$ candidates opposite $\bar{D}^0 \rightarrow K^+ \pi^- \pi^0$ tags in data. The q^2 bin increases from left to right and down the page. The lower right-hand plot shows the sum of all q^2 bins.
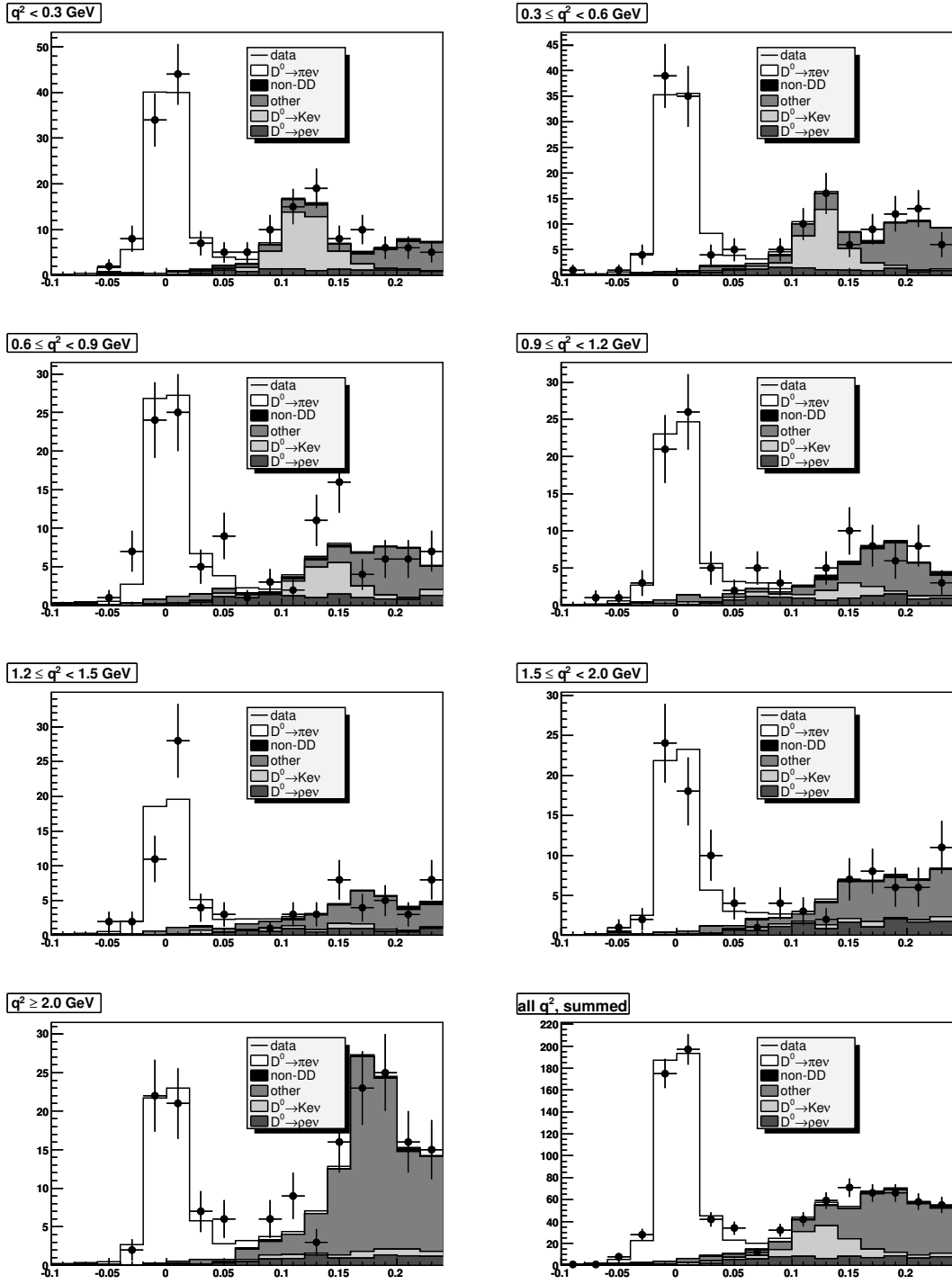
Figure 3: Signal yield fits to $D^0 \rightarrow \pi^- e^+ \nu_e$ candidates opposite $\bar{D}^0 \rightarrow K^+\pi^-\pi^-\pi^+$ tags in data. The q^2 bin increases from left to right and down the page. The lower right-hand plot shows the sum of all q^2 bins.
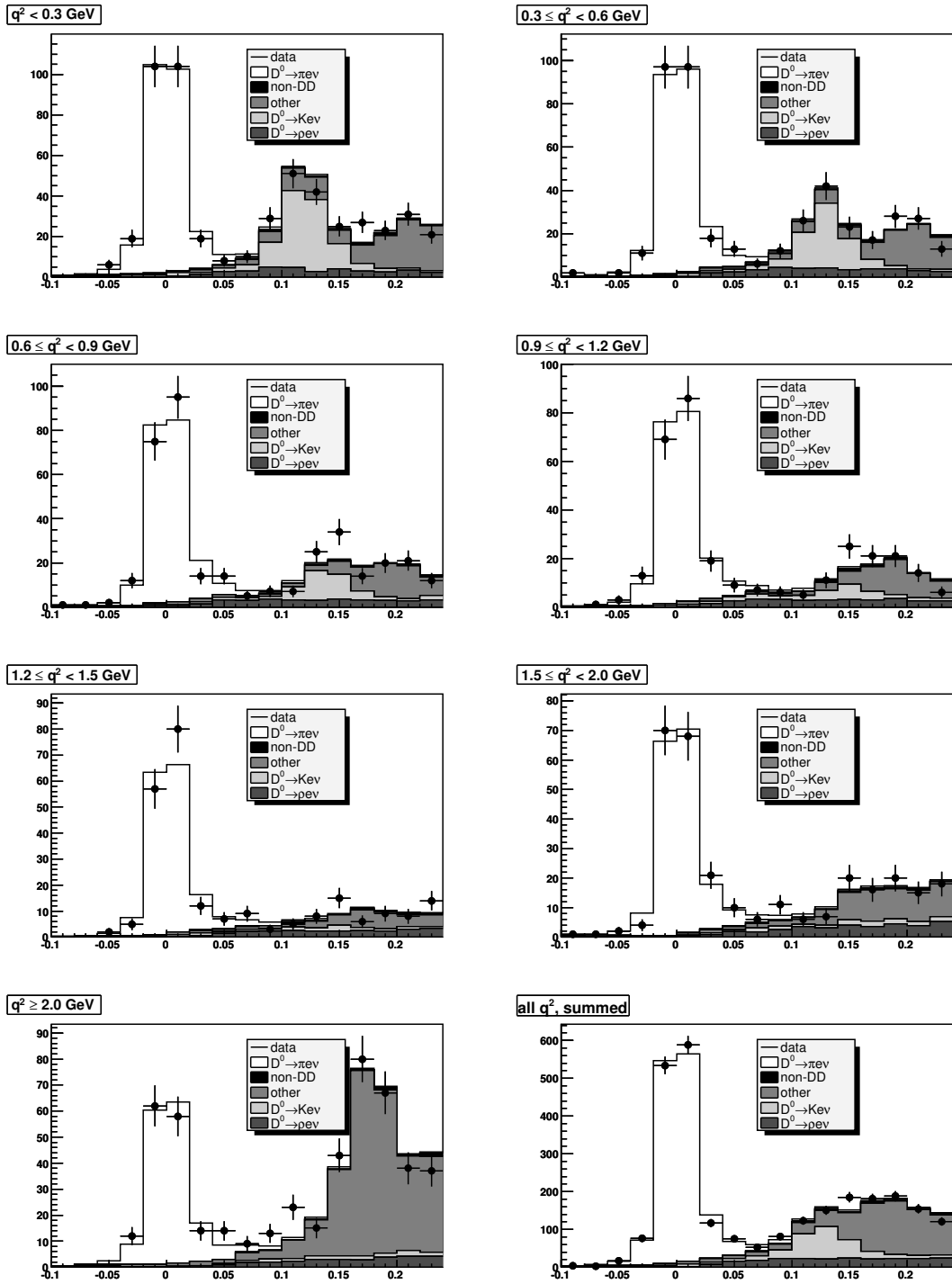
Figure 4: Signal yield fits to $D^0 \to \pi^- e^+ \nu_e$ candidates opposite all tag mode in data. The q^2 bin increases from left to right and down the page. The lower right-hand plot shows the sum of all q^2 bins.

115
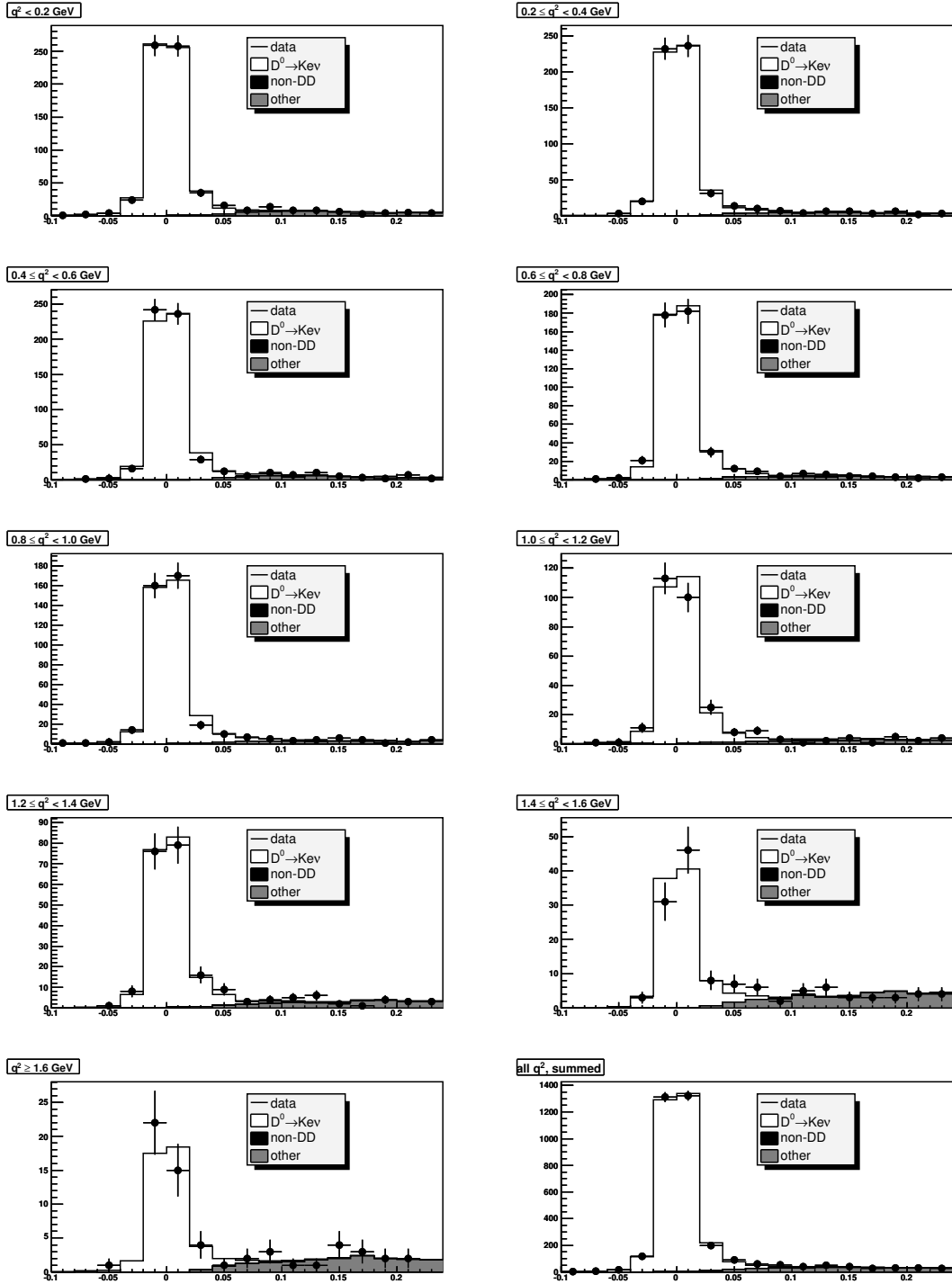
Figure 5: Signal yield fits to $D^0 \rightarrow K^- e^+ \nu_e$ candidates opposite $\bar{D}^0 \rightarrow K^+ \pi^-$ tags in data. The q^2 bin increases from left to right and down the page. The lower right-hand plot shows the sum of all q^2 bins.
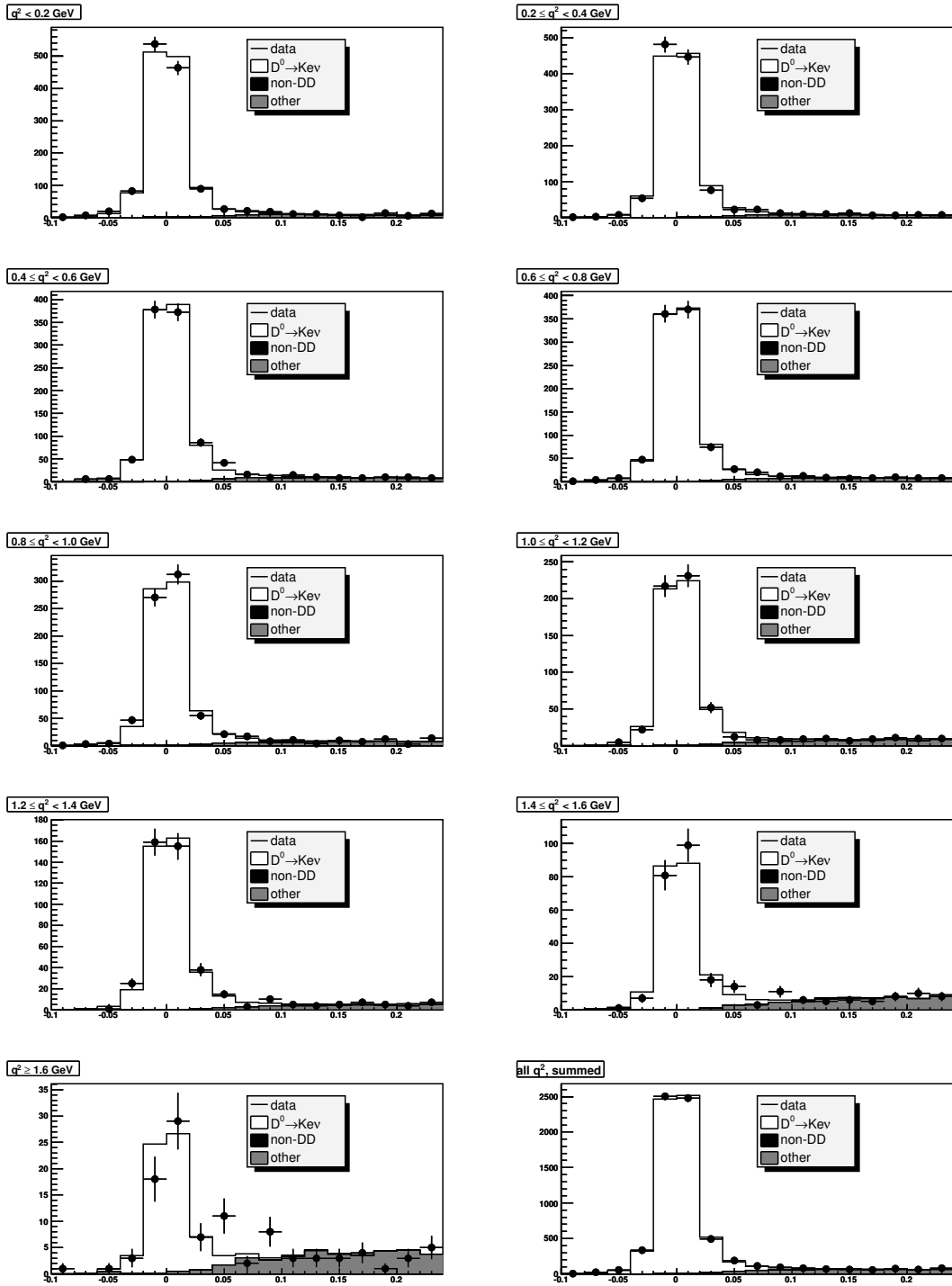
Figure 6: Signal yield fits to $D^0 \rightarrow K^- e^+ \nu_e$ candidates opposite $\bar{D}^0 \rightarrow K^+ \pi^- \pi^0$ tags in data. The q^2 bin increases from left to right and down the page. The lower right-hand plot shows the sum of all q^2 bins.
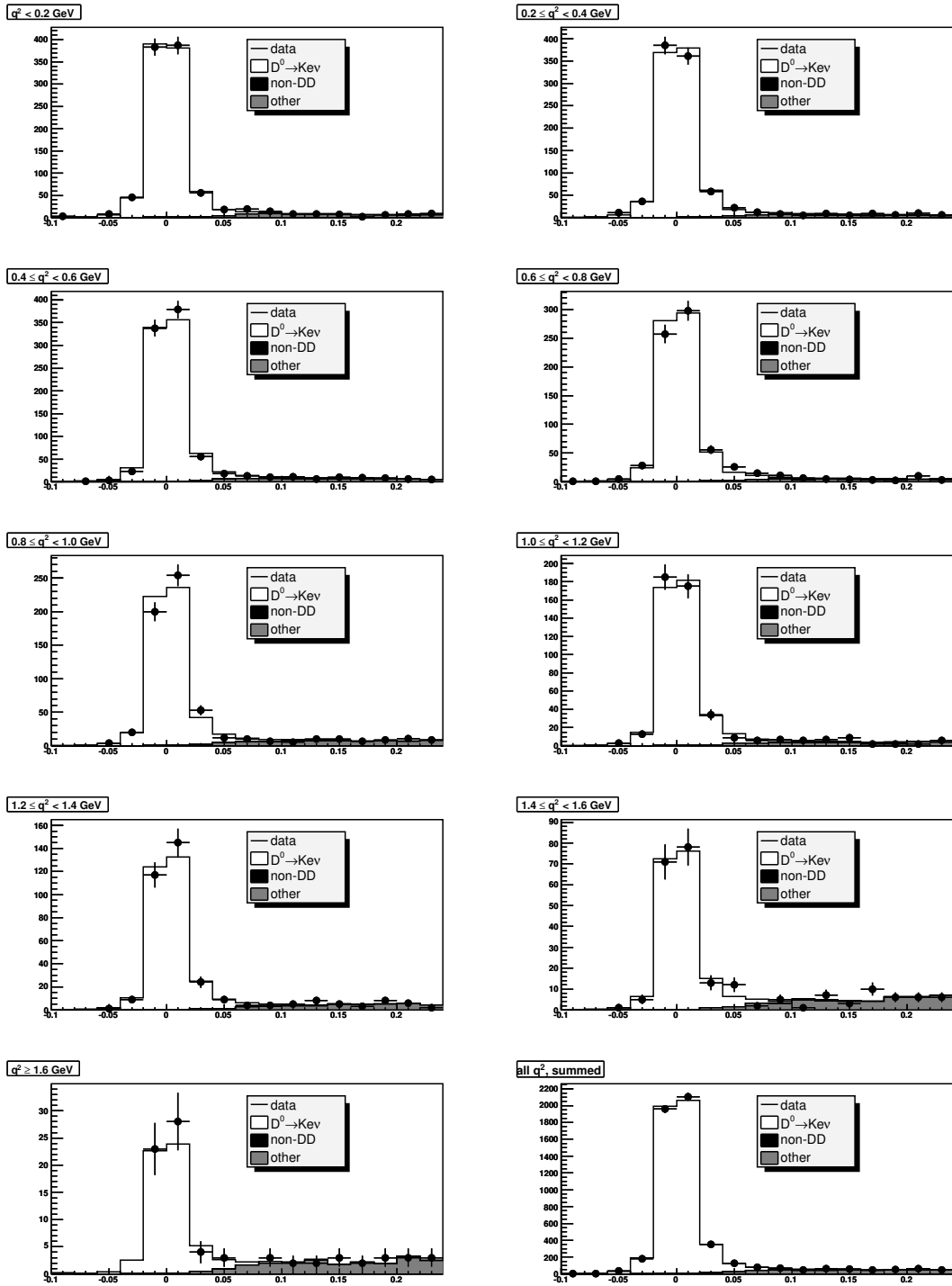
Figure 7: Signal yield fits to $D^0 \to K^- e^+ \nu_e$ candidates opposite $\bar{D}^0 \to K^+ \pi^- \pi^- \pi^+$ tags in data. The q^2 bin increases from left to right and down the page. The lower right-hand plot shows the sum of all q^2 bins.

118
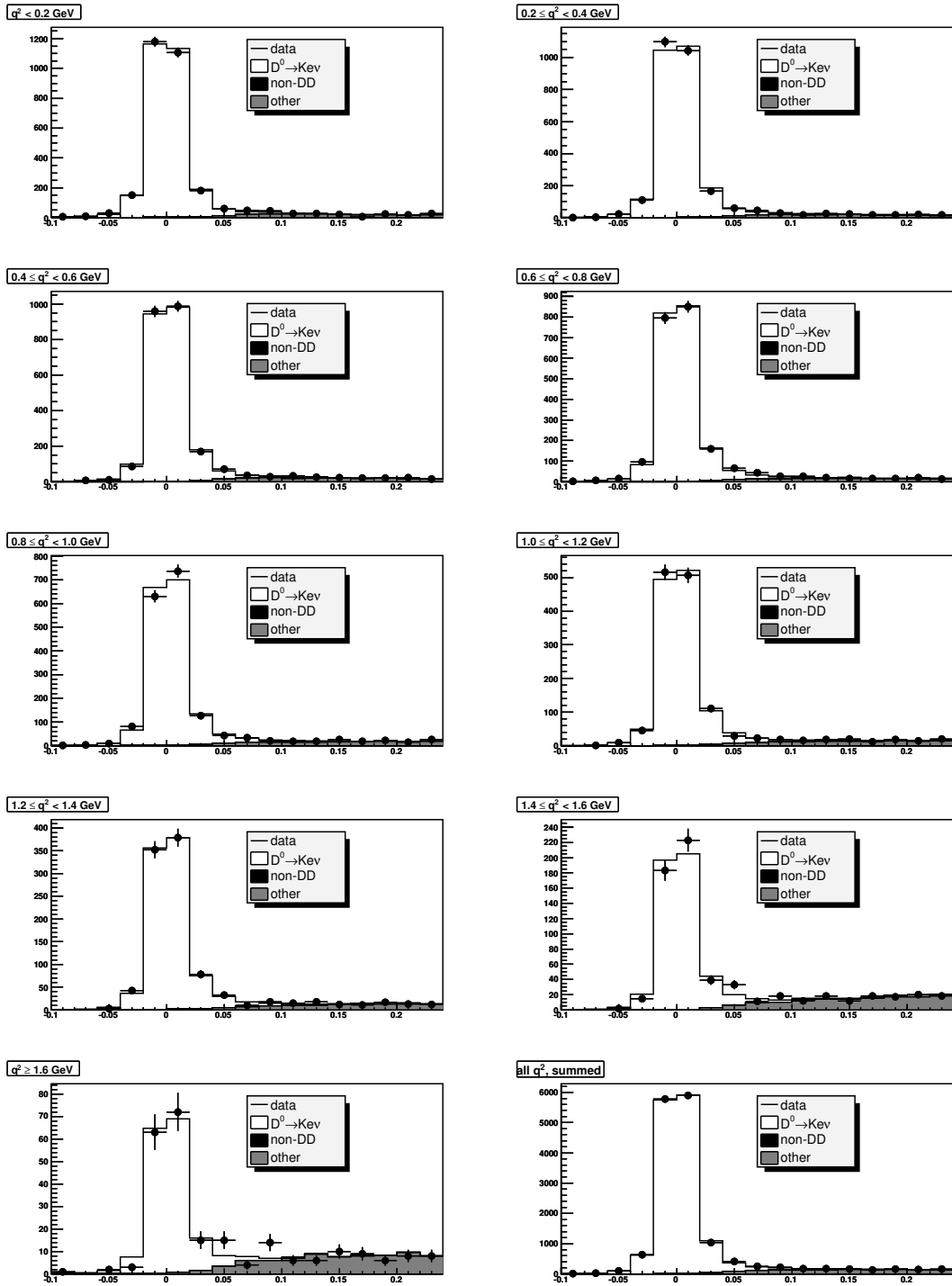
Figure 8: Signal yield fits to $D^0 \to K^- e^+ \nu_e$ candidates opposite all tags modes in data. The q^2 bin increases from left to right and down the page. The lower right-hand plot shows the sum of all q^2 bins.
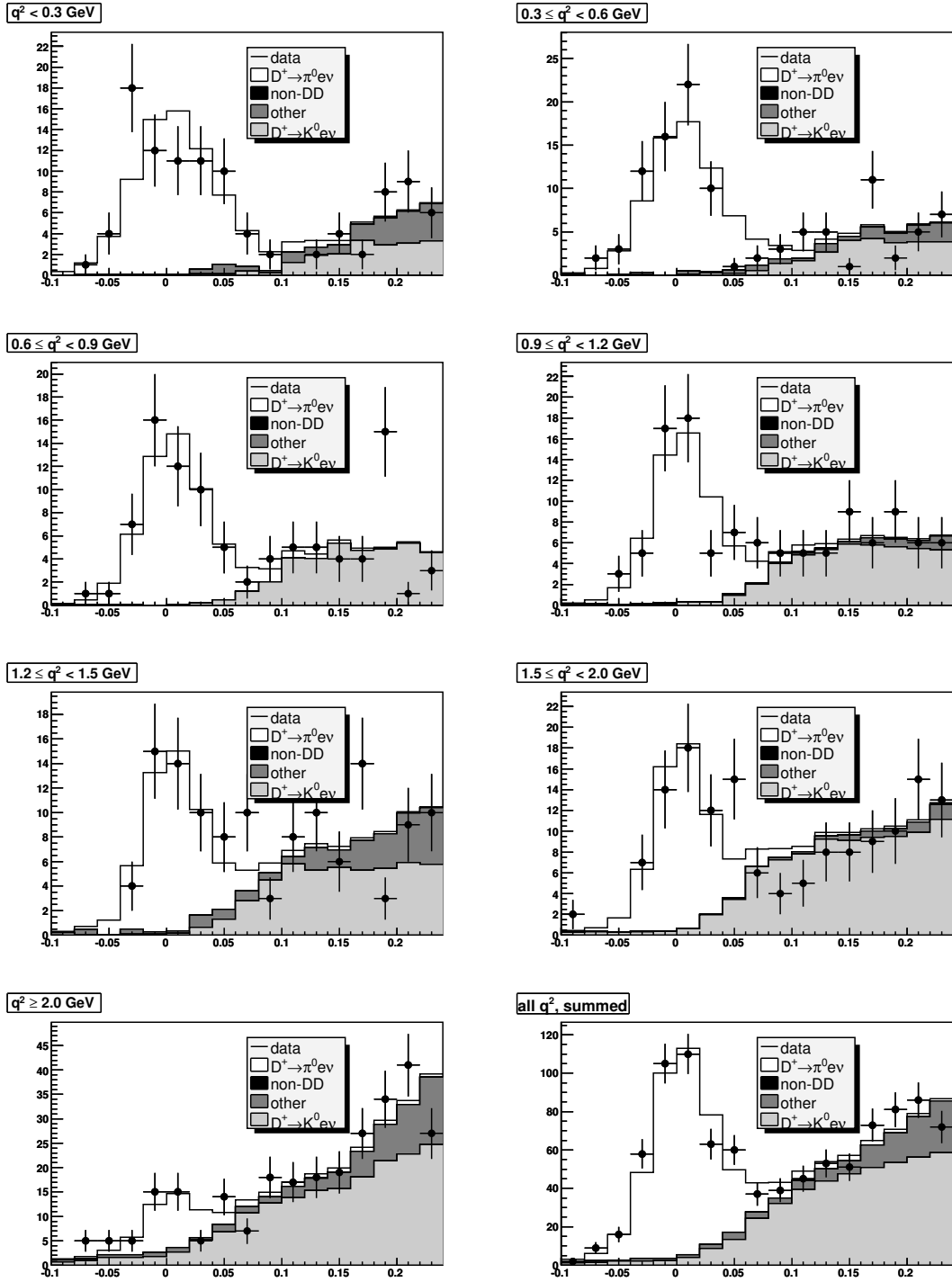
Figure 9: Signal yield fits to $D^+ \rightarrow \pi^0 e^+ \nu_e$ candidates opposite $D^- \rightarrow K^+ \pi^- \pi^-$ tags in data. The q^2 bin increases from left to right and down the page. The lower right-hand plot shows the sum of all q^2 bins.
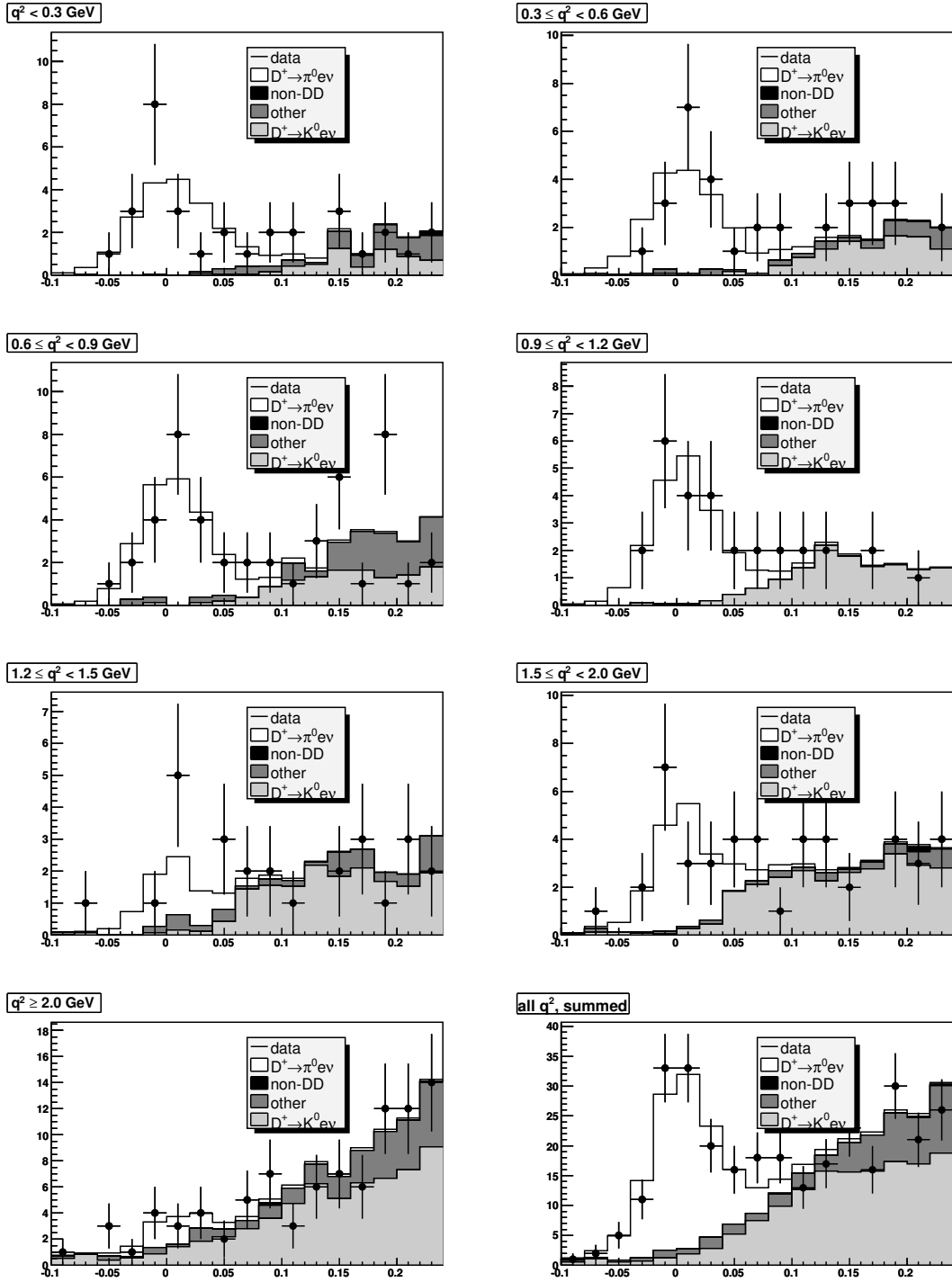
Figure 10: Signal yield fits to $D^+ \to \pi^0 e^+ \nu_e$ candidates opposite $D^- \to K^+\pi^-\pi^-\pi^0$ tags in data. The q^2 bin increases from left to right and down the page. The lower right-hand plot shows the sum of all q^2 bins.

121
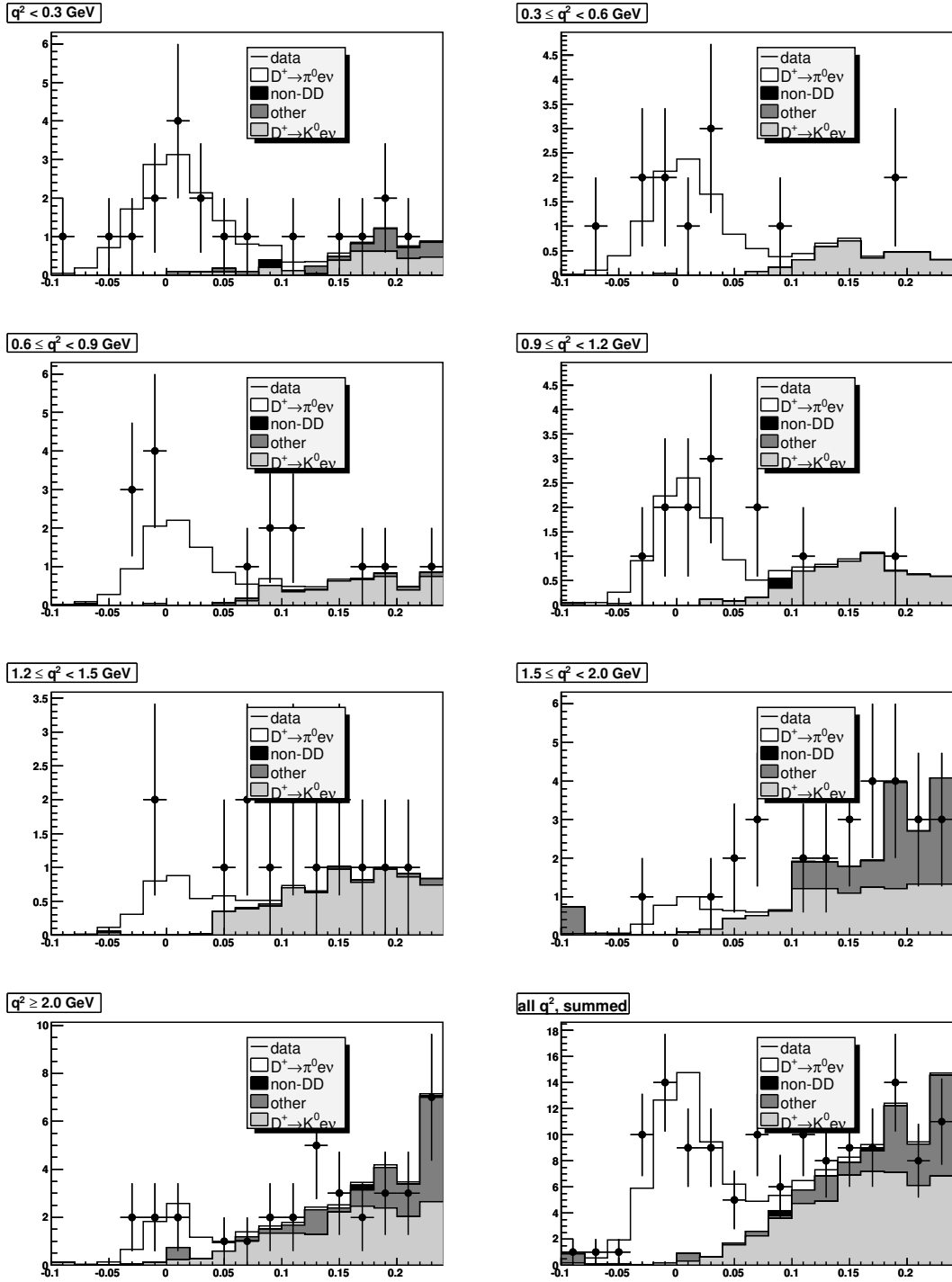
Figure 11: Signal yield fits to $D^+ \to \pi^0 e^+ \nu_e$ candidates opposite $D^- \to K^0 \pi^-$ tags in data. The q^2 bin increases from left to right and down the page. The lower right-hand plot shows the sum of all q^2 bins.
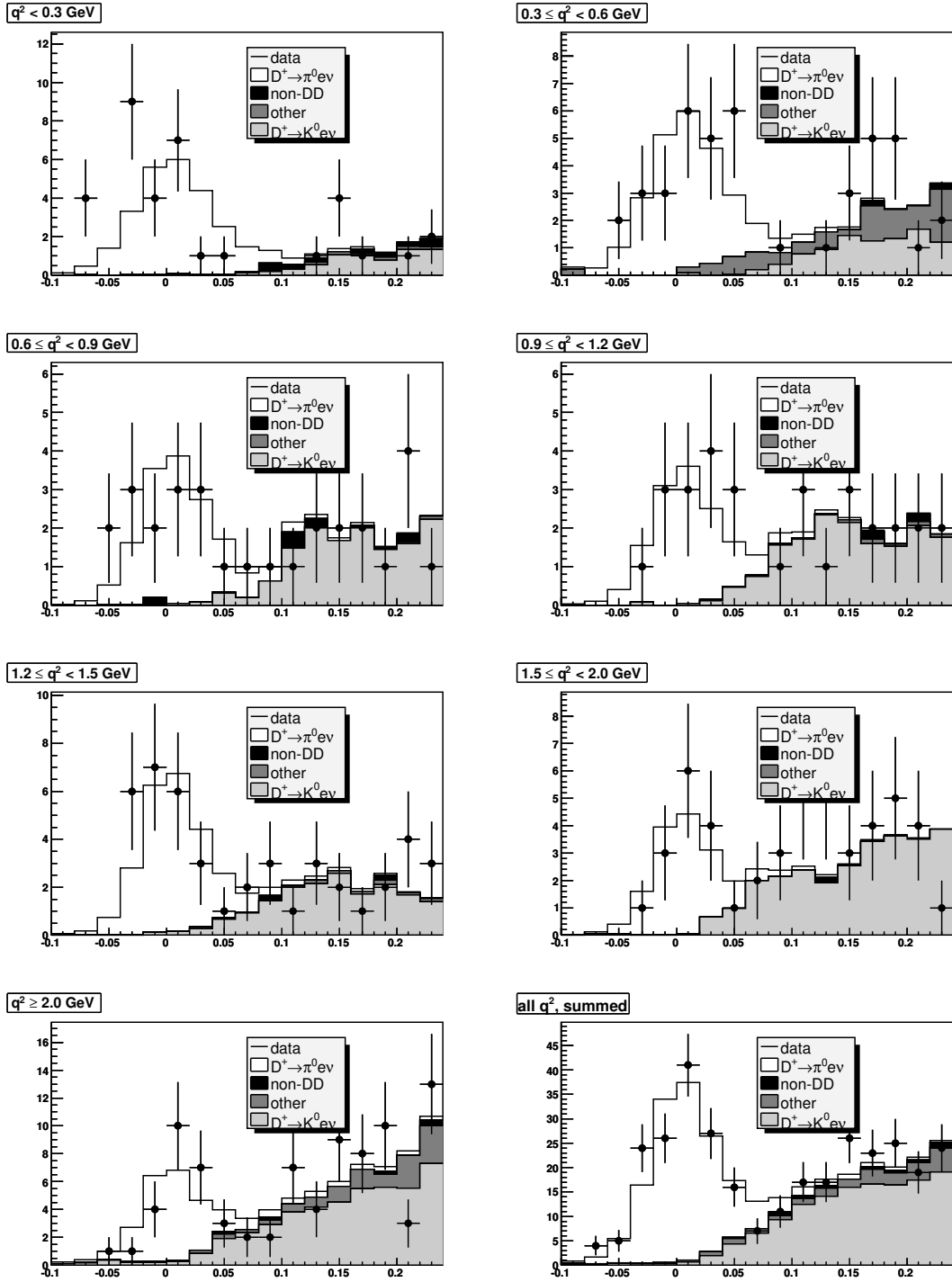
Figure 12: Signal yield fits to $D^+ \to \pi^0 e^+ \nu_e$ candidates opposite $D^- \to K^0 \pi^- \pi^0$ tags in data. The q^2 bin increases from left to right and down the page. The lower right-hand plot shows the sum of all q^2 bins.
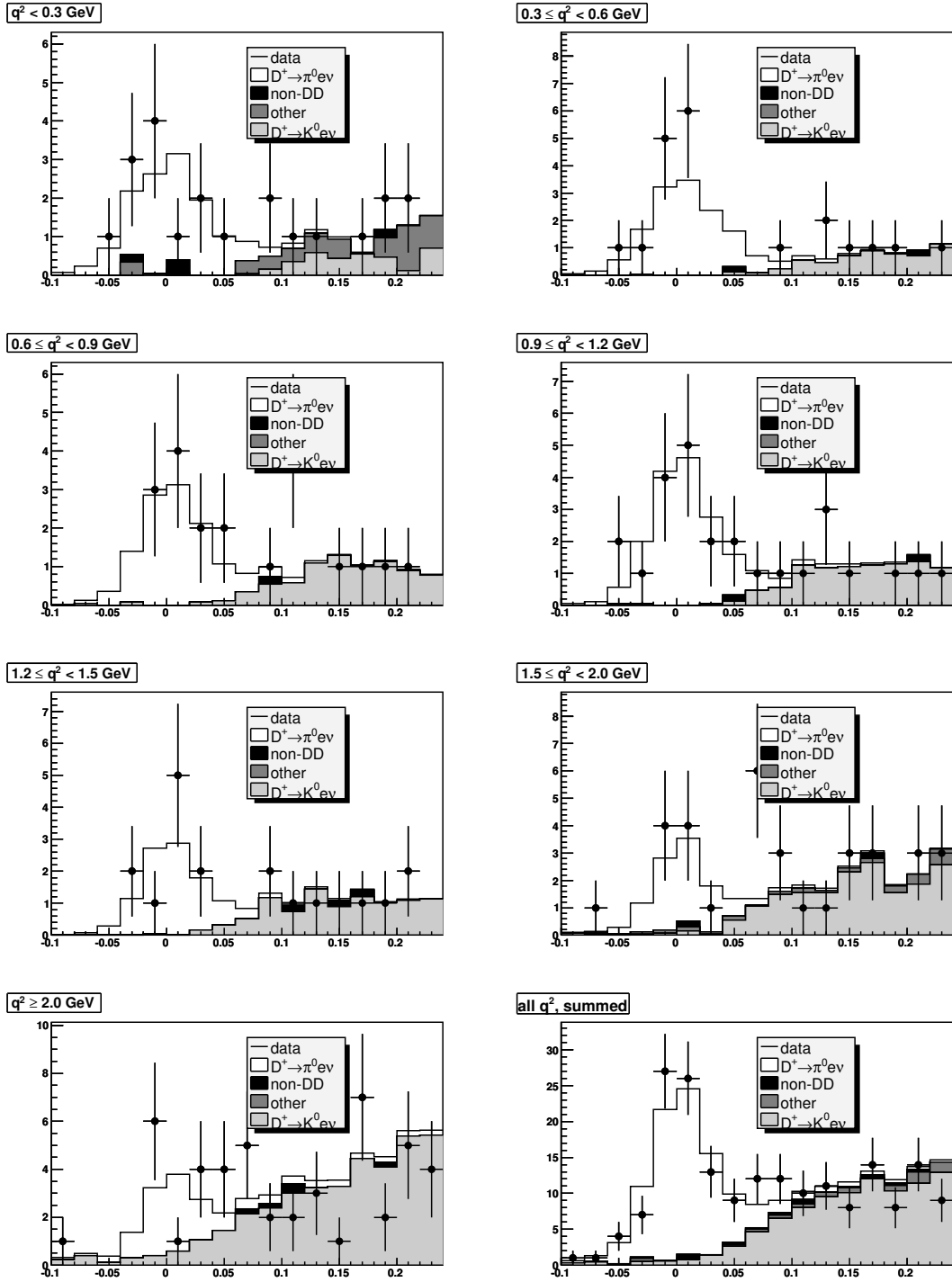
Figure 13: Signal yield fits to $D^+ \to \pi^0 e^+ \nu_e$ candidates opposite $D^- \to K^0 \pi^- \pi^- \pi^+$ tags in data. The q^2 bin increases from left to right and down the page. The lower right-hand plot shows the sum of all q^2 bins.

124
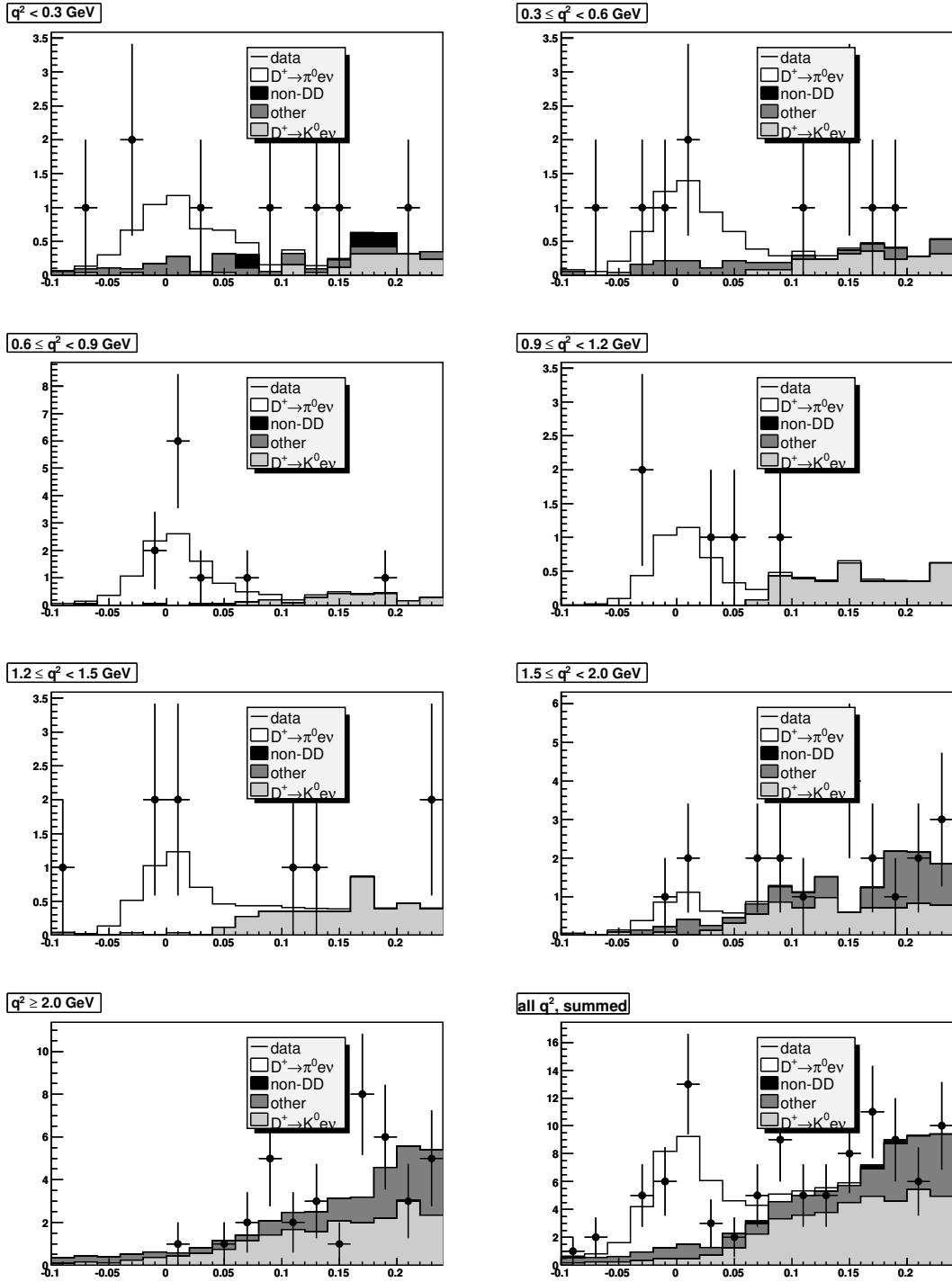
Figure 14: Signal yield fits to $D^+ \to \pi^0 e^+ \nu_e$ candidates opposite $D^- \to K^+\pi^-\pi^-$ tags in data. The q^2 bin increases from left to right and down the page. The lower right-hand plot shows the sum of all q^2 bins.

125
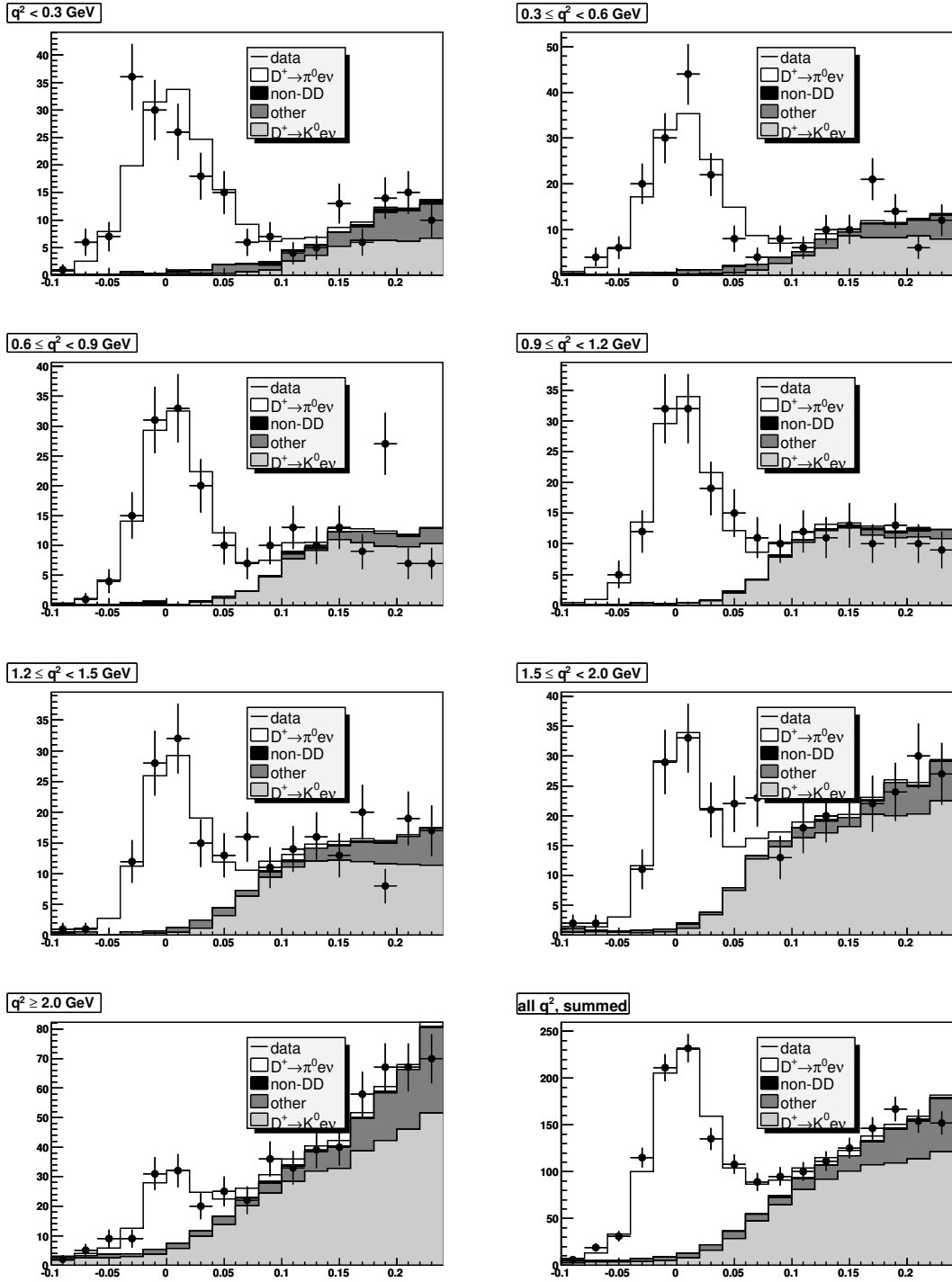
Figure 15: Signal yield fits to $D^+ \to \pi^0 e^+ \nu_e$ candidates opposite all tag modes in data. The q^2 bin increases from left to right and down the page. The lower right-hand plot shows the sum of all q^2 bins.

126
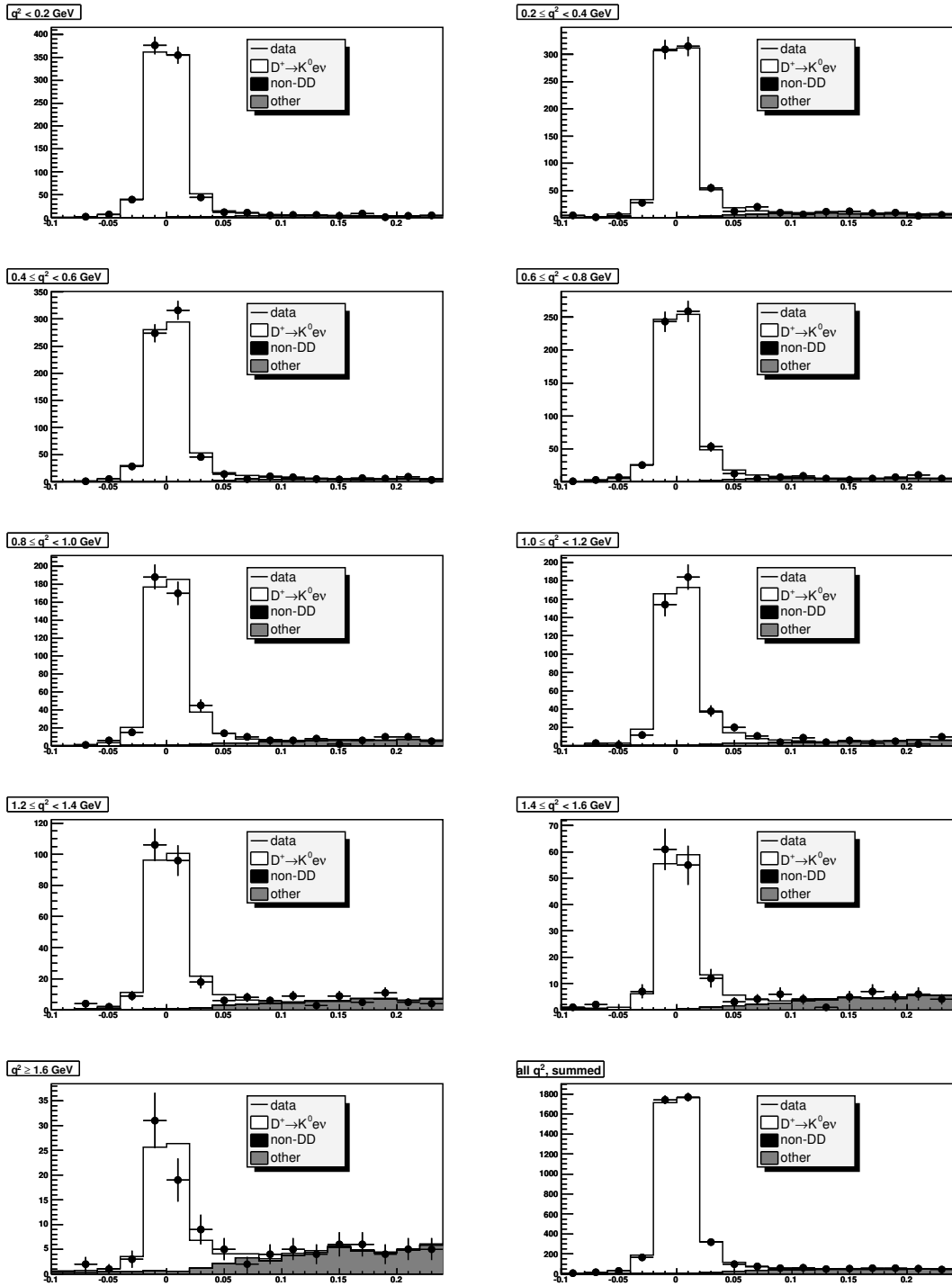
Figure 16: Signal yield fits to $D^+ \rightarrow \bar{K}^0 e^+ \nu_e$ candidates opposite $D^- \rightarrow K^+ \pi^- \pi^-$ tags in data. The q^2 bin increases from left to right and down the page. The lower right-hand plot shows the sum of all q^2 bins.
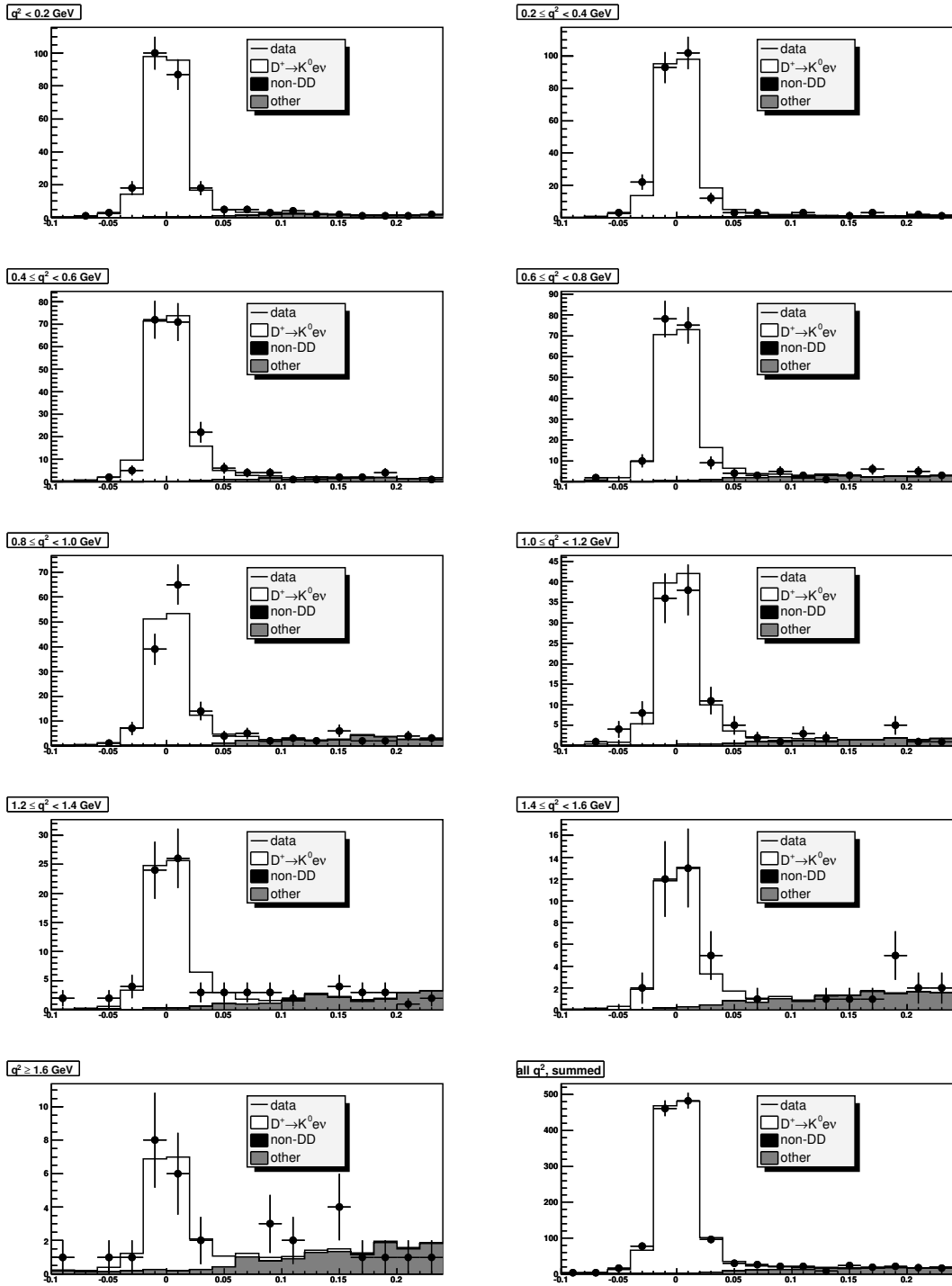
Figure 17: Signal yield fits to $D^+ \rightarrow \bar{K}^0 e^+ \nu_e$ candidates opposite $D^- \rightarrow K^+\pi^-\pi^-\pi^0$ tags in data. The q^2 bin increases from left to right and down the page. The lower right-hand plot shows the sum of all q^2 bins.

128
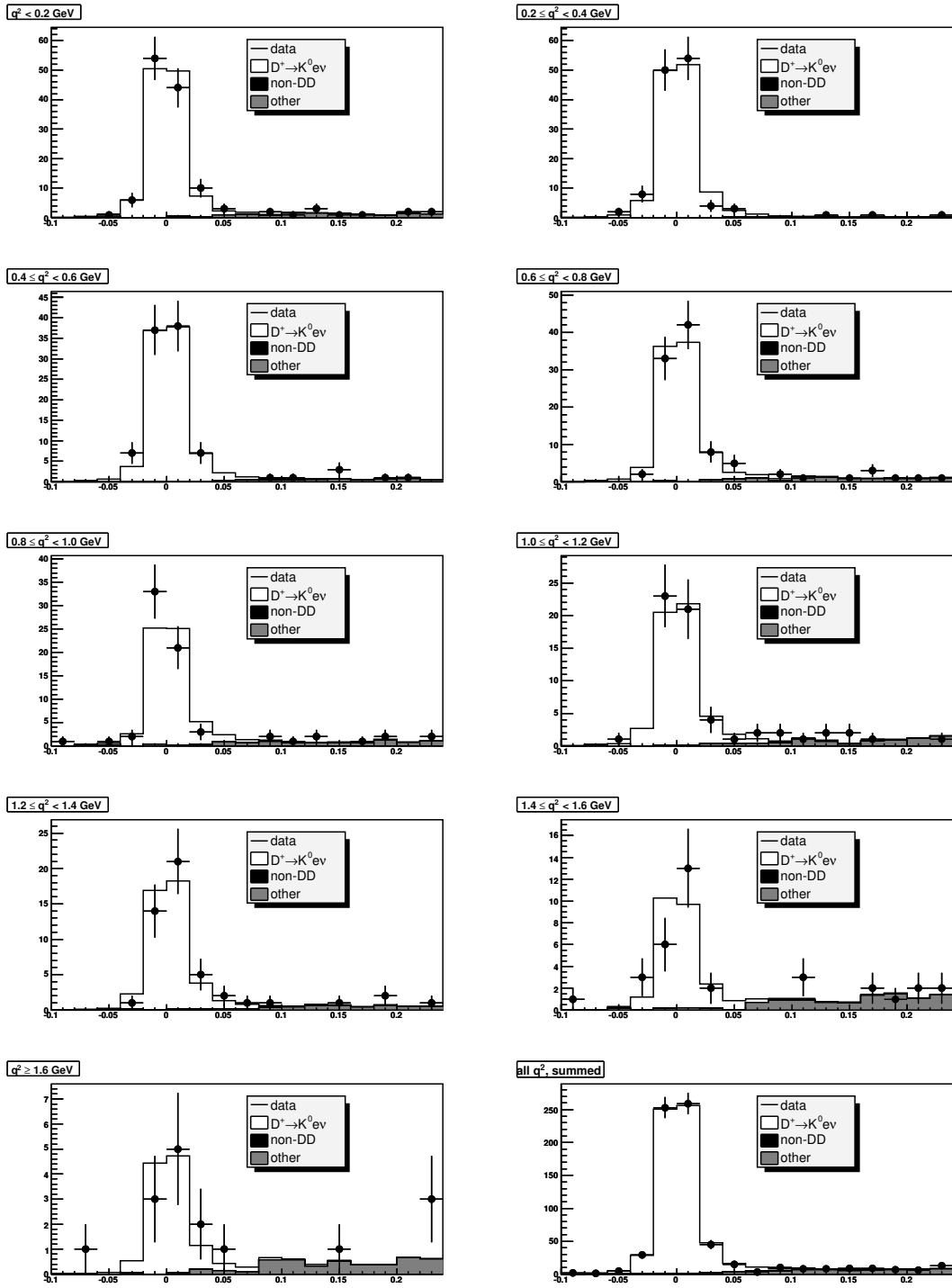
Figure 18: Signal yield fits to $D^+ \to \bar{K}^0 e^+ \nu_e$ candidates opposite $D^- \to K^0\pi^-$ tags in data. The q^2 bin increases from left to right and down the page. The lower right-hand plot shows the sum of all q^2 bins.
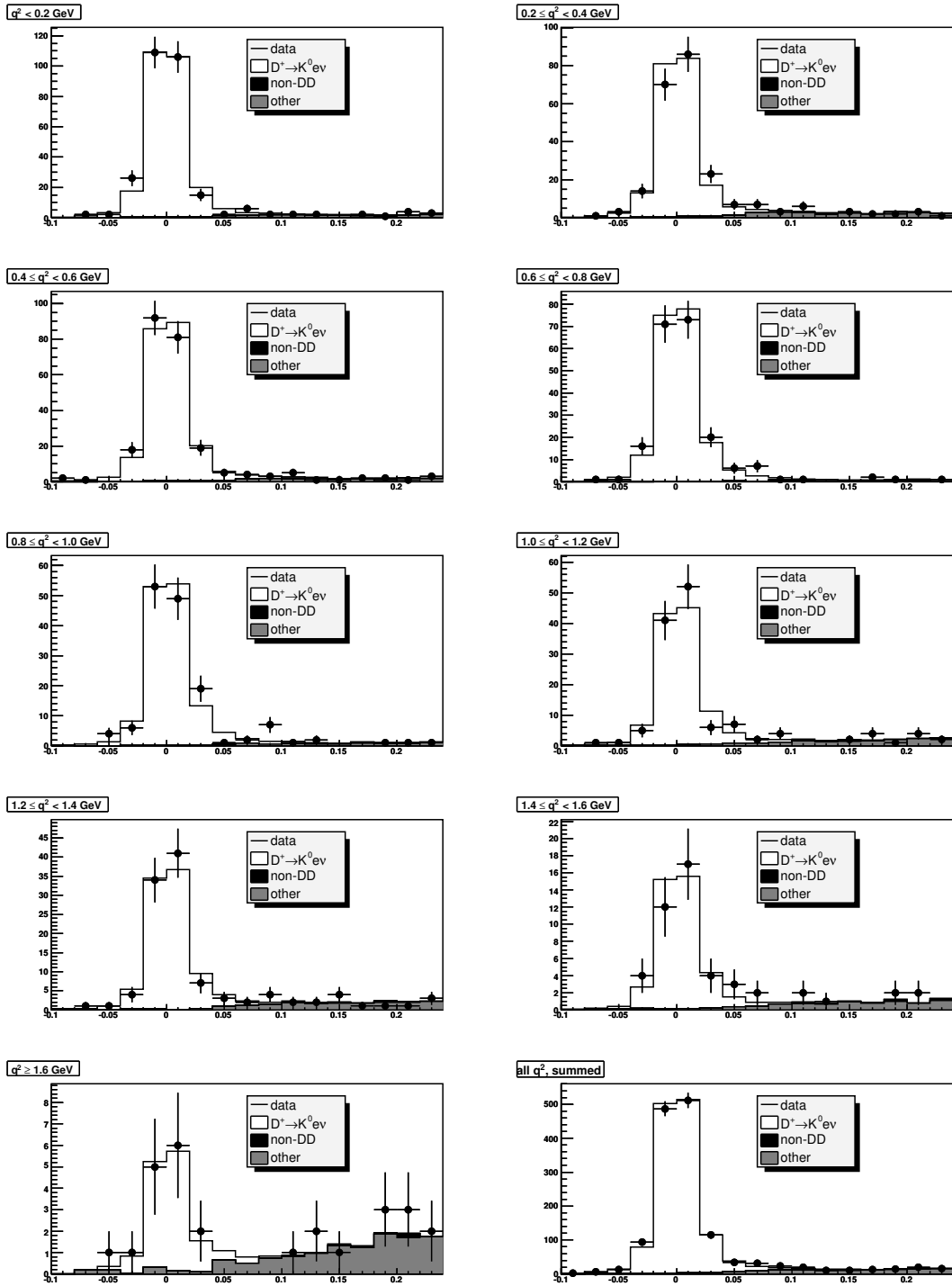
Figure 19: Signal yield fits to $D^+ \rightarrow \bar{K}^0 e^+ \nu_e$ candidates opposite $D^- \rightarrow K^0 \pi^- \pi^0$ tags in data. The q^2 bin increases from left to right and down the page. The lower right-hand plot shows the sum of all q^2 bins.

130
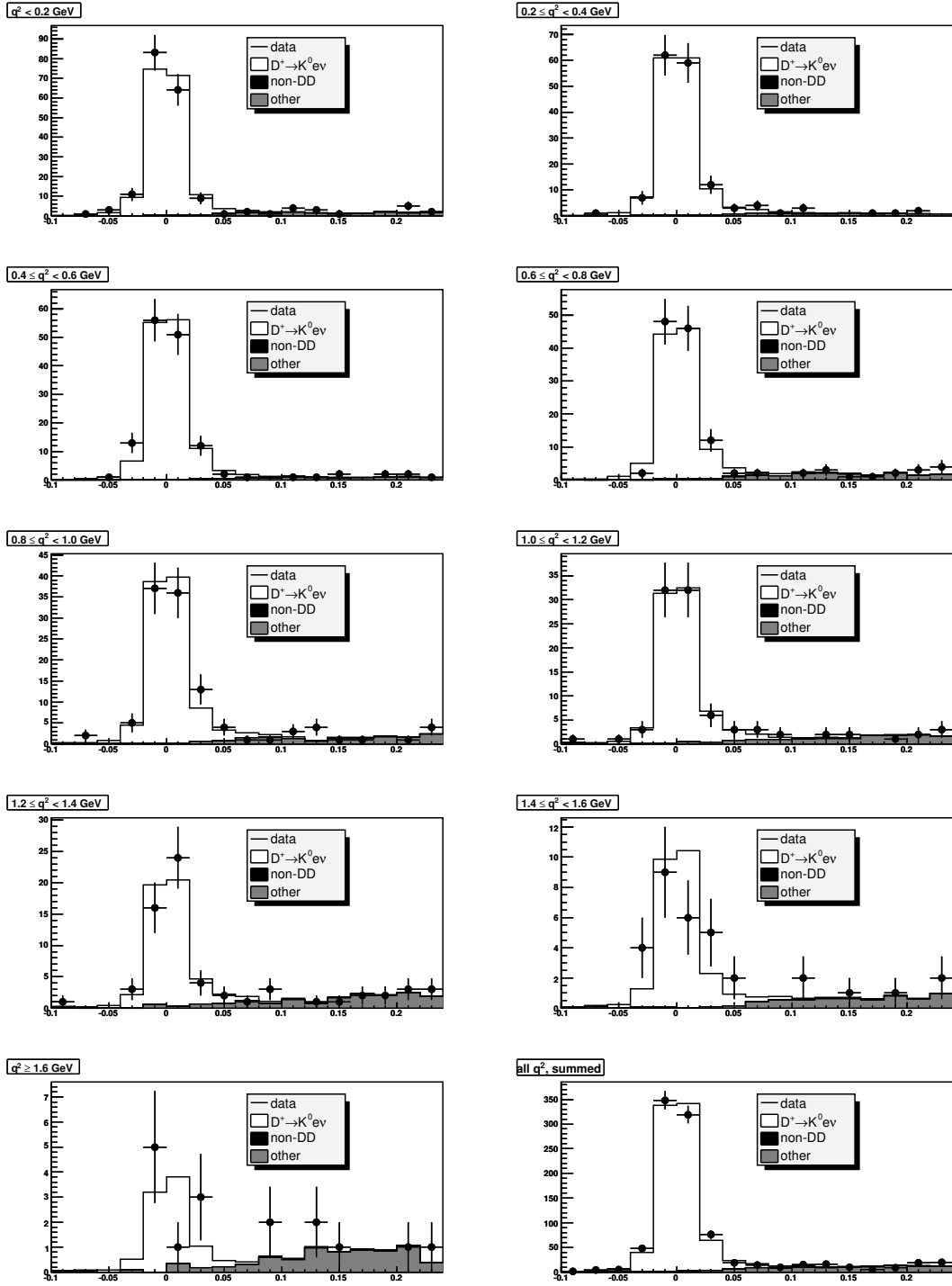
Figure 20: Signal yield fits to $D^+ \rightarrow \bar{K}^0 e^+ \nu_e$ candidates opposite $D^- \rightarrow K^0 \pi^- \pi^- \pi^+$ tags in data. The q^2 bin increases from left to right and down the page. The lower right-hand plot shows the sum of all q^2 bins.

131
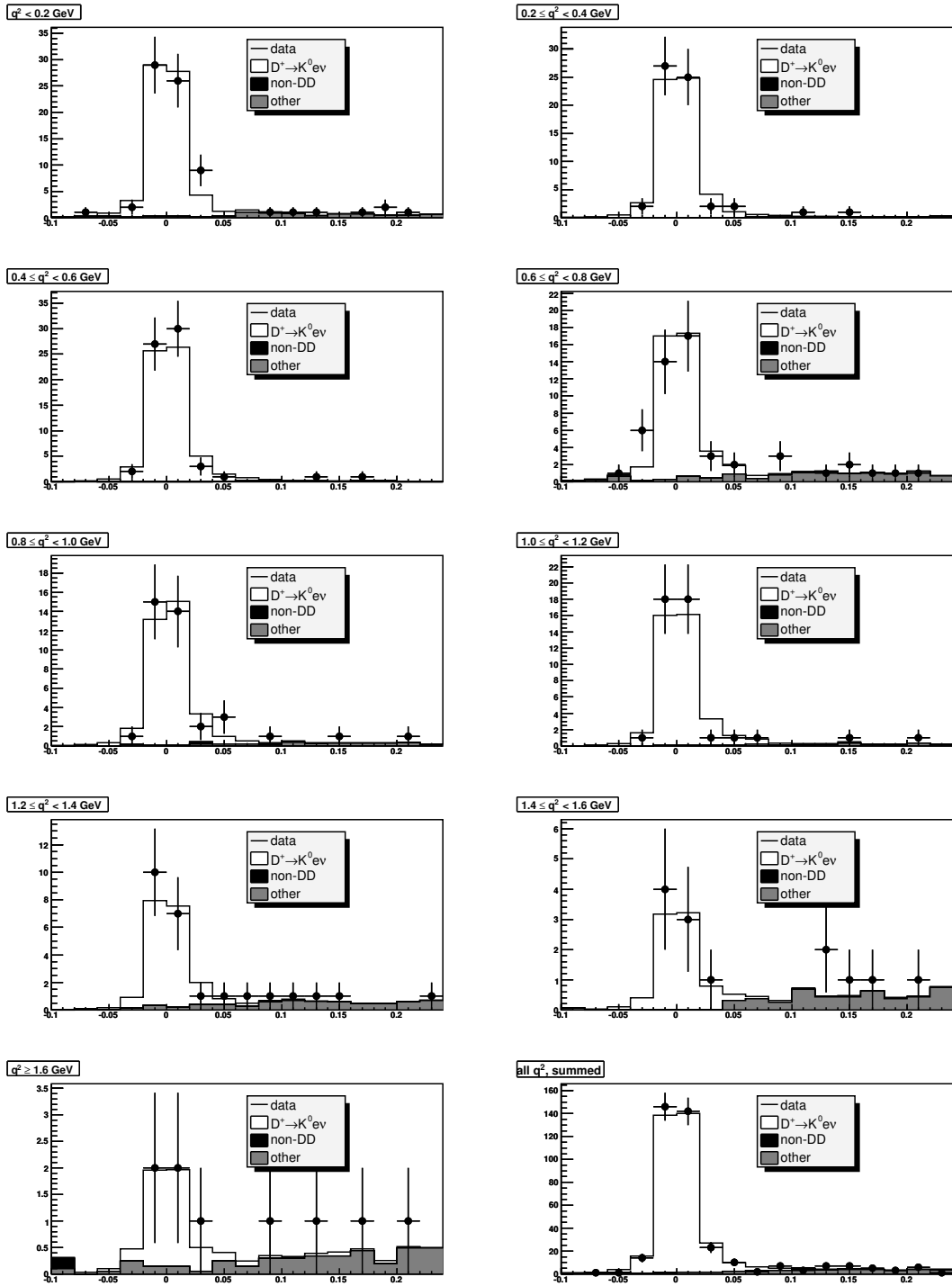
Figure 21: Signal yield fits to $D^+ \to \bar{K}^0 e^+ \nu_e$ candidates opposite $D^- \to K^+ K^- \pi^-$ tags in data. The q^2 bin increases from left to right and down the page. The lower right-hand plot shows the sum of all q^2 bins.
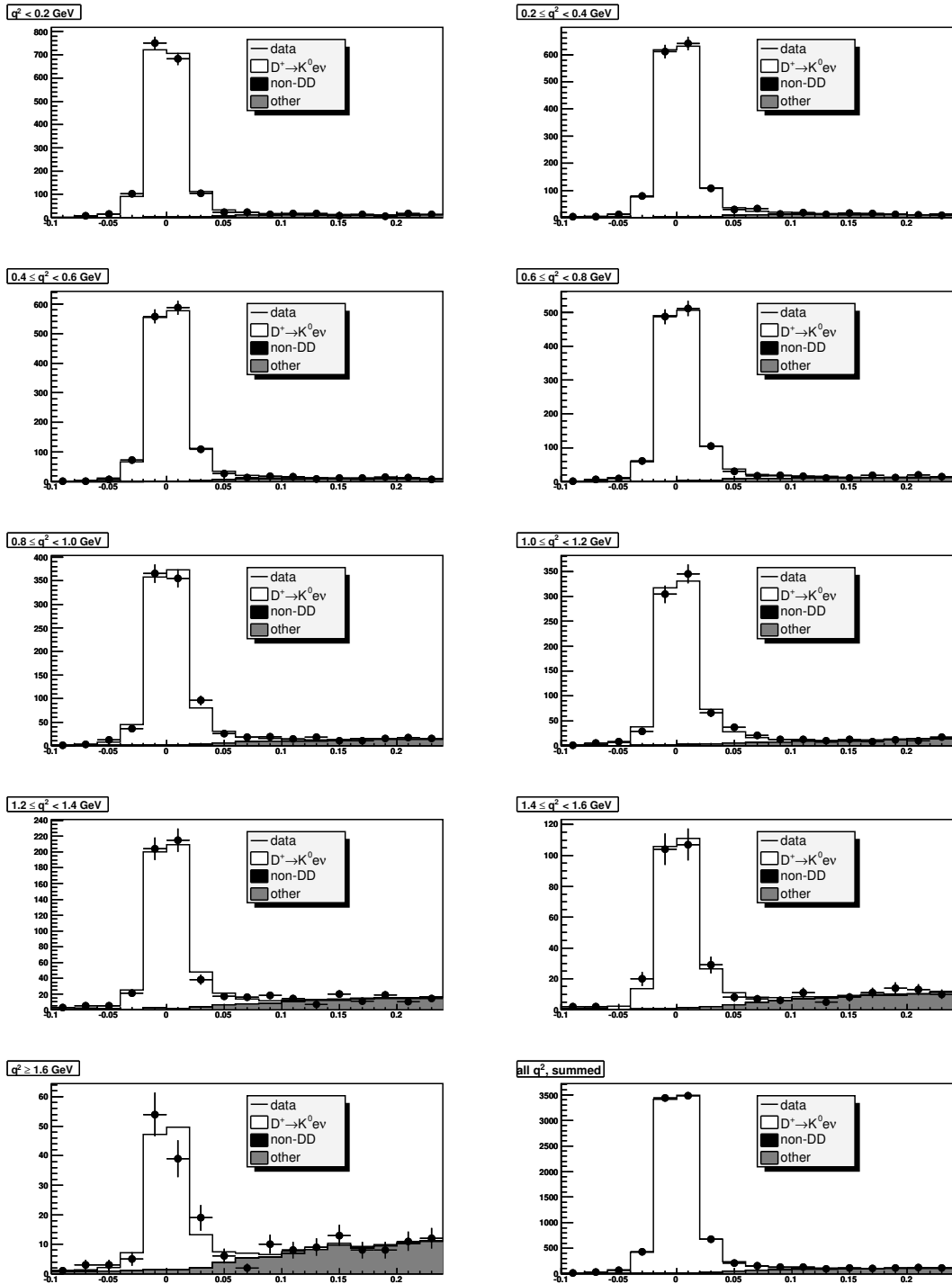
Figure 22: Signal yield fits to $D^+ \to \bar{K}^0 e^+ \nu_e$ candidate opposite all tag modes in data. The q^2 bin increases from left to right and down the page. The lower right-hand plot shows the sum of all q^2 bins.
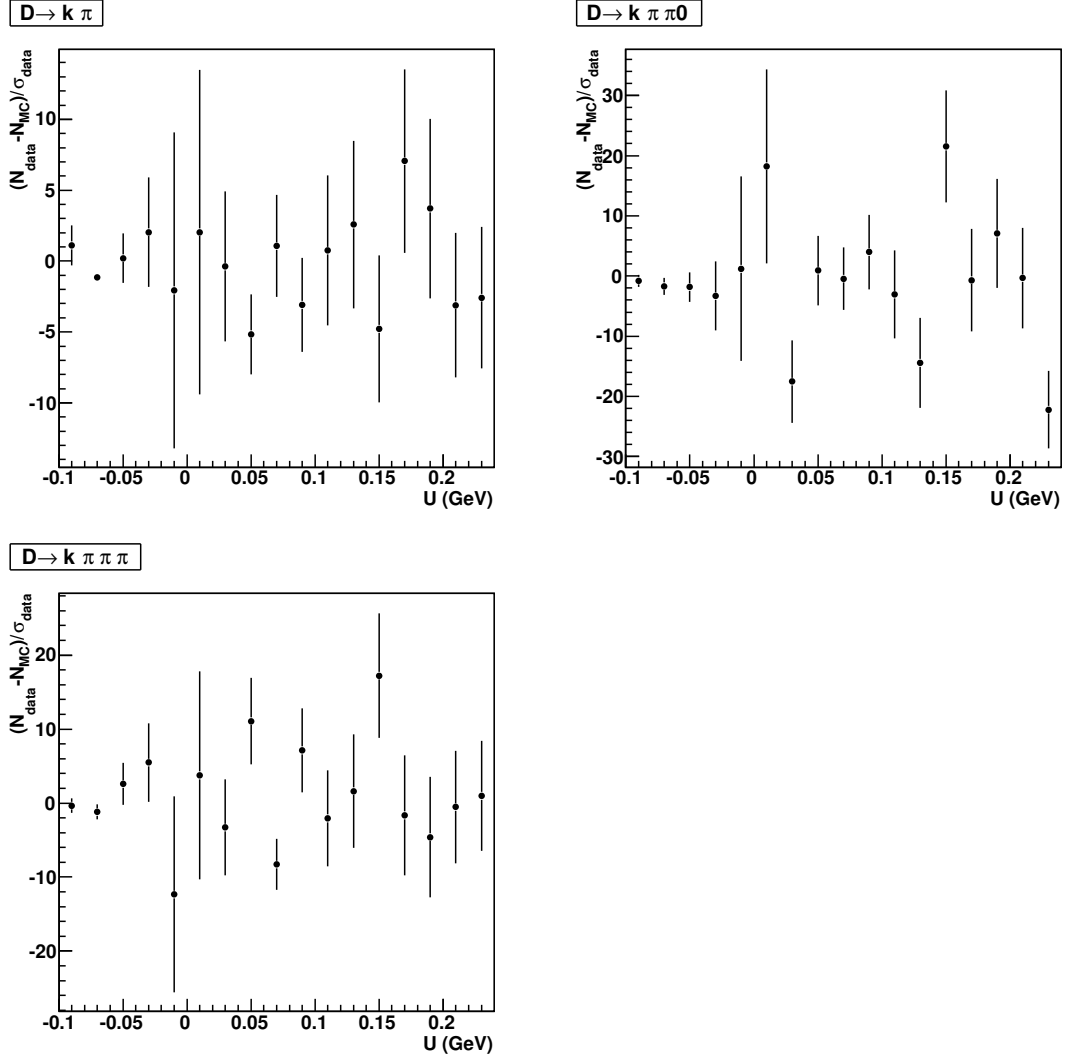
Figure 23: $D^0 \to \pi^- e^+ \nu_e$ Residuals: data - MC (from signal yield fits) in units of σ_{data}, summed over q^2 for each tag mode. Error bars show statistical uncertainties on data.
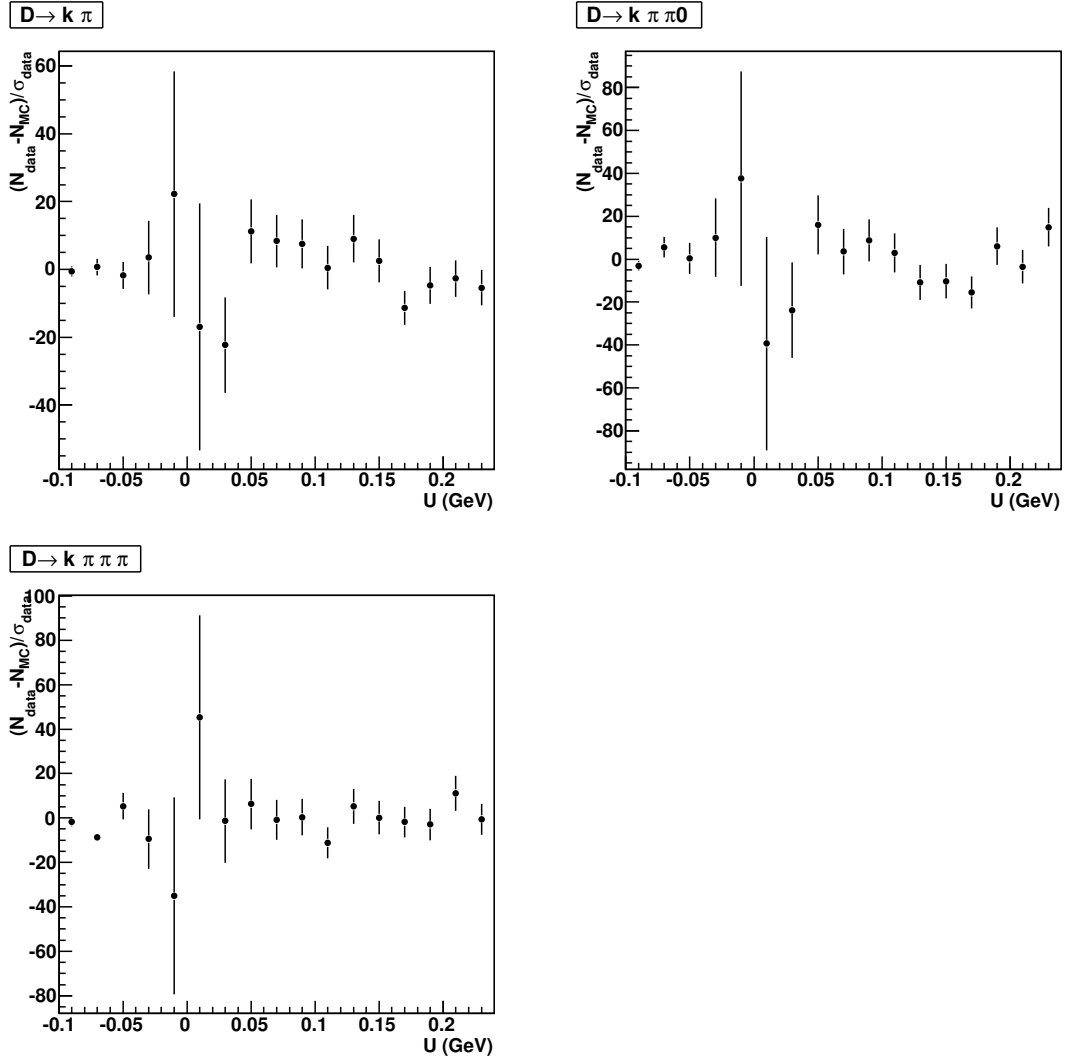
Figure 24: $D^0 \rightarrow K^- e^+ \nu_e$ Residuals: data - MC (from signal yield fits) in units of σ_{data}, summed over q^2 for each tag mode. Error bars show statistical uncertainties on data.
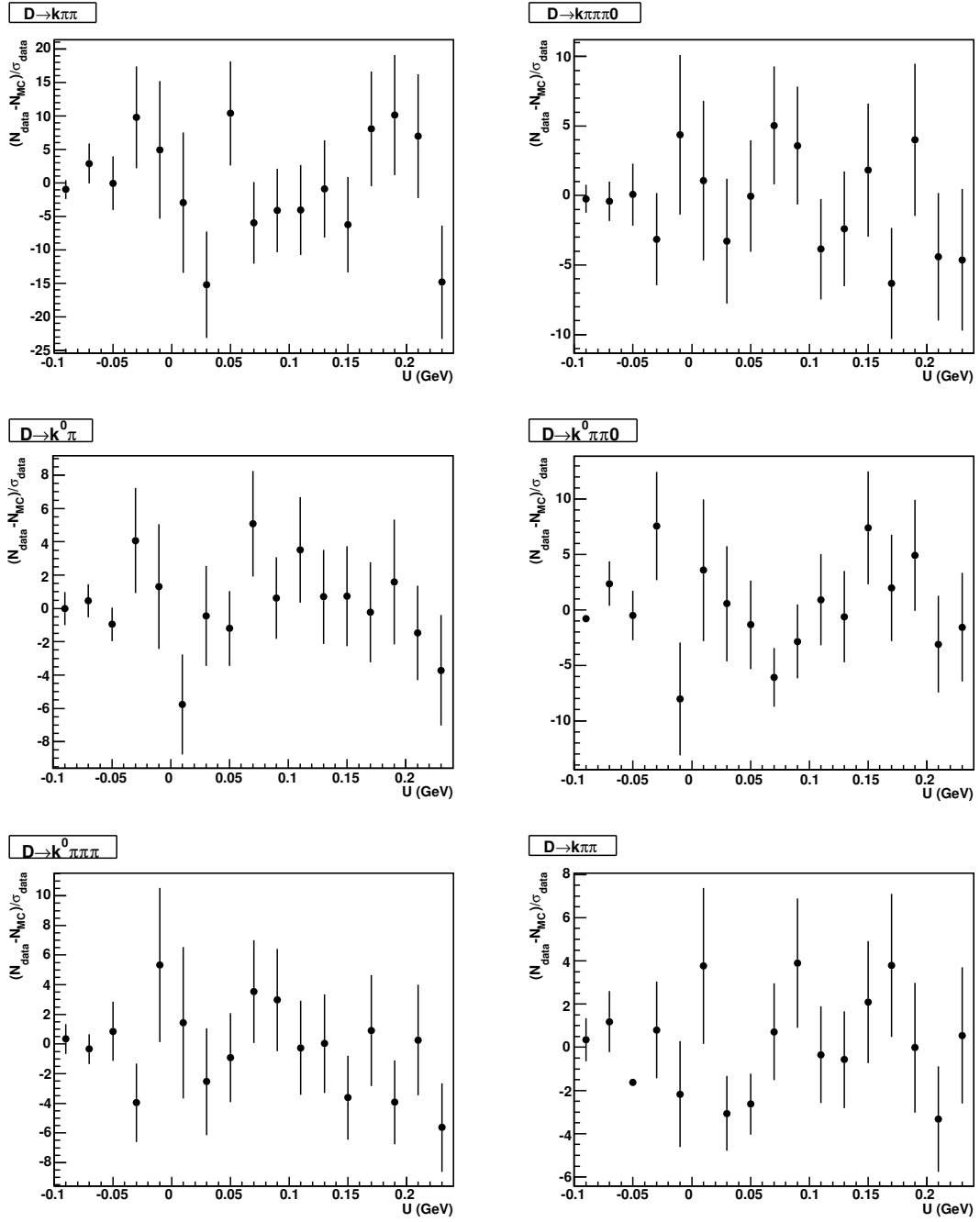
Figure 25: $D^+ \rightarrow \pi^0 e^+ \nu_e$ Residuals: data - MC (from signal yield fits) in units of σ_{data}, summed over q^2 for each tag mode. Error bars show statistical uncertainties on data.

136
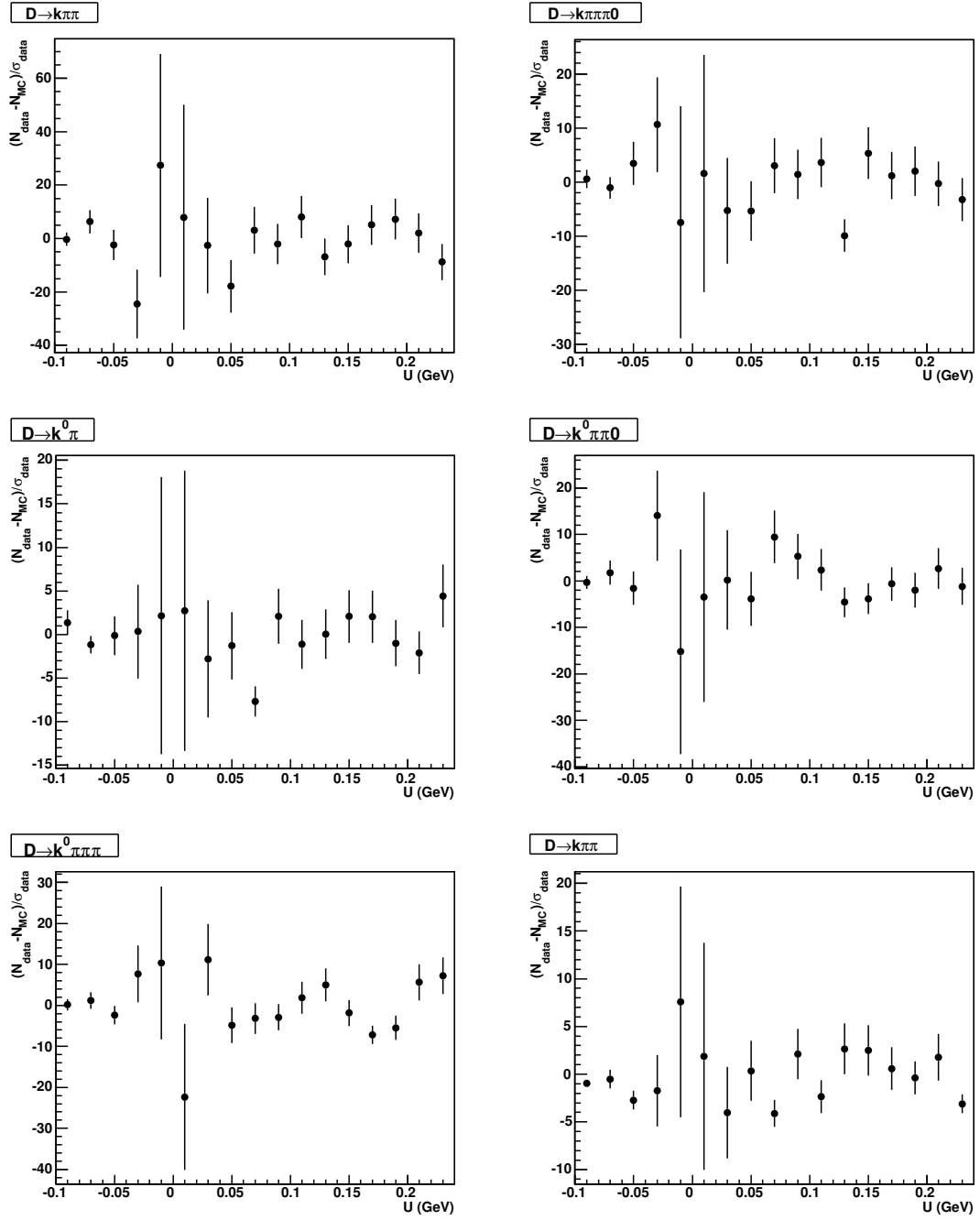
Figure 26: $D^+ \rightarrow \bar{K}^0 e^+ \nu_e$ Residuals: data - MC (from signal yield fits) in units of σ_{data}, summed over q^2 for each tag mode. Error bars show statistical uncertainties on data.

BIBLIOGRAPHY

[1] M. Kobayashi and T. Maskawa, Prog. Theor. Phys. **49**, 652 (1973).

[2] J. D. Richman and P. R. Burchat, Rev. Mod. Phys. **67**, 893 (1995), hep-ph/9508250.

[3] T. Becher and R. J. Hill, Phys. Lett. **B633**, 61 (2006), hep-ph/0509090.

[4] J. Y. Ge (CLEO) (2008), 0810.3878.

[5] D. Scora and N. Isgur, Phys. Rev. **D52**, 2783 (1995), hep-ph/9503486.

[6] G. P. Lepage (1998), hep-lat/0506036.

[7] A. Abada *et al.*, Nucl. Phys. **B619**, 565 (2001), hep-lat/0011065.

[8] C. Aubin *et al.* (Fermilab Lattice), Phys. Rev. Lett. **94**, 011601 (2005), hep-ph/0408306.

[9] P. Colangelo and A. Khodjamirian (2000), hep-ph/0010175.

[10] A. Khodjamirian, R. Ruckl, *et al.*, Phys. Rev. **D62**, 114002 (2000), hep-ph/0001297.

[11] V. M. Braun (1997), hep-ph/9801222.

[12] P. Ball, Phys. Lett. **B641**, 50 (2006), hep-ph/0608116.

[13] W. Y. Wang, Y. L. Wu, *et al.*, Phys. Rev. **D67**, 014024 (2003), hep-ph/0205157.

[14] D. Melikhov and B. Stech, Phys. Rev. **D62**, 014006 (2000), hep-ph/0001113.

[15] N. Isgur, D. Scora, *et al.*, Phys. Rev. **D39**, 799 (1989).

[16] J. Adler *et al.* (MARK-III), Phys. Rev. Lett. **62**, 1821 (1989).

[17] J. M. Link *et al.* (FOCUS), Phys. Lett. **B607**, 233 (2005), hep-ex/0410037.

[18] M. Ablikim *et al.* (BES), Phys. Lett. **B597**, 39 (2004), hep-ex/0406028.

[19] L. Widhalm *et al.*, Phys. Rev. Lett. **97**, 061804 (2006), hep-ex/0604049.

[20] B. Aubert *et al.* (BABAR), Phys. Rev. **D76**, 052005 (2007), hep-ex/0607077.

[21] S. Dobbs *et al.* (CLEO), Phys. Rev. **D77**, 112005 (2008), 0712.1020.

[22] C. Amsler *et al.* (Particle Data Group), Phys. Lett. **B667**, 1 (2008).

[23] CLEO-c/CESR-c Taskforces & CLEO-c Collaboration, Cornell LEPP preprint CLNS 01/1742 (2001) (unpublished).

[24] Y. Kubota *et al.* (CLEO), Nucl. Instrum. Meth. **A320**, 66 (1992).

[25] Gollin *et al.*, IEEE Trans. Nucl. Sci. **48**, 547 (2001); Hans *et al.*, *ibid.*, 552; Selen *et al.*, *ibid.*, 562.

[26] R. Brun et al., GEANT 3.21, CERN Program Library Long Writeup W5013 (1993) (unpublished).

[27] D. J. Lange, Nucl. Instrum. Meth. A **462**, 152 (2001).

[28] E. Barberio and Z. Was, Comput. Phys. Commun. **79**, 291 (1994).

[29] S. Dobbs *et al.* (CLEO), Phys. Rev. **D76**, 112001 (2007), 0709.3783.

[30] A. Ryd, *Fitting M_{BC} Distributions*, CLEO CBX 05-06 (2005).

[31] H. Albrecht *et al.* (ARGUS), Phys. Lett. **B241**, 278 (1990).

[32] D. Cassel *et al.*, *Determination of Tracking and Particle Identification Efficiencies*, CLEO CBX 04-39.

[33] L. Fields and R. Patterson, π^0 *Finding Efficiencies*, CLEO CBX 2008-29.

[34] M. Lefebvre, R. K. Keeler, *et al.*, Nucl. Instrum. Meth. **A451**, 520 (2000), hep-ex/9909031.

[35] S. Stroiney *et al.*, *Determination of Tracking Efficiencies*, CLEO CBX 08-040.

[36] I. Brock and R. Briere, *Pion and Kaon Identification Efficiencies for Cleo-c*, CLEO CBX 05-43 (2004).

[37] S. Stroiney, *Determination of K_0^S Efficiencies*, CLEO CBX 08-040.

[38] C. Park and E. Thorndike, *EID Systematic Uncertainty for Full 3770 Data Set*, CLEO CBX 08-49 (2008).

[39] X. Shi *et al.*, *Absolute Determination of Branching Fractions for Hadronic D Decays and Measurements of the Cross Sections for $e^+e^- \rightarrow D^0\bar{D}^0$ and $e^+e^- \rightarrow D^+D^-$*, CLEO CBX 07-XX (unpublished) (2007).

[40] R. Gray, Ph.D. thesis, Cornell University (2008).